This electronic thesis or dissertation has been downloaded from the King's Research Portal at https://kclpure.kcl.ac.uk/portal/

Spontaneous emission inside hyperbolic metamaterials

Roth, Diane Joane

Awarding institution:
King's College London

The copyright of this thesis rests with the author and no quotation from it or information derived from it may be published without proper acknowledgement.

END USER LICENCE AGREEMENT

Unless another licence is stated on the immediately following page this work is licensed

under a Creative Commons Attribution-NonCommercial-NoDerivatives 4.0 International

licence. https://creativecommons.org/licenses/by-nc-nd/4.0/

You are free to copy, distribute and transmit the work

Under the following conditions:

- Attribution: You must attribute the work in the manner specified by the author (but not in any way that suggests that they endorse you or your use of the work).
- Non Commercial: You may not use this work for commercial purposes.
- No Derivative Works - You may not alter, transform, or build upon this work.

Any of these conditions can be waived if you receive permission from the author. Your fair dealings and other rights are in no way affected by the above.

Take down policy

If you believe that this document breaches copyright please contact librarypure@kcl.ac.uk providing details, and we will remove access to the work immediately and investigate your claim.

Download date: 05. May. 2023

King's College London

Doctoral thesis

Spontaneous emission inside hyperbolic metamaterials

Author:

Diane J. Roth

Supervisor:

Prof. Anatoly V. Zayats

A thesis submitted in fulfilment of the requirements

for the degree of Doctor of Philosophy

in the

Experimental Biophysics & Nanotechnology Group

Department of Physics

December 2017

Abstract

Spontaneous emission is a fundamental manifestation of quantum mechanics and is strongly modified by the material environment in which the emitters are placed. Achieving the control of radiative and non-radiative transitions is of great importance for applications ranging from biosensing and optical communications to quantum technologies. The design of nanostructured media with tailored electromagnetic properties opens up a route for controlling the emission rate and the non-radiative energy transfer via the engineering of the local density of optical states. In this thesis, the influence of a gold nanorod-based hyperbolic metamaterial on the spontaneous emission and energy transfer between emitters located within the metamaterial is investigated. Hyperbolic metamaterials have emerged as a flexible and powerful platform for these purposes providing a high local density of states due to their peculiar mode structure. In a theoretical and experimental analysis, it is shown that the emission process in a nanorod-based hyperbolic metamaterial is strongly affected by its nonlocal response, thus impacting the emission dynamics and leading to a broadband 30-fold reduction of the emitters lifetime spanning the whole visible spectral range. To further emphasize the importance of the mode structure of the metamaterial in the emission process, an almost 50-fold enhancement of the spontaneous emission coupled to a waveguided mode of the metamaterial is demonstrated. The emission of a long lifetime Ruthenium complex involving spin-forbidden dipolar transitions is also studied. Rate enhancements far beyond the predictions of the standard electromagnetic local density of states description are observed, reaching 1000-fold near a gold film and higher inside the metamaterial. The influence of the local density of states on non-radiative energy transfer is presented, leading to more than 10-fold increase of the FRET rate inside the metamaterial. These results demonstrate the potential of highly tuneable hyperbolic metamaterials for the control of spontaneous emission and energy transfer, highlighting the capability of such materials for the design of enhanced and fast light sources.

Acknowledgements

First of all I would like to thank my supervisor, Professor Anatoly Zayats, for giving me the opportunity to work under his guidance on this project but also for his continuous support and advice. A special thanks to Dr. Grégory Wurtz, for having given me the opportunity to join the group for an undergraduate research project and first introduced me to the field of plasmonics. I am also particularly grateful to Dr. Wayne Dickson for his constant encouragement and advice and to Dr. Nicolas Olivier for his help in the lab. I also would like to thank Dr. Alexey Krasavin, Dr. Jean-Sébastien Bouillard, Dr. Tomasz Stefaniuk and the other academic staff from the Plasmonics research group for their help and encouragement. A special thanks goes to the members of the Physics department administrative staff and in particular the unforgettable Julia Kilpatrick, who has always been so helpful and caring. Also, the lab wouldn't run so smoothly without the support of the technical staff members, especially William Luckhurst.

I would particularly like to thank my colleagues and friends: Giovanni Sartorello, Francesco Lotti, Dr. Francisco Rodriguez Fortuño and Michela Picardi. A massive thanks goes to Luke Nicholls and Dr. William Wardley, who, despite being sometimes annoying, supported me at all times.

Many thanks to Emile, who has always been present and made sure I wasn't going to lose my Frenchness. I don't forget my friends back in France: Camille, Caroline and Virginie, whom I can count on for a good laugh every time I go back to France. Lastly I would like to thank my family and also Dan for their support throughout.

Contents

List of Figures

Abbreviations

AAO	**A**nodised **A**luminium **O**xide
ADC	**A**nalog-to-**D**igital **C**onverter
APD	**A**valanche **P**hoto**D**iode
ATR	**A**ttenuated **T**otal **R**eflection
CCD	**C**harge-**C**oupled **D**evice
DNA	**D**eoxyribo**N**ucleic **A**cid
EDTA	**E**thylene**D**iamine**T**etra**A**cetic
ENZ	**E**psilon-**N**ear-**Z**ero
FLIM	**F**luorescence **L**ifetime **I**maging **M**icroscopy
FRET	**F**örster **R**esonance **E**nergy **T**ransfer
HMM	**H**yperbolic **M**eta**M**aterial
HWM	**H**yperbolic **W**aveguided **M**ode
LSP	**L**ocalised **S**urface **P**lasmon
MIM	**M**etal-**I**nsulator-**M**etal
MLCT	**M**etal-to-**L**igand **C**harge-**T**ransfer
PAGE	**P**oly**A**crylamide **G**el **E**lectrophoresis
PL	**P**hoto**L**uminescence
PMT	**P**hoto**M**ultiplier **T**ube
QDs	**Q**uantum **D**ots
SEM	**S**canning **E**lectron **M**icroscopy
SERS	**S**urface-**E**nhanced **R**aman **S**pectroscopy
SLR	**S**urface **L**attice **R**esonance
SPAD	**S**ingle **P**hoton **A**valanche **D**iode
SPCE	**S**urface **P**lasmon **C**oupled **E**mission
SPP	**S**urface **P**lasmon **P**olariton
TAC	**T**ime-to-**A**mplitude **C**onverter
TAE	**T**ris-**a**cetate-**E**DTA
TCSPC	**T**ime-**C**orrelated **S**ingle **P**hoton **C**ounting
TE	**T**ransverse **E**lectric
TM	**T**ransverse **M**agnetic
TMM	**T**ransverse **M**atrix **M**ethod
TTL	**T**ransistor-**T**ransistor **L**ogic
TTS	**T**ransit **T**ime **S**pread

Chapter 1

Introduction

Spontaneous emission of light, describing the phenomenon of de-excitation of atoms by emission of a photon, is responsible for most of the light generated around us. From light emission by living organisms such as fireflies, to cutting-edge technologies such as modern light sources and display screens, the process of spontaneous emission can be distinguished by the source of energy from which it originates. Light emission resulting from excitation sources other than heat is known as luminescence. This includes, among others, electroluminescence, where light is emitted due to the electron-hole recombination in the material upon application of an electric current; and photoluminescence, spontaneous emission generated upon absorption of photons. Both electro- and photoluminescence have major roles in day-to-day applications and are heavily investigated in several research domains, where the precise engineering of the spontaneous emission and non-radiative processes properties could lead to significant advances.

Photoluminescence, which can be differentiated between fluorescence and phosphorescence according to the electronic transitions involved in the emission process, has many applications ranging from the well-known fluorescent lamps to biotechnologies such as bioimaging or biosensing. Fluorescent labels such as organic dyes, which are commonly being used in bioapplications, often suffer from low brightness or low photostability, especially in the far-red / near-infrared spectral range. This spectral range, comprising wavelengths between 700 nm and 1700 nm, appears to be really attractive for bioapplications because of minimum photodamage to samples and deep tissue penetration (up to 4 cm [1]). Therefore,

there is a need to amplify the signal emitted by the emitters in order to improve detection sensitivity and reach detection-levels down to the single-molecule.

The possible control of spontaneous emission is also of particular interest for several other domains ranging from solid-state lighting to data communication and quantum computing areas. Solid-state lighting, which is typically based on the use of semiconductor Light-Emitting Diodes (LEDs), is currently replacing most of the light bulbs and compact fluorescent tubes in lighting elements and is present in most of the displays of electronic devices due to their low energy consumption and small sizes. With Haitz's law predicting an increase of the luminous flux per LED package by a factor 20 per decade [2], the aim is today to investigate the possibilities to increase the quantum efficiency of the emitters and achieve very bright LEDs and thus efficient light sources [3, 4]. The potential control of spontaneous emission has also gained interest in the field of data communications, where achieving very high modulation rates of emitters could lead to the substitution of power consuming lasers by LEDs for short-range microchip communications. These high-modulation rates could then also be beneficial for the development of Li-Fi and data transfer via common household LEDs. Lastly, research towards quantum information technologies has recently led to the need of single photon sources, requiring efficient single photon emitters. For these applications, the stability of the emitters along with high quantum yield and emission rate, high purity and indistinguishability [5] are required. While colour centres in crystals, such as nitrogen-vacancies in nanodiamonds, or semiconductor quantum dots (QDs) are the most promising types of emitters for such sources, these systems could all benefit from the engineering of the spontaneous emission process in order to enhance their capabilities.

In order to compensate for limitations and develop new technologies, one can take advantage of the non-inherent character of the spontaneous emission properties of emitters. Indeed, spontaneous emission based processes are strongly influenced by the local electromagnetic environment in which the emitters are located. Therefore, the careful engineering of the emitters' surroundings enables the control of the spectral properties, directionality and decay dynamics of the emitters. This can be achieved by placing the emitters in the vicinity of suitably designed photonic or plasmonic structures. Photonic structures, such as resonators, have shown their potential in the control of spontaneous emission thanks to high quality factors (up to 10^6) owing to their low losses. These structures have nevertheless

reached a frontier in their development due to diffraction, preventing the concentration of the light below the diffraction limit and hence restricting the down-scaling of the mode volumes (V). This ultimately limits the enhancement of the spontaneous emission rate of emitters (F_p) achievable with such structures since $F_p \propto 1/V$. This fundamental limit can however be compensated for by the use of plasmonic structures, with their peculiar mode structure and ability to confine light on subwavelength scales leading to high electromagnetic field enhancements. Despite the losses introduced by the presence of the metal, plasmonic nanostructures have been shown to be able to strongly influence the spontaneous emission properties of emitters placed in their vicinity by increasing the excitation rates at the positions of the emitters, shaping their emission profiles or modifying their radiative and non-radiative decay rates [6]. The modification of the decay rate of the emitters owes to the alteration of the local density of electromagnetic states (LDOS) of the system, corresponding to the number of electromagnetic states available to the emitters to decay into. The large LDOS present in plasmonic structures thus favours the relaxation of the emitters to the ground state, leading to high decay rates and emission enhancement.

The influence of the LDOS on the spontaneous emission of emitters has also led to the study of the influence of the electromagnetic environment on non-radiative processes, such as energy transfers between emitters. In particular, Förster resonance energy transfer (FRET), which is used to estimate distances between nearby emitters at the nanoscale, is limited to distances of the order of a few nanometers and could notably benefit from signal enhancement in order to extend its detection range. FRET is also of primary interest in various processes and applications such as biosensing [7], organic photovoltaics [8] or light sources [9], which could as well take advantage of engineered emission and decay rates.

In this context, constant advances in nanophotonics and plasmonics, joined with new fabrication and characterisation techniques, have led to the possibility of engineering materials and structures with tailored electromagnetic properties in order to suitably control their interaction with light. From metallic films, nanoparticles and nanoantennas to photonic/plasmonic crystals and cavities, the influence of the local environment on the spontaneous emission properties of emitters is an ongoing field of investigation. Recently, hyperbolic metamaterials, consisting of engineered composites constituted of metallo-dielectric subwavelength unit cells, have emerged as a very flexible and powerful platform

for spontaneous emission engineering as they provide a theoretically infinite LDOS $\rho(\omega)$ thanks to the unique high-wavevector modes characteristic of their topology, yielding $\rho(\omega) \propto k_{max}^3$. In practice, the upper boundary for high-wavevector modes supported by hyperbolic metamaterials k_{max}^3 is set by factors such as material losses and geometry, leading to a finite LDOS.

This thesis particularly investigates the influence of a hyperbolic metamaterial comprised of an array of gold nanorods on the spontaneous emission of emitters and energy transfer processes between them. The inexpensive and relatively easy fabrication process of nanorod-based hyperbolic metamaterials, using a self-assembled approach combined with the ability to tune their geometrical parameters, allow their electromagnetic properties to be tailored in a wide spectral range and over large areas. This geometry also provides significant advantages with regard to the placing of the emitters inside the metamaterial.

In Chapter 2, the concepts of spontaneous emission and energy transfer as well as the fundamentals of plasmonics, relevant to the work presented in this thesis, will be presented.

In Chapter 3, the main experimental and theoretical results, related to spontaneous emission and energy transfer engineering, will be reviewed from the literature, covering the various photonic and plasmonic electromagnetic environments used so far and their advantages.

In Chapter 4, the experimental techniques used for the fabrication of the samples and their optical characterisation will be discussed. In particular, the design of the TCSPC system built in the scope of this thesis and the data analysis methods common to several experimental studies developed in the following chapters will be described.

In Chapter 5, both an experimental and theoretical analysis of the process of spontaneous emission in a nanorod-based hyperbolic metamaterial exhibiting non-local electromagnetic behaviours will be presented. The decay dynamics of several emitters spanning the elliptic and hyperbolic dispersion regimes of a nanorod-based metamaterial are shown to be essentially dominated by the non-local response of the composite.

In Chapter 6, the spontaneous emission of various dyes inside a metamaterial-based planar waveguide will be discussed. The importance of the mode structure in the enhancement of

the spontaneous emission thanks to the coupling of the emitted light to the waveguided mode supported by the metamaterial slab will be demonstrated.

In Chapter 7, the study of the spontaneous emission of a Ruthenium complex in different electromagnetic environments including a nanorod-based metamaterial will be described. Experimental enhancement of the spontaneous emission rate far beyond the predictions of the standard electromagnetic local density of states description, typically employed for the spontaneous emission enhancement analysis of dipolar transitions, have been obtained.

In Chapter 8, the process of non-radiative energy transfer between donor and acceptor emitters in various plasmonic environments will be studied. By investigating the donor's emission dynamics and the free-space acceptor's emission intensity, the FRET rate and efficiency dependence on the modification of the local density of electromagnetic states available for the emitters to decay is investigated.

Finally, Chapter 9 will summarise the results obtained and discuss the open routes for further investigations.

Chapter 2

Fundamentals of spontaneous emission and plasmonics

This chapter presents an overview of the basic concepts of spontaneous emission and energy transfer processes, followed by fundamental theory of plasmonic excitations such as surface and localised modes. Finally, metamaterials and their optical properties will be discussed, introducing the concept of non-local optical response in plasmonic nanorod-based metamaterials.

2.1 Spontaneous emission

Spontaneous emission is defined as the process by which a quantum emitter transitions from an excited state to a lower energy state by releasing energy in the form of a photon. This process can be in the simplest case approximated to a two-level system; E_1 (ground state) and E_2 (excited state) as shown in Figure 2.1; where the emitter in its excited state E_2 may spontaneously decay to the lower energy state E_1 by emitting a photon of energy equal to the difference in energy between the two states, such as

$$E_2 - E_1 = \hbar\omega \tag{2.1}$$

where ω is the angular frequency of the photon and $\hbar$ is the reduced Planck constant. The resulting photon is emitted in a random direction and has a random phase.

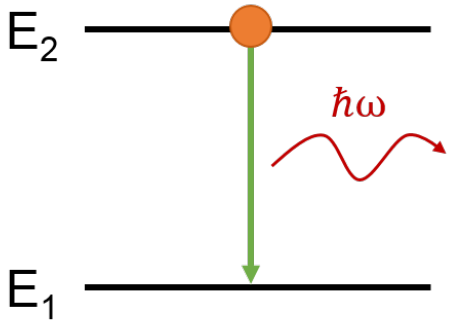

FIGURE 2.1: Diagram of a two-level system.

Before being able to relax to its ground state, the emitter undergoes a process of absorption of energy, which can be of different nature regarding the energy source considered. In the case of photoluminescence, the energy is provided by the absorption of photons by the material, promoting electrons to an excited state. Due to the instability of these excited states, the electrons then undergo a transition back to the ground state along with the emission of photons.

The energy levels and various transitions occurring in the absorption and emission processes of organic fluorophores are classically represented by a Jablonski diagram as shown in Figure 2.2. S_0, S_1 and S_2 respectively represent the singlet electronic ground state, first and second electronic excited state, while T_1 is the first electronic triplet excited state. Each of these electronic states are constituted by several vibrational energy levels, which the excited emitter can occupy (the rotational energy sublevels are not shown). The phenomenon of photoluminescence can be divided into two different processes: fluorescence and phosphorescence, respectively involving relaxation of an emitter from a singlet or triplet excited state. The various types of transitions are depicted by different styles of arrows and will be explained in more details in the following subsections.

2.1.1 Excitation

Photoluminescence occurs after absorption of electromagnetic radiation by an emitter [11]. During absorption of a photon, one of the electron of the emitter undergoes a transition from the ground state (S_0) to one of the vibrational energy levels of an excited singlet

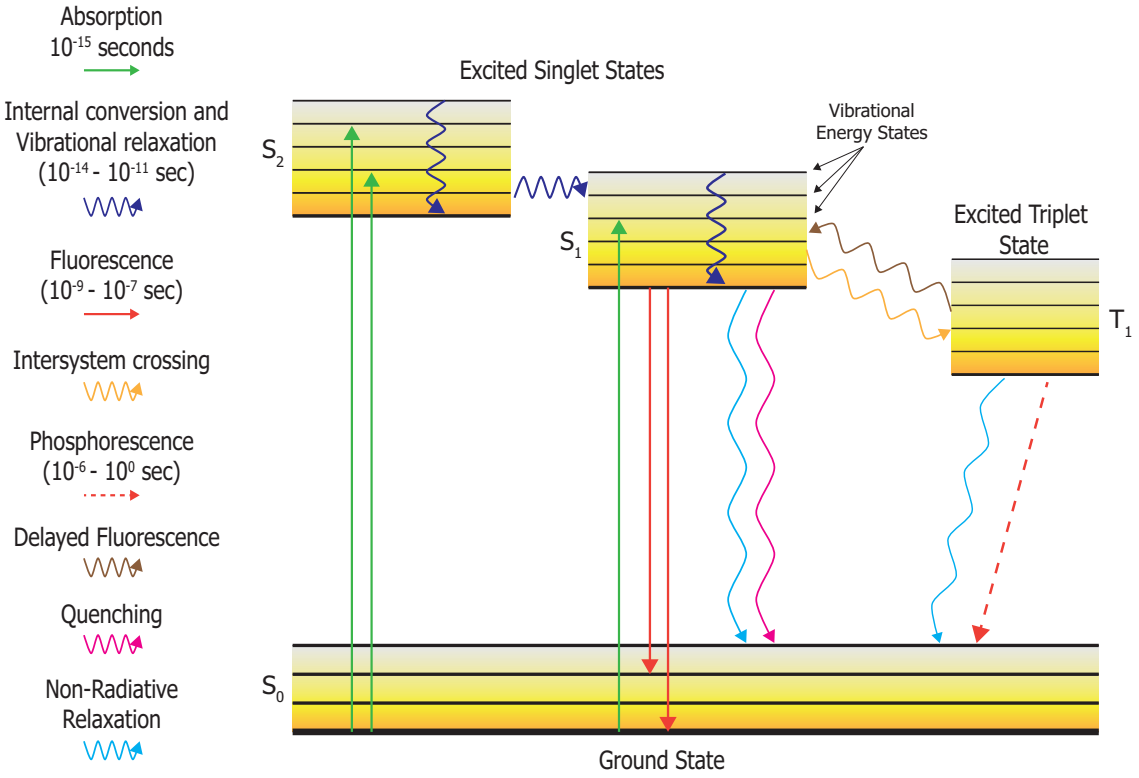

FIGURE 2.2: **Jablonski diagram.** (adapted from [10])

electronic state (S_1 or S_2). This transition occurs without spin flip of the promoted electron and the time required for this transition is typically of the order of 10^{-15} seconds. The absorption of a photon can promote the emitter to any of the vibrational or rotational levels of an excited state. Each of these different levels will be represented by a peak in the absorption spectrum of the emitter. However, as depicted in Figure 2.3 for Rhodamine 6G, the absorption spectrum of a fluorophore in solvent will most likely appear as a broad absorption peak with smeared out features, resulting from the broadening of the individual peaks due to the interaction between the solvent and the emitters.

2.1.2 Relaxation

Fluorescence. In the case of fluorescence, the emitter stays in the excited state for periods of the order of nanoseconds ($10^{-9} - 10^{-7}$ seconds) before relaxing to one of the vibrational energy levels of the ground state S_0 by emitting a photon. Prior to the emission of a photon, the emitters will most likely be subjected to a non-radiative relaxation to the lowest vibrational energy level of the first excited state. This non-radiative relaxation can

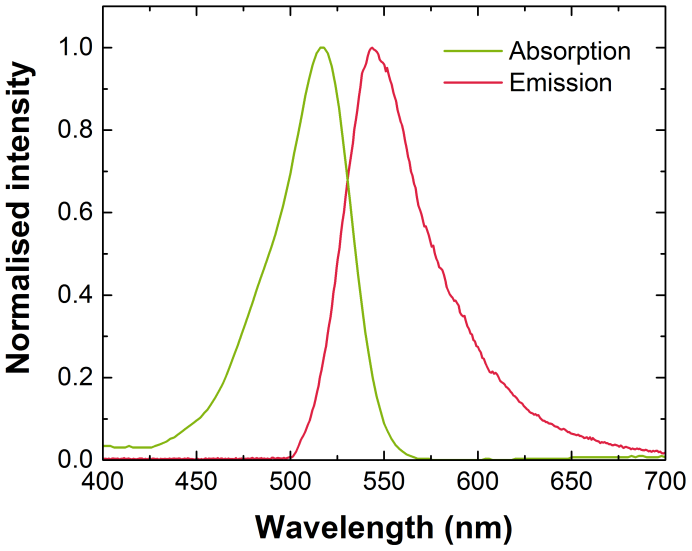

FIGURE 2.3: **Normalised absorption and emission of Rhodamine 6G.**

take place from vibrational levels of high energies to the lowest vibrational level of the same state and is called vibrational relaxation, while the process of de-excitation between excited states ($S_2 \rightarrow S_1$) is called internal conversion. This process is possible thanks to a high coupling between the vibrational levels of these two singlet energy states due to the overlap of some of their vibrational energy levels and generally occur within 10^{-13} to 10^{-11} seconds [12].

Exactly as the absorption process, the relaxation process can occur from the lowest vibrational energy level of the first excited state to any of the vibrational or rotational levels of the singlet ground state. Hence, the emission spectrum of a given emitter also exhibits broad features. Due to the rapid vibrational relaxation of the emitter to the lowest vibrational level of the first singlet excited state after excitation and the relaxation to one of the higher vibrational level of the singlet ground state, the emitted photon typically has lower energy than the corresponding absorbed photon. This typical red-shift of the emission was first observed by Sir G. G. Stokes, and named after him as the Stokes shift. The very similar organisation of the vibrational levels of the singlet ground and excited state leads to an emission spectrum which is the mirror-image of the absorption spectrum.

Intersystem crossing, phosphorescence and delayed fluorescence. The fluorescence emission process also competes with various other de-excitation pathways, involving

triplet excited states. For instance, emitters in the first singlet excited state can undergo transitions to a vibrational level of the triplet excited state of equivalent energy, via a process called intersystem crossing. This transition involves spin inversion, as singlet and triplet states have different multiplicities. It is important to note that these transitions between energy levels of different multiplicities are theoretically forbidden due to the existence of selection rules and in particular, the spin selection rule [13]. However, this rule, derived from quantum mechanical calculations, does not take into account the interactions between electrons and nuclei in a molecule. These interactions, known as spin-orbit coupling, induce a mixing of the singlet and triplet states, leading to partially allowed transitions between states of different multiplicities. Intersystem crossing is particularly favoured in the presence of atoms having high atomic masses, leading to increased spin-orbit coupling (heavy atom effect). Following intersystem crossing, emitters in high vibrational energy levels will undergo vibrational relaxation and relax back to the lowest vibrational energy level of the excited triplet state. Due to the fact that the lowest vibrational level of the triplet state is lower than that of the singlet state, emitters are theoretically trapped in this state before relaxation. Relaxation from the excited triplet state to the ground singlet state can then take place either non-radiatively or with emission of a photon via phosphorescence. In the case of radiative emission via phosphorescence, this partially allowed transition, due to spin-orbit coupling, results in excited lifetimes orders of magnitude longer than fluorescence lifetimes ($10^{-6} - 10^{0}$ seconds). This emission typically occurs at longer wavelengths than fluorescence. Alternatively, emitters can relax to the ground state via a process called delayed fluorescence, where the electron in the triplet excited state transitions back to the singlet excited state. This transition can occur as thermally activated delayed fluorescence, if the energy difference between the excited singlet state (S_1) and the excited triplet state (T_1) is small and the lifetime of the triplet excited state is long; or as triplet-triplet annihilation, where the collision between emitters can provide enough energy for one of them to transition back to the excited singlet state. The emitter in the excited singlet state will then relax to the ground state by emission of a photon having the same spectral characteristics as the photon emitted during the conventional fluorescence process, but a longer lifetime.

Non-radiative relaxation processes. Several non-radiative relaxation processes can also take place, leading to a decrease in the fluorescence intensity. Different types of

molecular interactions, such as complex formations, energy transfer mechanisms or collisional quenching, can lead to static or dynamic quenching. Static quenching occurs due to the formation of a non-fluorescent complex between the emitter and the quencher in the ground-state. When the complex absorbs light, it immediately relaxes back to the ground state without emitting a photon. Unlike static quenching happening in the ground-state, dynamic quenching is an excited-state process. Dynamic quenching mechanisms can occur upon contact between the emitter and the quencher, known as collisional quenching. Typical collisional quenchers of fluorescence are for instance molecular oxygen [14, 15] and heavy ions such as iodide [16]. Another type of dynamic quenching occurs via non-radiative energy transfer and is known as Dexter energy transfer [17, 18]. Dexter energy transfer consists in a transfer of an excited-state electron from the donor to the excited-state of the acceptor. The acceptor then transfers a ground-state electron back to the donor. This interaction, resulting from intermolecular orbital overlap, is only possible at very short distances (typically $10\mathring{A}$). Another type of non-radiative energy transfer, Förster resonance energy transfer (FRET), will be discussed in more details in section 2.2.

2.1.3 Quantum yield and fluorescence lifetime

As mentioned in the previous section, the average time a fluorophore spends in the electronically excited state after absorption of a photon is a characteristic property of an emitter and is known as the fluorescence lifetime τ. τ is defined as the inverse of the sum of the rate constants for all the de-excitation pathways:

$$\tau = \frac{1}{\Gamma_r + \Gamma_{nr}} \tag{2.2}$$

where Γ_r and Γ_{nr} are respectively the radiative rate constant and the non-radiative rate constant.

In the absence of non-radiative processes, a natural (or radiative) lifetime $\tau_0 = \Gamma_r^{-1}$ can be defined and related to the fluorescence lifetime via another characteristic property of a fluorophore which is the fluorescence quantum yield ϕ

$$\phi = \frac{\tau}{\tau_0} = \frac{\Gamma_r}{\Gamma_r + \Gamma_{nr}} \tag{2.3}$$

The quantum yield represents the ratio of the number of photons emitted to the number of photons absorbed.

2.2 Energy transfer

The second important process to be described in this chapter is Förster Resonance Energy Transfer (FRET). FRET has been mostly used in fluorescence applications in the field of biotechnologies, where the aim is to study biological structures. FRET, often characterised as the "*spectroscopic ruler*" [19], allows the estimation of distances between two sites in a macromolecule at the nanometer scale, where the resolution in conventional fluorescence microscopy is limited by the spatial resolution (approximately 200 nm), which is defined by the Rayleigh criterion [20] $r = (0.61\,\lambda)/(n\,sin\theta) = (0.61\,\lambda)/NA$ with λ the wavelength and $n\,sin\theta$ the numerical aperture (NA) of the microscope objective used. FRET also constitutes an interesting technology for other domains of research, such as organic lighting sources [9], photovoltaics [8, 21] or sensing [7, 22].

FRET is a non-radiative process between two fluorophores, a donor (D) and an acceptor (A), where the donor in its excited state may transfer its excitation energy to the nearby acceptor in the ground state. This transfer is ensured by long-range intermolecular dipole-dipole coupling [23], that is to say that an emitter is considered as an oscillating dipole able to exchange energy with another dipole of similar frequency. Figure 2.4 represents a simplified Jablonski diagram showing the transitions involved in the energy transfer process. Absorption and emission transitions are represented by solid blue, green and red arrows, while vibrational relaxations between electronic states are shown with wavy purple arrows. The transitions actually affected by the presence of an energy transfer are represented by dashed lines. In the presence of a neighbouring acceptor, the donor is able to transfer its excited state energy to the acceptor at a rate of energy transfer k_T, which will be described later. It is important to emphasize that the transfer is non-radiative as the donor does not emit any photon while returning to the ground state and the acceptor does not absorb one.

The first experimental observations of energy transfer over larger distances than collision radii were made in 1922 by Cario and Franck [24], where they observed emission from thallium in a mixture of mercury vapor and thallium vapor upon excitation of the mercury

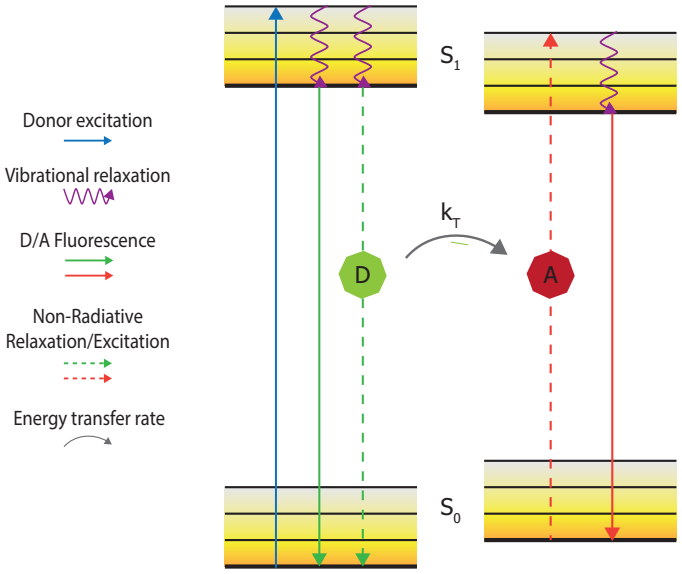

FIGURE 2.4: **Simplified Jablonski diagram for FRET.** (Adapted from [10])

atoms. This phenomenon, known as "sensitized fluorescence", was then observed for molecules in solution by J. Perrin and Choucroun [25]. Several important theoretical developments by Kallmann, London, J. Perrin, and F. Perrin paved the way for Theodor Förster's contributions on energy transfer theory [26]. In 1925, J. Perrin was the first to formulate a theory on energy transfer between molecules in condensed solvents based on the principles of classical physics. His model of two dipoles oscillating at the same frequency, in which it was assumed that molecules separated by a small enough distance could non-radiatively transfer energy to each other, resulted in a rate of energy transfer $k_T(r)$ dependent on the cube of the distance r between the molecules, leading to an overestimation of the range of possible energy transfer. A few years later, in 1928, Kallmann and London first proposed a quantum mechanical theory to explain the energy transfer between atoms in the vapour phase at longer distances than their collisional radii. This study led to the correct dependence of the energy transfer rate $k_T(r)$ on the distance r between atoms, $k_T(r) \propto r^{-6}$. With the help of Kallmann and London work, in 1932, F. Perrin then developed a quantum mechanical model for transfer energy between molecules in solution. The results in terms of distance dependence of the energy transfer were however the same as those from J. Perrin. Whereas the dependence of the energy transfer on the separation between donor and acceptor was not unanimously defined as the time, all

theories predicted the existence of a distance between donor and acceptor at which the probability of relaxation via energy transfer was equal to the probability of relaxation by all other decay pathways, later defined as Förster radius [27].

The main contribution of Förster in the development of the energy transfer theory arises from the connection of the energy transfer rate with data that can be obtained experimentally [27]. As will be developed below, Förster's theory of energy transfer includes several experimental datasets such as absorption and emission spectra, quantum yields and emission lifetimes. The next section will describe the final results of Förster's theory for energy transfer.

2.2.1 Theory of FRET

As mentioned above, the theory of FRET is based on the concept of an emitter as an oscillating dipole, which can exchange energy with another dipole with a similar resonance frequency [28]. Considering a single donor and acceptor separated by a distance r, the rate of energy transfer k_T is given by

$$k_T(r) = \frac{Q_D \kappa^2}{\tau_D r^6} \left(\frac{9000(ln(10))}{128\pi^5 N_A n^4} \right) \int_0^\infty F_D(\lambda)\epsilon_A(\lambda)\lambda^4 d\lambda \tag{2.4}$$

where Q_D is the quantum yield of the donor in the absence of the acceptor, n is the refractive index of the medium in which the molecules are, N_A is the Avogadro's number, r is the distance between the donor and the acceptor, τ_D the lifetime of the donor in the absence of acceptor and ϵ_A is the extinction coefficient of the acceptor at λ (in $mol^{-1}cm^{-1}$). λ represents wavelengths expressed in nm.

Two parameters in equation 2.4 remain to be explained. The first one, F_D, is the fluorescence spectrum of the donor normalised on the wavelength scale such as

$$F_D(\lambda) = \frac{f_{D_\lambda}(\lambda)}{\int f_{D_\lambda}(\lambda) d\lambda} \tag{2.5}$$

where $f_{D_\lambda}(\lambda)$ is the donor fluorescence per unit of wavelength interval and the integral extends over the relevant donor emission range.

Lastly, κ^2 represents an orientation factor with

$$\kappa = \vec{d}.\vec{a} - 3(\vec{d}.\vec{r})(\vec{r}.\vec{a}) = cos\theta_T - 3cos\theta_D cos\theta_A \tag{2.6}$$

where θ_D is the angle between the donor emission transition moment and the line connecting the donor and acceptor, θ_A is the angle between the acceptor absorption transition moment and the line connecting the donor and acceptor and θ_T is the angle between the donor emission transition moment and the acceptor absorption transition moment. The angles are illustrated in Figure 2.5. κ^2 can vary between 0 and 4. Three characteristic orientations of the dipoles are shown in Figure 2.5. In the case of random distribution of orientations, known as dynamic random averaging, κ^2 is equal to 2/3.

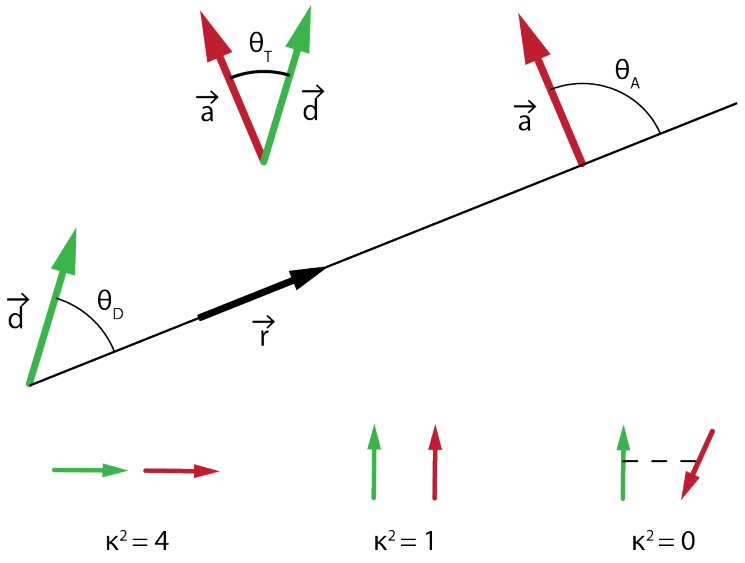

FIGURE 2.5: **Dependence of κ^2 factor on orientation of the transition dipoles of the donor and the acceptor.** $\vec{d}, \vec{a}$ and $\vec{r}$ are unit vectors (adapted from [11]).

The integral $\int_0^\infty F_D(\lambda)\epsilon_A(\lambda)\lambda^4 d\lambda$ in equation 2.4 represents the overlap integral $J(\lambda)$ between the emission spectrum of the donor and the absorption spectrum of the acceptor as shown in Figure 2.6. Considering the units chosen above, $J(\lambda)$ is expressed in $mol^{-1}cm^{-1}nm^4$.

Equation 2.4 can also be written in terms of distances between donor and acceptor by introducing the parameter R_0, the Förster radius, corresponding to the distance between the donor and acceptor at which the efficiency of energy transfer is equal to 50%. In other

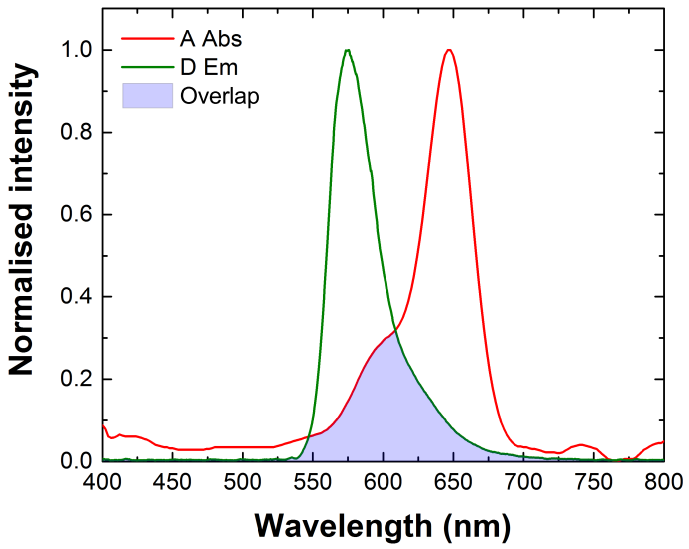

FIGURE 2.6: **Overlap between the emission spectrum of the donor and the absorption spectrum of the acceptor.**

words, R_0 corresponds to the distance at which the probabilities of spontaneous decay of the excited donor and energy transfer are equal [13]. This distance is typically of the order of 10 to 70 $\mathring{A}$ [13] and is specific to each pair of donor-acceptor molecules. Using this value R_0 and the fluorescence lifetime of the donor in absence of the acceptor τ_D, the rate of Förster dipole-dipole energy transfer is given by the following equation

$$k_T(r) = \frac{1}{\tau_D}\left(\frac{R_0}{r}\right)^6 \tag{2.7}$$

where r is the distance between the donor and acceptor.

Considering $r = R_0$, equation 2.7 becomes $k_T(r) = \frac{1}{\tau_D}$ and leads to the following expression for R_0

$$R_0^6 = \frac{9000(ln(10))Q_D\kappa^2}{128\pi^5 N_A n^4} J(\lambda) \tag{2.8}$$

which can be simplified as (in $\mathring{A}$)

$$R_0^6 = 8.79 \times 10^{-5}(Q_D\kappa^2 n^{-4} J(\lambda)) \tag{2.9}$$

The efficiency of energy transfer, which represents the fraction of the photons absorbed by the donor which are transferred to the acceptor is given by

$$E = \frac{k_T(r)}{k_T(r) + k_r^D + k_{nr}^D} = \frac{k_T(r)}{k_T(r) + \tau_D^{-1}} = \frac{R_0^6}{R_0^6 + r^6} \tag{2.10}$$

As depicted in Figure 2.7, the efficiency of energy transfer highly depends on the distance between donor and acceptor. The energy transfer efficiency rapidly increases for separation distances below the Förster radius R_0, to almost reach 100% when $r = R_0/2$. Hence, shorter distances than $r = R_0/2$ cannot be reliably determined. Contrarily, the efficiency drops for distances greater than R_0 to reach only 1.5% at $r = 2R_0$ making it impossible to determine longer distances accurately. These two boundaries typically set the range of operation of FRET.

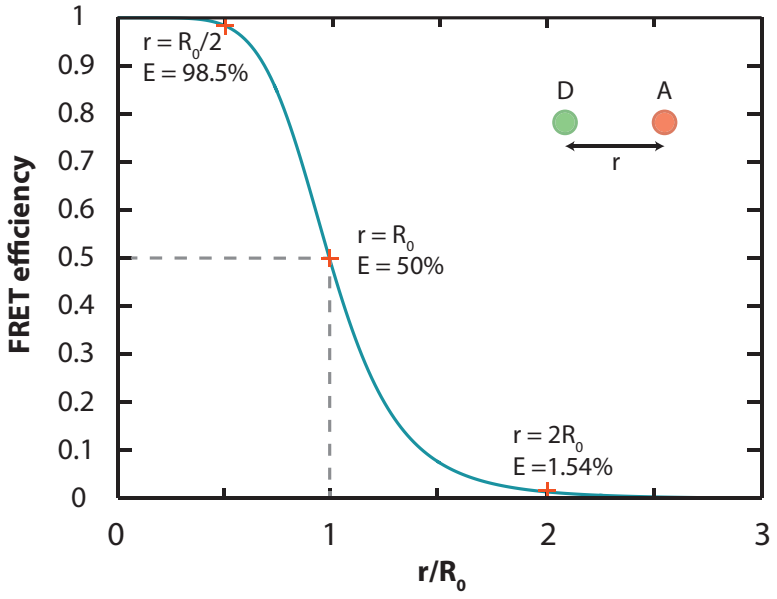

FIGURE 2.7: **FRET efficiency in function of distance r between the donor and acceptor.** R_0 is the Förster radius.

It is possible to determine the efficiency of energy transfer using fluorescence spectroscopy or time-resolved fluorescence measurements. To do so, either the relative fluorescence intensities (F_D and F_{DA}) or the lifetimes (τ_D and τ_{DA}) of the donor in respectively absence

and presence of the acceptor are needed as shown in Equation 2.11.

$$E = 1 - \frac{F_{DA}}{F_D} \tag{2.11a}$$

$$E = 1 - \frac{\tau_{DA}}{\tau_D} \tag{2.11b}$$

Equations 2.11a and 2.11b are valid only for a fixed distance between donor and acceptor pairs and not random dispersion of molecules in solution. Fixed distances between donor and acceptor pairs can for instance be achieved by using double-stranded DNA linkers. This method will be discussed in chapter 8. Also, in the case of multi-exponential decays of the donor, the use of an average lifetime taking into account the amplitudes of the components is needed. This average lifetime is defined as $\langle\tau\rangle = \sum \alpha_j \tau_j / \sum \alpha_j$ with α_j and τ_j the amplitude and the lifetime of the j^{th} component. These multi-exponential decays can arise from the presence of more than one distance between the donor and acceptor pairs or from a complex electromagnetic environment surrounding the molecules.

To summarise this section with a practical point of view, FRET allows the study of molecular processes with subnanometer resolution [29] but it is essential to remember the four major criteria that need to be satisfied in order for FRET to occur and on which the energy transfer rate depends:

- a reasonably high quantum yield (Q_D) of the donor and the absorption coefficient (ϵ_A) of the acceptor;
- a spectral overlap between the donor emission spectrum and the acceptor absorption spectrum;
- a relative orientation of the transition dipole moments of the donor and acceptor leading to $\kappa^2 \neq 0$;
- a distance between the donor and acceptor between $0.5R_0$ and $2R_0$, with R_0 typically in the range of 10 to 70 $\mathring{A}$.

2.3 Plasmonics

All the processes described in the previous sections are highly dependent on the electromagnetic environment in which the emitters are located and the control of both spontaneous emission or energy transfers has been shown to be extremely useful for many types of applications. In particular, plasmonic structures offer interesting electromagnetic properties allowing the modification of emission intensities or decay rates of emitters. This section describes the fundamental concepts of plasmonics and introduces the properties of hyperbolic metamaterials.

2.3.1 Optical properties of metals and Drude-Lorentz model

Metals are described as good conductors of heat and electricity and are characterised by the high density of free electrons they contain, typically of the order of $10^{28}-10^{29}$ $electrons/m^3$ [30], originating from the valence electrons of the metal atoms [31]. In order to characterise their optical properties, metals can be considered as a plasma, constituted of a neutral gas of free electrons moving around immobile positively charged ion cores. This approach is valid over a wide range of frequencies, particularly for alkali metals, but will be limited for other metals, due to several factors such as interband transitions, damping and losses [31, 32]. When subjected to an electromagnetic field $\mathbf{E}$, the free electrons oscillate in response to the applied field and their motion can be described as damped oscillators due to collisions occurring at a frequency $\gamma = 1/\tau$ (damping rate), where τ is the relaxation time of the free electron gas. This model is known as the Drude-Lorentz model and the equation of motion associated with an electron of the plasma upon excitation by an external electromagnetic field is given by

$$m_e \frac{\partial^2 \mathbf{r}}{\partial t^2} + \gamma m_e \frac{\partial \mathbf{r}}{\partial t} = -e\mathbf{E} \tag{2.12}$$

where e and m_e are the charge and the effective mass of the electron and $\mathbf{r}$ is the electron displacement. This equation does not include any restoring force as the electron is considered as a free electron. If we assume a harmonic time dependence of the external field such as $\mathbf{E(t)} = \mathbf{E_0} e^{i\omega t}$, with E_0 and ω are the amplitude and the angular frequency

of the applied field, a solution of equation 2.12 describing the oscillation of the electron is $\mathbf{r}(t) = \mathbf{r_0}e^{i\omega t}$, leading to

$$\mathbf{r(t)} = \frac{e}{m_e(\omega^2 + i\gamma\omega)}\mathbf{E(t)} \tag{2.13}$$

In the case of the charges motion, the polarisation of the medium induced by the electric field, which describes the density of electric dipole moment per unit volume inside the material $\mathbf{P} = -N_0 e\mathbf{r}(t)$, with N_0 the number of electrons per unit volume, yields:

$$\mathbf{P} = -N_0 e\frac{e}{m_e(\omega^2 + i\gamma\omega)}\mathbf{E(t)} \tag{2.14}$$

The application of an electric field $\mathbf{E(t)}$ to a medium leads to the motion of the free charges, which can be characterised by the dielectric permittivity ϵ and the electric displacement field, expressed as

$$\mathbf{D} = \epsilon\mathbf{E(t)} = \epsilon_0\epsilon_r\mathbf{E(t)} = \epsilon_0\mathbf{E(t)} + \mathbf{P} = \epsilon_0\mathbf{E(t)} - \frac{N_0e^2}{m_e(\omega^2 + i\gamma\omega)}\mathbf{E(t)} \tag{2.15}$$

where ϵ_0 is the permittivity of free space and ϵ_r is the relative permittivity of the material.

Rearranging equation 2.15 gives

$$\epsilon_r = 1 - \frac{N_0e^2}{\epsilon_0 m_e(\omega^2 + i\gamma\omega)} = 1 - \frac{\omega_p^2}{(\omega^2 + i\gamma\omega)} \tag{2.16}$$

with

$$\omega_p^2 = \frac{N_0e^2}{\epsilon_0 m_e} \tag{2.17}$$

ω_p is known as the bulk plasma frequency of the free electron gas, which depends on the density of free electrons and the effective mass of an electron. Therefore, ω_p is different for each metal.

In the case of negligible damping ($\gamma \simeq 0$), equation 2.16 can be simplified as

$$\epsilon_r = 1 - \frac{\omega_p^2}{\omega^2} \tag{2.18}$$

It can be shown that ω_p represents a cut-off angular frequency between the high reflectivity of the metal for $\omega < \omega_p$ (ϵ_r is negative) and a region where the metal is transparent for $\omega > \omega_p$ (ϵ_r is positive) [31], where the electron gas is not able to respond collectively to the applied field.

The Drude-Lorentz model correctly represents the properties of metals at low frequencies but fails at higher frequencies due to interband effects, where electrons from bands below the Fermi level, corresponding to the energy level with 50 % probability of being occupied by electrons at a finite temperature, can be promoted to the conduction band. These effects are related to the excitation of bound electrons of the filled bands, which translate into increased damping and therefore an increase of the imaginary part of the dielectric permittivity of the metal [31–33].

The next sections will be dedicated to surface modes such as surface plasmon polaritons and localised surface plasmons present in specific multilayer systems.

2.3.2 Surface modes

As discussed in section 2.1, an emitter in a homogeneous environment decays to the ground state radiatively and emit a photon, or non-radiatively due to various processes such as quenching or energy transfer. However, in the case where the emitter is placed close to an interface between two media of different refractive indices or in a stratified medium, the relaxation process is modified and new decay channels are introduced. The emitter may then not only relax to the ground state by the emission of a photon but also by coupling to electromagnetic surface modes introduced by the presence of the modified electromagnetic environment. This coupling to surface modes strongly depends on the geometrical parameters of the system but also on the electromagnetic properties of the materials constituting it. In optimised conditions, this coupling could represent the principal relaxation mechanism of the emitters.

2.3.2.1 Brief history of surface modes and the beginnings of plasmonics

The study of surface waves began at the start of the 20^{th} century with the separate mathematical studies of Zenneck, in 1907 [34], about the propagation of radio waves along the surface between two homogeneous media of different conductivities and dielectric constants; and Sommerfeld, in 1909 [35], with the study of the radiation of a vertical dipole at the surface of a finite conductivity ground. It is also at the start of the 20^{th} century that the first experimental demonstration of surface waves in the visible range of the electromagnetic spectrum took place. In 1902, Wood, unaware of the phenomenon he was observing at the time, noticed a drop in the reflected intensity from a metallic diffraction grating at specific wavelengths and this only for TM-polarised light [36]. These observations were only later explained by Rayleigh [37] and related to Sommerfeld's work by Fano in 1941 [38]. In 1957, Ritchie theoretically studied electron energy losses in thin metallic foils and showed some of the losses were due to excitation of plasma oscillations at the surface of the metals [39]. This is thought to be the first theoretical description of so-called surface plasmons. It is only in 1968 that he then related surface plasmon resonances to Wood's work on the metallic gratings [40]. It is also in 1968 that the two main first experiments of the field of plasmonics were performed by Otto [41] and the pair Kretschmann and Raether [42], who demonstrated two methods to observe the excitation of surface plasmons at the interface between a metal and a dielectric using total internal reflection, methods which are still currently being used for various sensing applications.

2.3.2.2 Surface Plasmon Polaritons

A surface plasmon polariton (SPP) is an evanescent electromagnetic surface wave propagating at the interface between a metal and a dielectric medium, resulting from the coupling of the electromagnetic field of the incoming light to the collective oscillations of electrons at the metal interface. These surface charge-density oscillations lead to strongly enhanced near-fields, which are confined to the metallo-dielectric interface and whose amplitudes decay exponentially with increasing distance from the interface. This makes SPPs very sensitive to surface conditions and largely used for sensing applications [33, 43].

The theoretical model for SPPs can be derived from the Maxwell's equations. SPPs can be described by finding the propagating waves' solutions satisfying the wave equation at

the smooth interface between two semi-infinite half-spaces of different dielectric constants, using the boundary conditions of continuity of the tangential components of **E** and **H** as well as the normal component of the electric displacement field **D** across the interface. Figure 2.8 shows the system considered consisting of a planar interface ($z = 0$) between a dielectric (region 1, for $z > 0$) of dielectric constant ε_1 and a metal (region 2, for $z < 0$) of dielectric constant $\varepsilon_2(\omega)$. Using the Maxwell-Faraday's and the Maxwell-Ampère's laws in the absence of external charge and current densities, a system of six equations can be derived in order to deduce explicit expressions of the electric field **E** and magnetic field **H**. If a harmonic time dependence of the electric field **E** is assumed and considering waves propagating in the positive x-direction and homogeneity in the y-direction, this system of equations can be separated into two sets of solutions with different polarisations of the propagating waves: transverse magnetic (TM) modes having only H_y, E_x and E_z non-zero components and transverse electric (TE) modes having only E_y, H_x and H_z non-zero components. This leads to two expressions of the wave equation for TE and TM modes respectively. Only TM-polarised modes will be considered in the following derivations as it can be shown that surface-plasmons do not exist for TE-polarised modes [32].

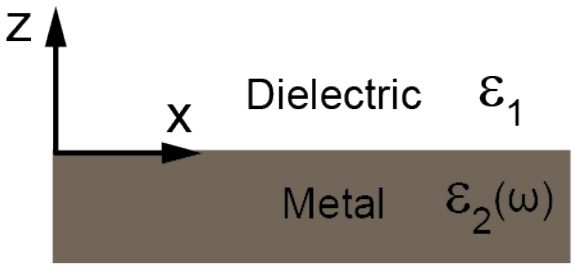

FIGURE 2.8: **Schematic of a metal-dielectric interface.**

Solving the wave equation for TM-polarised waves lead to the dispersion relation for SPPs at a single, flat interface between a dielectric and conductor:

$$k_x = k_{SPP} = \frac{\omega}{c}\sqrt{\frac{\varepsilon_1\varepsilon_2(\omega)}{\varepsilon_1 + \varepsilon_2(\omega)}} \tag{2.19}$$

The expressions for the normal component of the wavevector can also be obtained:

$$k_{z,1} = \frac{\omega}{c}\sqrt{\frac{\varepsilon_1^2}{\varepsilon_1 + \varepsilon_2(\omega)}} \tag{2.20a}$$

$$k_{z,2} = \frac{\omega}{c}\sqrt{\frac{\varepsilon_2(\omega)^2}{\varepsilon_1 + \varepsilon_2(\omega)}} \tag{2.20b}$$

Finding solutions that are propagating waves bound to the surface require having a real in-plane component of the wavevector k_x along x and the normal components of the wavevector purely imaginary in both media, leading to solutions decaying exponentially. From equations 2.19 and 2.20, this can be achieved only in the case where the real part of the dielectric constant of the metal ε_2' is negative and $|\varepsilon_2'| > \varepsilon_1$.

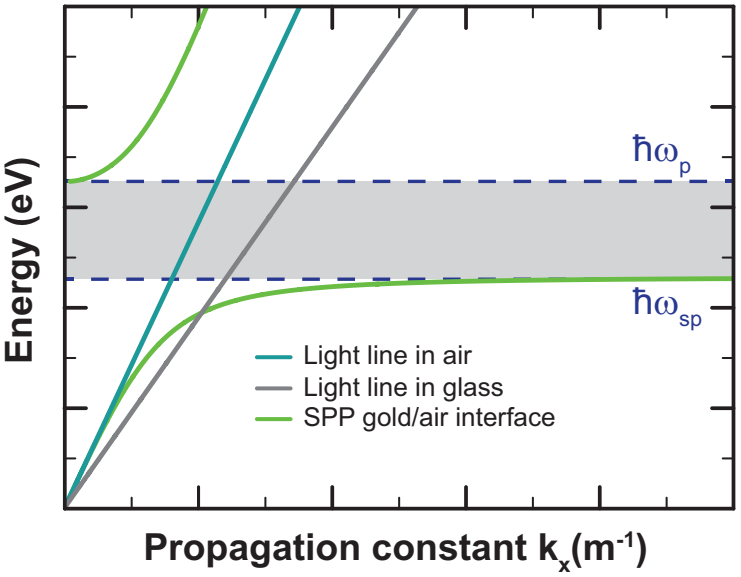

FIGURE 2.9: **SPP dispersion at a gold/air interface using the lossless Drude model.** The bulk plasma frequency for gold is $\omega_p = 1,37.10^{16}\ rad/s$.

Using the dielectric permittivity of gold given by the lossless Drude model (Equation 2.16), with a bulk plasma frequency of gold $\omega_p = 1,37.10^{16}\ rad/s$ and the dispersion relation given by Equation 2.19 for a gold/air interface, the SPP dispersion curve plotted in Figure 2.9 can be obtained. The blue and grey lines respectively represent the light-lines in air ($k_x = \omega/c$) and in glass ($k_x = \epsilon_{glass}\omega/c$ with $\epsilon_{glass} = 1.5^2$). The SPP dispersion shows two branches at low-energies and high-energies separated by a greyed area between the characteristic lines $\hbar\omega_{sp}$ and $\hbar\omega_p$ representing an energy range for which the values of k_x

are purely imaginary and hence the wave is not propagating. ω_{sp} is the asymptotic surface plasmon frequency expressed as

$$\omega_{sp} = \frac{\hbar\omega_p}{\sqrt{1+\epsilon_1}} \tag{2.21}$$

with in the case of air $\epsilon_1 = 1$.

The high-energy branch for $\omega > \omega_p$ corresponds to the so-called Brewster mode, where the z-component of the wavevector is not only imaginary but also has a real part. In this case, the considered wave is not bound to the surface and radiates into the metal. Finally, the low-energy branch, where k_x has a real part and k_z is purely imaginary, account for the propagation of surface plasmon polaritons. For low energies, the SPP dispersion curve follows the light-line in air, while at energies approaching $\hbar\omega_{sp}$, the difference in wavevectors increases, showing the coupling between electromagnetic wave and the surface charge oscillations. It is also worth noting that the wavevector of the SPP is always greater than the wavevector of a free space photon, meaning that SPPs can not be excited by incident light on the metal surface. Several techniques such as prism coupling or grating coupling are available to compensate for this momentum mismatch and increase the wavevector of the incident light in order to excite SPPs.

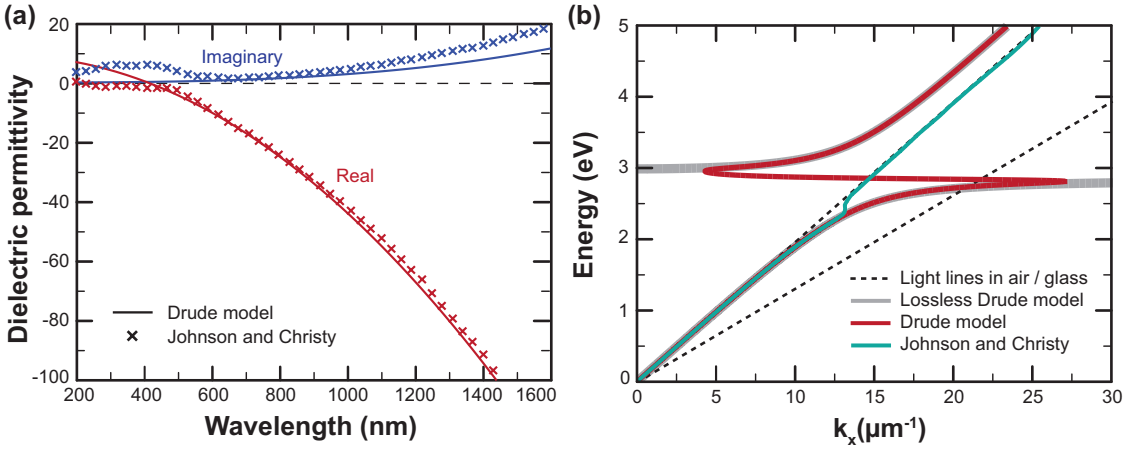

FIGURE 2.10: **Dielectric permittivity of gold and dispersion relations of surface plasmons at a gold/air interface. (a)** Dielectric constant of gold calculated from the Drude model with $\omega_p = 1,37 \times 10^{16}\ rad/s$ and $\gamma = 1,0027 \times 10^{14}\ s^{-1}$ and values from Johnson and Christy [44], **(b)** Dispersion relations of SPPs using the dielectric constants of gold represented in (a).

The dispersion curve shown in Figure 2.9 considered an ideal metal with $\epsilon_2''(\omega) = 0$. However, real metals suffer from losses and damping, leading to a complex value of the dielectric permittivity and hence, a complex value of the SPP dispersion relation. The SPP is then characterised by a propagation length $L = (2\,\mathrm{Im}[k_{SPP}])^{-1}$, where $\mathrm{Im}[k_{SPP}]$ is the imaginary part of k_{SPP} (equation 2.19). To highlight the effects of the losses and damping in the system, Figure 2.10b shows the calculated dispersion curve of a SPP propagating at a gold/air interface using both the full Drude model and values of the dielectric permittivity of gold from Johnson & Christy [44] represented in Figure 2.10a. Compared to the undamped case of Figure 2.9, there is now the existence of a finite value of k_x at the surface plasmon frequency and existence of propagating waves solutions between ω_{sp} and ω_p.

It is also important to note that in a more practical realisation, if a three-layer system consisting of a metallic film on a dielectric substrate and surrounded by air is considered, both the air/metal and the metal/substrate interfaces can support SPPs. Coupling between these two SPPs is then possible when the thickness of the metallic film becomes comparable to the electric-field decay lengths, leading to mode hybridisation [33].

2.3.2.3 Localised surface plasmons

Interactions between an electromagnetic field and free electrons in a metal can also occur in the case of small metallic nanoparticles, where their diameter d is small compared to the wavelength of the incident light λ. Under specific conditions, the electron cloud of the nanoparticle can be resonantly excited giving rise to so-called localised surface plasmons (LSPs), which, as opposed to SPPs, are non-propagating excitations of the conduction electrons of metallic subwavelength nanostructures coupled to an electromagnetic field [32].

In order to examine the properties of LSPs, the most straightforward nanostructure to consider is a subwavelength metallic sphere. In the presence of a time-harmonic electric field, the mobile cloud of conduction electrons undergo a displacement relative to the nuclei, creating a dipolar surface charge distribution within the particle as represented in Figure 2.11. This leads to a restoring force originating from Coulomb attraction between electrons and nuclei resulting in resonant oscillations of the electron cloud at a frequency

dependent on various factors such as the size and shape of the nanoparticle as well as its dielectric function and the surrounding environment [45–47].

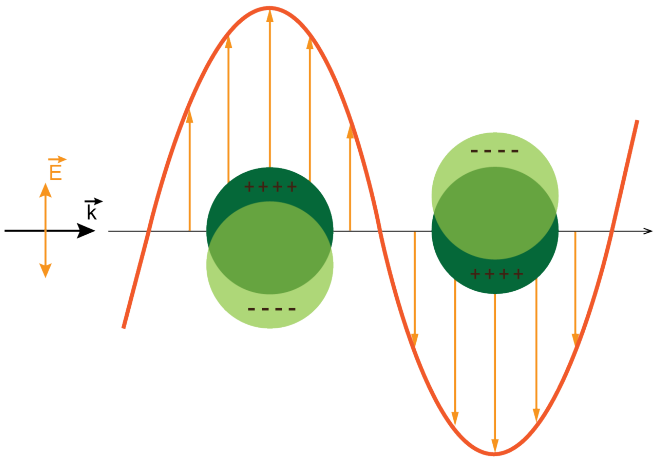

FIGURE 2.11: **Charge distribution for a metallic nanosphere under the presence of an external electric field.**

Considering a homogeneous metallic sphere of radius r and dielectric permittivity $\epsilon_2(\omega)$ placed in an isotropic dielectric medium of dielectric permittivity ϵ_1, the applied electric field $\mathbf{E}$ induces a dipole moment inside the sphere defined as

$$\mathbf{p} = \epsilon_1 \alpha \mathbf{E} \tag{2.22}$$

where α is the polarisability of the sphere

$$\alpha(\omega) = 4\pi\epsilon_0 r^3 \frac{\epsilon_2(\omega) - \epsilon_1}{\epsilon_2(\omega) + 2\epsilon_1} \tag{2.23}$$

The polarisability shows a resonance behaviour when $|\epsilon_2(\omega) + 2\epsilon_1|$ is a minimum, which in the case of a small imaginary part of ϵ_2 around the resonance ($\epsilon_2 = \epsilon_2'$) gives $\epsilon_2' = -2\epsilon_1$.

The theory existing for spherical particles can be extended to some other non-spherical shapes, such as ellipsoids with semiaxes $a,\ b$ and c [48, 49]. The polarisability of such particles along each axes ($m = a,\ b,\ c$) is given by

$$\alpha_m(\omega) = \epsilon_0 \frac{\epsilon_2(\omega) - \epsilon_1}{\epsilon_1 + L_m(\epsilon_2(\omega) - \epsilon_1)} V \tag{2.24}$$

where V is the volume of the ellipsoid such as $V = \frac{4\pi}{3}abc$, L_m is a geometrical factor given by $L_m = \frac{abc}{2}\int_0^\infty \frac{dq}{(m^2+q)f(q)}$ with $f(q) = \sqrt{(q+a^2)(q+b^2)(q+c^2)}$ and which satisfies $L_a + L_b + L_c = 1$.

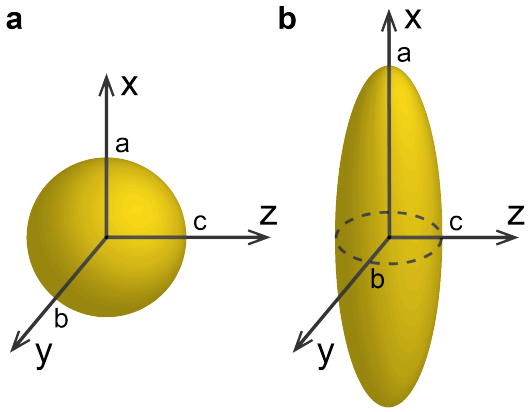

FIGURE 2.12: Schematic of **(a)** a spherical nanoparticle with $a = b = c$ and **(b)** a prolate spheroid of principal axis a and minor axes $b = c$.

A particular class of ellipsoids which is particularly interesting in this work is prolate spheroids, where the two minor axes are equal ($b = c$) and a is the principal axis as illustrated in Figure 2.12. The geometrical factors (respectively parallel and perpendicular to the principal axis), which can be expressed in function of the eccentricity of the spheroid $e = \sqrt{1 - \frac{b^2}{a^2}}$, are given by $L_\parallel = \frac{1-e^2}{e^2}\left[\frac{1}{2e}log\left(\frac{1-e}{1+e}\right) - 1\right]$ and $L_\perp = \frac{1-L_\parallel}{2}$. [50]

Spheroidal metal nanoparticles exhibit two distinct LSP resonances respectively corresponding to the oscillations of the free electrons along and perpendicular to the principal axis of the ellipse. This treatment is particularly useful to study highly anisotropic materials, such as plasmonic nanorod-based metamaterials, where the individual particles can be considered as prolate spheroids with high aspect ratios ($a >> b$) as will be seen in section 2.3.4.

2.3.3 Metamaterials

Due to the large number of applications of metamaterials which have been developed over the years, several definitions of what metamaterials are can be found in the literature. Taken from reference [51], *"a metamaterial is an artificially structured material which attains its properties from the unit structure rather than the constituent materials. A metamaterial has an inhomogeneity scale that is much smaller than the wavelength of*

interest, and its electromagnetic response is expressed in terms of homogenized material parameters.". This definition will be further explained in the next sections.

It is more than 30 years after Veselago's prediction [52] and shortly after Sir John Pendry's theoretical work on negative permittivity [53] and permeability [54] that the first experimental validation of an artificial left-handed material was performed by Smith *et al.* [55–58] in the microwave range of the electromagnetic spectrum. This material, constituted of split-ring resonators capable of producing negative magnetic permeability and wires to produce a negative dielectric permittivity over an overlapping frequency range, induces refraction in the opposite direction to normal refraction. This work, along with the theoretical work of Sir John Pendry on the so-called perfect lens made of a slab of negative-refractive index material [59], allowing resolution beyond the diffraction limit, marked the beginning of a rapidly developing field. Today's research in metamaterials has expanded to new applications in the microwave regime such as cloaking [60] or thermophotovoltaic applications [61], but also in new frequency ranges from the infrared [62–66] and near-infrared [67–69], to the visible [70–73] and the ultraviolet, taking advantage of new fabrication techniques in order to achieve smaller unit cell sizes.

Metamaterials are also commonly defined as engineered materials with electromagnetic properties which cannot be found in nature and are typically constituted of subwavelength building blocks, or meta-atoms. Analogous to how conventional materials and their properties at the macroscopic scale are defined by the assemblies of atoms they consist of, the electromagnetic properties of metamaterials arise from the composition of the meta-atoms, their spatial arrangement and the interaction between them. Hence, these materials can be described using an effective medium theory, which is detailed in section 2.3.4.3. In the visible and near-infrared spectral ranges, the combination of dielectric materials and metallic structures supporting surface plasmons excitations, as described in section 2.3.2.2, allow to precisely control the electromagnetic response of the metamaterial over a broad wavelength range and achieve desired properties. Many different geometries including split-rings resonators, fishnets, metallo-dielectric multilayers or nanorod assemblies have so far been designed and used for various applications such as sensing [74, 75] or subdiffraction imaging and nanolithography [76].

Among these materials, a sub-class of metamaterials, called hyperbolic metamaterials (HMMs), has emerged at the forefront of research in the field. These metamaterials are

uniaxial anisotropic metamaterials with electromagnetic properties that can be described with a diagonal tensor of effective dielectric permittivity as follows

$$\varepsilon_{\mathbf{eff}} = \begin{pmatrix} \varepsilon_{xx} & 0 & 0 \\ 0 & \varepsilon_{yy} & 0 \\ 0 & 0 & \varepsilon_{zz} \end{pmatrix} \tag{2.25}$$

where the in-plane components are equal $\varepsilon_{xx} = \varepsilon_{yy} = \varepsilon_{\perp}$ and of opposite sign from the out-of-plane component $\varepsilon_{zz} = \varepsilon_{\parallel}$. Note that HMMs can also have an anisotropic magnetic tensor μ_{eff} but in this case we will focus only on electric HMMs with $\mu_{\parallel} = \mu_{\perp} > 0$. The dispersion relation for such materials 2.26b in the case of transverse magnetic (TM) waves can then be compared with the dispersion relation for isotropic materials 2.26a.

$$\frac{(k_x^2 + k_y^2 + k_z^2)}{\varepsilon} = \left(\frac{\omega}{c}\right)^2 \tag{2.26a}$$

$$\frac{(k_x^2 + k_y^2)}{\varepsilon_{zz}} + \frac{k_z^2}{\varepsilon_{xx}} = \left(\frac{\omega}{c}\right)^2 \tag{2.26b}$$

where $k_x,\ k_y\ and\ k_z$ are respectively the $x,\ y$ and z components of the wavevector, ω is the angular frequency and c the speed of light in vacuum.

From equations 2.26 it can be seen that as opposed to isotropic media or anisotropic media with positive components of the effective dielectric permittivity, respectively exhibiting closed spherical (Figure 2.13a) or elliptical (Figure 2.13b) isofrequency surfaces, HMMs exhibit opened hyperboloid-shaped isofrequency surfaces. This leads to the presence of high-wavevector states, evanescent in conventional media, and a theoretically infinite local density of electromagnetic states. With regard to the number of negative components in the effective dielectric permittivity tensor, two different cases depicted in Figure 2.13c and 2.13d can then be distinguished where the hyperboloid is a double sheet, in the case of a type I HMM with $\epsilon_{xx} = \epsilon_{yy} > 0\ and\ \epsilon_{zz} < 0$, and a single sheet for a type II HMMs with $\epsilon_{xx} = \epsilon_{yy} < 0\ and\ \epsilon_{zz} > 0$.

Practical realisations of HMMs require the use of metallo-dielectric building blocks, as opposite signs of the components of the effective dielectric permittivity imply the material

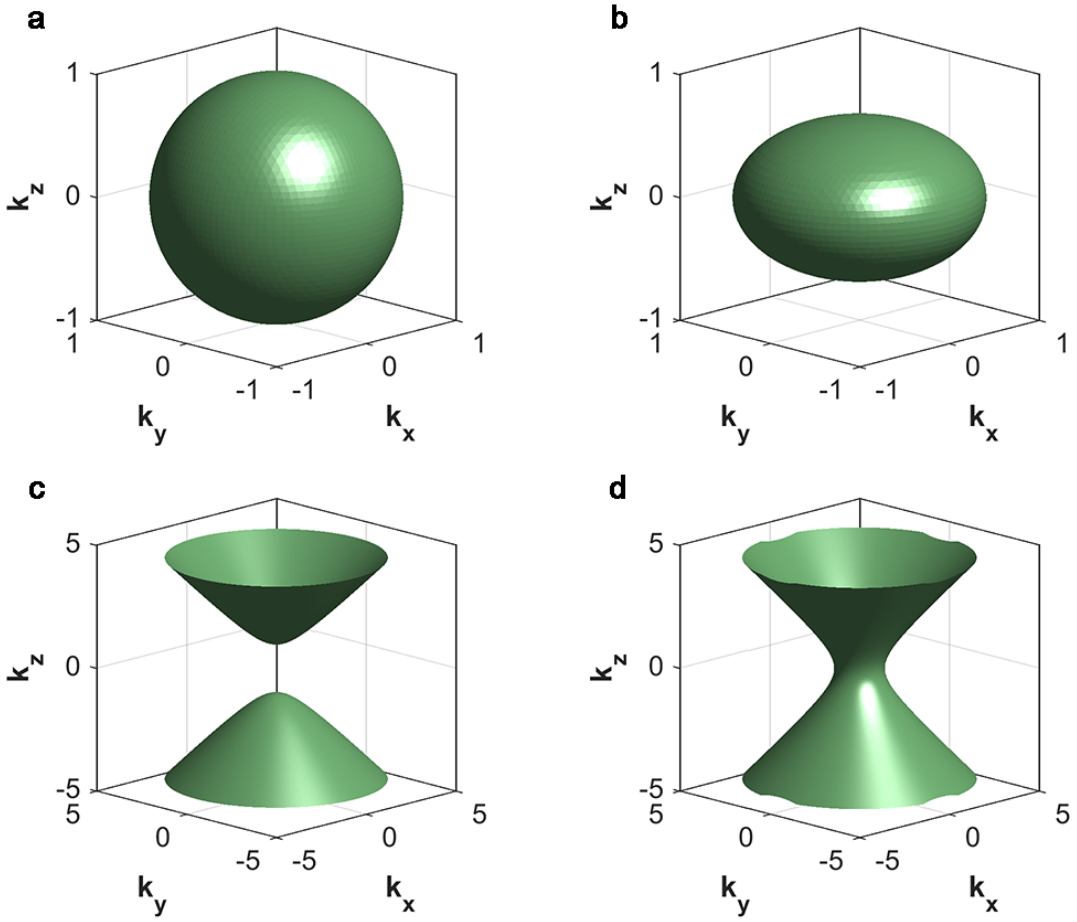

FIGURE 2.13: **Isofrequency surfaces for different types of media** given by $\omega(\mathbf{k}) = constant$. **(a)** Spherical isofrequency surface for an isotropic material with $\varepsilon_{xx} = \varepsilon_{yy} = \varepsilon_{zz} > 0$, **(b)** Elliptical isofrequency surface for a uniaxial material with $0 < \varepsilon_{xx} = \varepsilon_{yy} < \varepsilon_{zz}$, **(c)** Hyperbolic isofrequency surface for a uniaxial hyperbolic material of type I ($\varepsilon_{xx} = \varepsilon_{yy} > 0$ *and* $\varepsilon_{zz} < 0$) , **(d)** Hyperbolic isofrequency surface for a uniaxial hyperbolic material of type II ($\varepsilon_{xx} = \varepsilon_{yy} < 0$ *and* $\varepsilon_{zz} > 0$).

combines the properties of dielectric materials in one direction and those of reflective metals in the perpendicular direction [77, 78], leading to extreme anisotropy. This can be achieved for instance by designing metallo-dielectric multilayers with sub-wavelength thicknesses or metallic nanorod arrays in a dielectric matrix as represented in Figure 2.14 [79, 80]. The optical properties of these HMMs can typically be tuned from the ultraviolet spectral range to the mid-infrared by choosing appropriate materials [81]. Metals are required to exhibit good metallic properties in the wavelength range considered, whilst having low losses. This can be achieved by choosing metals with large absolute values of the real part of their dielectric permittivity and small values of the imaginary part, determining losses. While aluminium is used for applications in the ultraviolet spectral

range, metals such as silver or gold can be used in the visible spectral range, in conjunction with appropriate dielectrics such as aluminium oxide or higher refractive index materials such as titanium oxide or silicon nitrides [80]. Gold has also been shown to be applicable for nanorod-based hyperbolic metamaterials in the near-infrared wavelengths range [82]. However, in the case of metallo-dielectric multilayers, the high reflectivity of conventional plasmonic metals in the near-infrared spectral range causes high-impedance mismatch and thus low transmission [80, 81]. Therefore, research towards alternative plasmonic materials for this spectral range, such as oxides and nitrides, has emerged [83, 84].

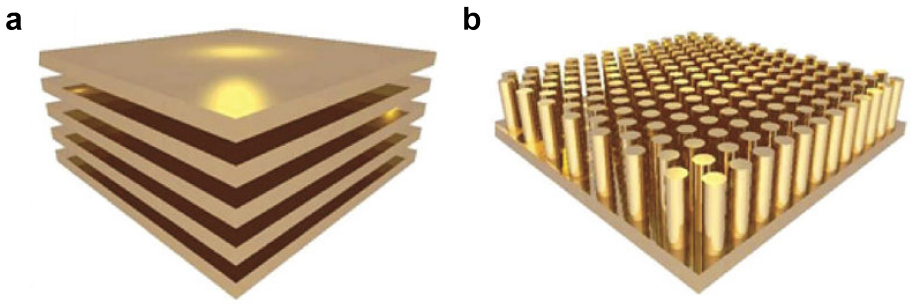

FIGURE 2.14: **Two types of hyperbolic metamaterials. (a)** Subwavelength metallo-dielectric multilayers, **(b)** Nanorod-based hyperbolic metamaterial. (from [85])

Historically, hyperbolic media were first investigated in the 1960s with the study of anisotropic plasmas and the predictions of negative refraction and planar focusing [86]. More recently, the high sensitivity of these composites to the local dielectric environment has led to their implementation as ultra-high sensitivity biosensors [74], hydrogen sensors [75] and ultrasound sensors [87]. The large density of photonic states available in hyperbolic dielectric environments constitutes a major advantage in their ability to enhance the spontaneous emission rate of emitters located in their vicinity via the Purcell effect [88–96]. In comparison with the well-known techniques involving cavities [97] or photonic crystal structures [98], the use of metamaterials for controlling spontaneous emission can lead to a broadband and frequency tunable enhancement of the spontaneous emission rate up to about 100 times, useful for biosensing and bioimaging applications or the development of bright and fast sources. The state of the art of the control of spontaneous emission using plasmonics will be developed in Chapter 3.

2.3.4 Plasmonic nanorod metamaterials

2.3.4.1 Geometrical properties

Nanorod-based metamaterials consist of quasiperiodic arrays of metallic nanorods oriented perpendicularly to a supporting substrate, as represented in Figure 2.14b and shown in the SEM images of Figure 2.15. The metallic nanorods are fabricated using electrodeposition into porous anodised aluminium oxide (AAO) templates, which are formed by self-organisation of subwavelength pores during the anodisation of a thin aluminium film. These processes will be described more details in Chapter 4. By controlling the dimensions of the pores in the template as well as the electrodeposition conditions, it is possible to control the geometry of the nanorods. The diameter and inter-rod spacing of the nanorods can vary respectively in the range of $20 - 80\ nm$ and $40 - 100\ nm$, while their length can be varied from tens to several hundreds of nanometers, depending on the thickness of the AAO template and the electrodeposition time [99, 100].

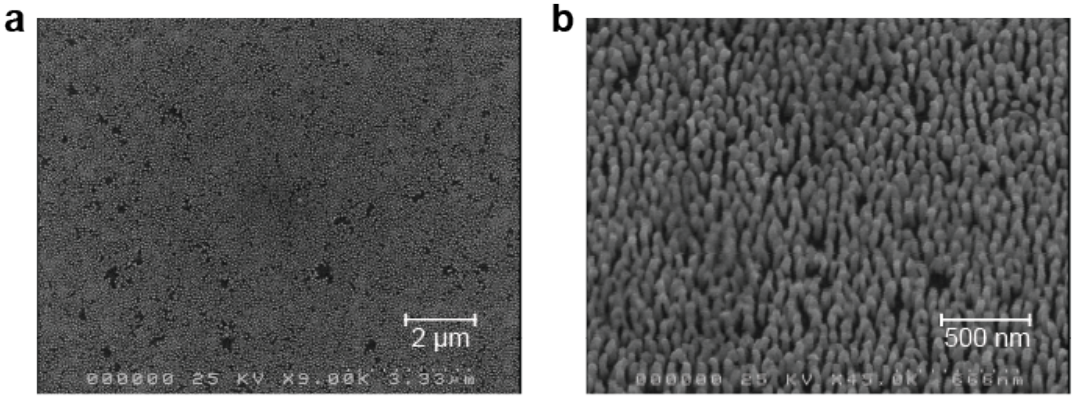

FIGURE 2.15: **Nanorod metamaterial. (a)** Top view and **(b)** tilted view of nanorod-based hyperbolic metamaterial.

2.3.4.2 Optical properties

The optical properties of this metamaterial, constituted of an assembly of nanorods, can be understood by first analysing the properties of an isolated nanorod, which in this case can be considered as a prolate spheroid with two principal axes corresponding to the length and the diameter of the rod. This type of particles exhibit two dipolar LSP resonances, a longitudinal plasmonic mode (L-mode) in the infrared spectral range and a transverse

plasmonic mode (T-mode) in the visible spectral range, respectively associated with the electron motion in the direction along and across the length of the nanorod. However, when placed in close proximity, like in the metamaterial considered, the dipolar longitudinal modes supported by each individual nanorod interact leading to a collective plasmonic resonance which is blue-shifted with regard to the longitudinal modes of each nanorod. By varying the aspect ratio of the nanorods (ratio between length and diameter), their separation and their surrounding environment, it is then possible to tune the plasmonic resonances of the system in the visible and near-infrared spectral ranges. Modifying the inter-rod spacing also affects the spatial distribution of the electric field associated with the L-mode resonance of the array. In the case of large inter-rod distances the field is concentrated around the extremities of the rods whereas for smaller separations, the coupling of the individual L-modes of the nanorods leads to the concentration of the electric field inside the metamaterial slab [100]. In addition to these two dipolar resonances, the nanorod-based metamaterial slab with finite dimensions, such as finite thickness, also supports waveguided modes, which also spectrally depend on the nanorod length, diameter and surrounding refractive index. Like SPPs, these modes are accessible using attenuated total internal reflection (ATR) spectroscopy.

2.3.4.3 Local effective medium theory

As mentioned in previous sections, for wavelengths much larger than all the characteristic sizes of the composite, such as nanorod diameter and their period, the macroscopic optical properties of such metamaterial can be theoretically analysed using a local effective medium theory approach based on the Maxwell-Garnett approximation. The Maxwell-Garnett mixing formula for anisotropic composites constituted of uniformly distributed and oriented prolate spheroids (principal axis oriented along the z-direction) describe the effective permittivity of the medium in terms of the permittivities of the materials constituting the meta-atoms and the filling factor of each individual meta-atoms [101, 102]. The in-plane and out-of-plane components of the effective permittivity are given by

$$\varepsilon_{xx}^{eff} = \varepsilon_{yy}^{eff} = \varepsilon_{\perp}^{mg} = \varepsilon_h \frac{(1+p)\varepsilon_{rod} + (1-p)\varepsilon_h}{(1+p)\varepsilon_h + (1-p)\varepsilon_{rod}} \tag{2.27a}$$

$$\varepsilon_{zz}^{eff} = \varepsilon_{\parallel}^{mg} = p\varepsilon_{rod} + (1-p)\varepsilon_h \tag{2.27b}$$

with ε_h and ε_{rod} respectively the permittivities of the host material and the rods, and $p = \pi\frac{r^2}{a^2}$ the filling factor of the metal in the host matrix with r the radius of the nanorod and a the periodicity of the array. This model can then be used to calculate transmission, reflection and absorption spectra of the composite using a transfer matrix method (TMM) [103], considering a metamaterial slab with thickness of the length of the rods. Due to symmetry, the optical properties of a nanorod metamaterial resemble those of an homogeneous anisotropic medium with the optical axis parallel to the nanorods and its dielectric permittivity can be expressed as a diagonal tensor of effective dielectric permittivity, like in equation 2.25 with $\varepsilon_{xx}^{eff} = \varepsilon_{yy}^{eff} \neq \varepsilon_{zz}^{eff}$. Figure 2.16 shows an example of the effective permittivity of the nanorod metamaterial where three regions can be distinguished relative to the sign of the real part of the dielectric permittivity along the nanorods: the elliptical regime, where $Re(\varepsilon_{xx}^{eff})$ is positive and the metamaterial behaves like a dielectric (green shaded region in Figure 2.16); the epsilon-near-zero (ENZ) region, where $Re(\varepsilon_{xx}^{eff})$ vanishes or approached zero (orange shaded region in Figure 2.16) and the hyperbolic regime, where $Re(\varepsilon_{xx}^{eff})$ is negative and the metamaterial has a metal-like behaviour (yellow shaded region in Figure 2.16).

2.3.4.4 Optical non-localities in nanorod metamaterials

In the limit of small losses and for a wavelength range close to the ENZ regime depicted in figure 2.16, it has been shown that the optical properties of metamaterials are largely affected by a non-local response of the composite [104]. Non-locality refers to the behaviour of a physical system at a given point depending on its state at another spatially separated region. In this ENZ wavelength range, strong spatial dispersion is observed and this non-local character of the metamaterial yields the propagation of not two, but three different modes: one of these modes is a TE-polarised ordinary wave, while the two other waves are both TM-polarised but have different effective indices. The additional TM-polarised mode in the case of nanorod-based metamaterials results from the collective excitation of

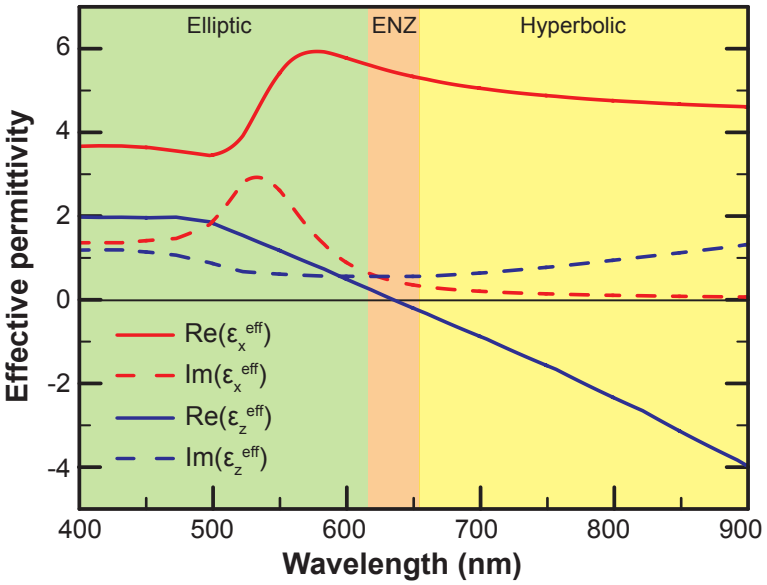

FIGURE 2.16: **Effective permittivity of nanorod based metamaterial in its AAO matrix.** The parameter of the nanorods are: length 300 nm, diameter 30 nm and period 60 nm.

cylindrical surface plasmons propagating along the nanorods [105]. The strong interaction of these two TM-polarised modes leads to a dispersion relation taking into account both local and non-local contributions given by

$$\left(k_z^2 - (n_z^l)^2 \frac{\omega^2}{c^2}\right)\left(k_z^2 - \varepsilon_\perp^{mg} \frac{\omega^2}{c^2}\right) = -\frac{\varepsilon_\perp^{mg}}{\xi} \frac{\omega^2}{c^2} k_x^2 \tag{2.28}$$

with $\xi = p\frac{\varepsilon_{Au}+\varepsilon_h}{\varepsilon_h-(n_\infty^l)^2}$, where p is the filling factor defined in section 2.3.4.3, n_z^l is the effective refractive index of the cylindrical surface plasmons that propagate in a nanorod metamaterial with the nanorod permittivity ε_{Au} and n_∞^l represents the limit of n_z^l for perfectly conducting nanorods. The parameters n_z^l and n_∞^l can be calculated either numerically or by solving an eigenvalue-type problem as described in [105].

2.3.4.5 Non-local effective medium theory

The non-locality mentioned above can be successfully described in a non-local EMT by introducing a wavevector dependence of the permittivity of the metamaterial. Hence, while the components of the dielectric permittivity tensor perpendicular to the optical axis

ε_{xx}^{eff} and ε_{yy}^{eff} can still be described using Maxwell-Garnett approximation in the non-local EMT, the component of the permittivity along the optical axis ε_{zz} becomes

$$\varepsilon_{zz}(k_z) = \xi \left(k_z^2 \frac{c^2}{\omega^2} - (n_z^l)^2 \right) \tag{2.29}$$

The transfer matrix method can subsequently be used to calculate the linear optical properties of the metamaterial slab. Although non-local effects are known to have a weak impact on linear reflection and transmission through the metamaterial, the situation can be completely different in the prediction of the spontaneous emission properties of emitters located inside such metamaterial, where the presence of an additional propagating mode inside the metamaterial, acts as a new decay channel for the emitters and fundamentally alters the local density of states. This will be discussed in details in Chapter 5.

Chapter 3

Control of spontaneous emission and non-radiative processes

In this chapter, the main steps in the development of a precise control of the spontaneous emission, as well as the non-radiative energy transfer between emitters via the engineering of the electromagnetic environment surrounding the emitters, will be discussed.

3.1 Local density of electromagnetic states and Purcell effect

The spontaneous emission of emitters in a specific environment can be characterised by the emission spectrum of the emitters and their lifetime, depending on both radiative and non-radiative decay channels. According to Fermi's golden rule [106], the radiative spontaneous emission rate of an emitter can be expressed as

$$\Gamma = \frac{\pi\omega_0}{3\hbar\varepsilon_0}|\mathbf{p}|^2\rho(\mathbf{r_0},\omega_0) \tag{3.1}$$

where $\mathbf{p}$ is the matrix element related to the transition between initial and final energy states and $\rho(\mathbf{r_0},\omega_0)$ is the local density of electromagnetic states (LDOS) corresponding to the number of modes per unit volume and frequency, at the position r_0 of the emitter, into which a photon of energy $\hbar\omega_0$ can be released during the spontaneous emission process

[33]. From this equation, two ways of modifying the spontaneous emission rate can be distinguished. The first one, associated with the transition dipole moment, is purely related to the chemical structure of the emitters and the initial and final energy levels involved in the transition. The second method, however, is not related to the emitters themselves but to their electromagnetic environment by means of a modification of the LDOS available for the emitters to decay. This possibility has first been observed by the pioneering work of Purcell in 1946, who discovered the enhancement of the spontaneous emission rates of atoms in the presence of a resonant cavity [88]. Therefore, the enhancement of the spontaneous emission rate of an emitter has taken the name of Purcell effect, which can be evaluated using the Purcell factor, defined as the ratio of the spontaneous emission rate of the emitters in the engineered environment to the one of the emitters in free-space. Since, the engineering of the LDOS has been achieved in various photonic and plasmonic environments leading to inhibition or enhancement of the spontaneous emission rate as will be described in the next sections. One of the main challenge of the evaluation of the spontaneous emission enhancement in various environments, and especially plasmonic ones, relies from the combined modifications of the radiative and also non-radiative decay rates due to the potential presence of losses channels and quenching mechanisms, leading to an increase in the spontaneous emission rate but a decrease in the emission intensity.

3.2 Spontaneous emission engineering

3.2.1 Planar metallic interface

The presence of an interface between two media of different refractive indices is one of the simplest example of modification of the LDOS in the vicinity of an emitter. This modification arises from the interferences between the emitted field from the emitter and the field reflected by the interface. The dependence of the spontaneous emission rate to the distance between the emitter and the surface was first experimentally shown by the pioneering work of Drexhage in the late 1960s and early 1970s [107, 108] with his work on europium ions near metallic mirrors, which was subsequently replicated and extended by Amos and Barnes in 1997 [109, 110].

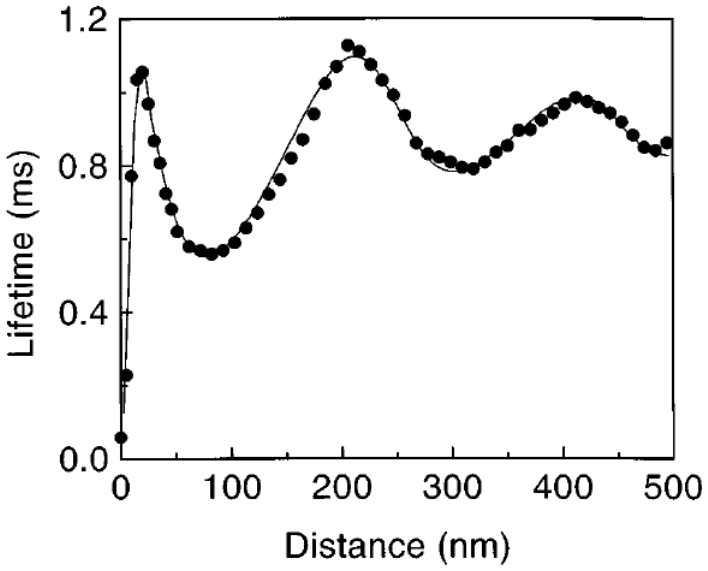

FIGURE 3.1: Excited state lifetime of Eu^{3+} ions as a function of the distance from a 200 nm thick silver mirror. Taken from [109].

Figure 3.1 shows the dependence in lifetime of Eu^{3+} ions as a function of the distance from a 200 nm silver mirror, where the oscillations in the lifetime of the ions is due to the phase difference between the emitted and reflected fields and the decrease in amplitude is the result of the radiated field decreasing as the square of the distance from the dipole. The different behaviour for short distances between the dipole and the planar interface leading to the fast decrease of the lifetime of the emitter can be attributed to non-radiative energy transfer to the metal, mainly due to the excitation of surface-plasmon polaritons (SPPs) at the metal surface but also to the coupling to lossy surface waves [111, 112], which become predominant at very short distances from the surface. Several experiments aiming at demonstrating the coupling between emitters and SPPs [113–115] and characterising the dependence of the coupling with regard to the distance between the emitters and the interface [116] were then performed. These experiments required the use of momentum-matching techniques such as prism or grating coupling. It has also been shown that the use of an optically thin film as a mirror not only allows the propagation of SPPs on the closer side of the metal but also on the far side of the film; resulting in another decay channel and hence, a further decrease in the lifetime of the emitters [117]. This has been discussed in [109]. Another decay mechanism can also take place in the case where the spacer layer is thick enough leading to the presence of waveguided modes [110] constituting new decay channels for the emitters.

3.2.2 Corrugated interfaces

The non-radiative character of the emitted light coupled to SPPs naturally drove the research towards the use of roughness or corrugated surfaces in order to couple the light back to radiative modes and take advantage of the density of states associated with SPPs.

The out-coupling of SPPs to radiative modes is made possible by momentum-matching techniques via the periodic patterning of the planar surface. Out-coupling of luminescence from dye molecules into SPPs by silver gratings for TM-polarised light and enhancement of emission was first experimentally demonstrated by Knoll *et al.* in 1981 [118] and followed by the work of Adams, who also investigated the excitation of waveguided modes [119]. For these methods, the radiation patterns are strongly modified, leading to a specific angular distribution and polarisation of the emission [120]. Several experimental studies have then shown that the careful design of the grating geometry can allow the modification of the decay rate of the emitters and also enhancement of the emission [121–123]. Another way to couple SPPs and waveguided modes to radiation is to use roughened or multi-corrugate surfaces, which has been shown to allow enhancement of the emission of emitters with respect to planar surfaces [3, 124]. Some work on emission enhancement has also been done using another type of substrate made of subwavelength metallic islands covered with dye molecules. In this case, the scattering from the islands allows the coupling of the propagating SPPs to radiation and the small sizes of the islands, which can be considered as particles of various shapes, leads to the presence of localised modes also taking part in the control of spontaneous emission. Similarly to the case of surfaces with small roughness, optimised distances between the islands and the molecules allow an enhancement of the fluorescence emission and an increase in the decay rate of the emitters situated in the localised "hot-spots", leading to a higher photostability, essential to biosensing and bioimaging applications [125]. However, due to the size and shape distributions of the particles, it is very difficult to predict the efficiency of enhancement of these structures, even across a same sample.

3.2.3 Metallic nanoparticles

As explained in the case of roughened surfaces, the localisation of light plays an important role in the enhancement of the emission from emitters placed in their vicinity. Hence,

emission enhancement has also been studied in systems constituted of subwavelength single or multiple metallic nanoparticles. Enhancement properties are significantly dependent on the careful design of the geometry of the particles, their material constituents and the control of their arrangements and various types of systems have been studied.

For instance, the interaction between emitters paired with single nanoparticles of different shapes such as nanospheres [126], nanodisks [127] as well as nanorods [128] or nanoprisms [129] has been largely investigated. By tuning the shape, size and composition of these subwavelength nanoparticles, it is possible to finely tune the spectral position of the LSP resonances over the whole visible and near-infrared spectral ranges in order to optimise the correspondence between the LSPs of the nanoparticles and the spectral properties of the emitters and thus improve the coupling between them. Different factors can influence the emission properties of the emitters, such as the high localised fields at the nanoparticle surface able to enhance the excitation intensity incident on the emitters; the modification of the decay rate due to the modified LDOS and also the efficient coupling to radiative modes thanks to the nanoparticle scattering [130]. Like in the case of surfaces, the distance between the emitter and the nanoparticle has a dramatic effect on the emission of emitters leading to either quenching or enhancement due to the competing non-radiative and radiative decay channels available to the emitters [131] as represented in Figure 3.2.

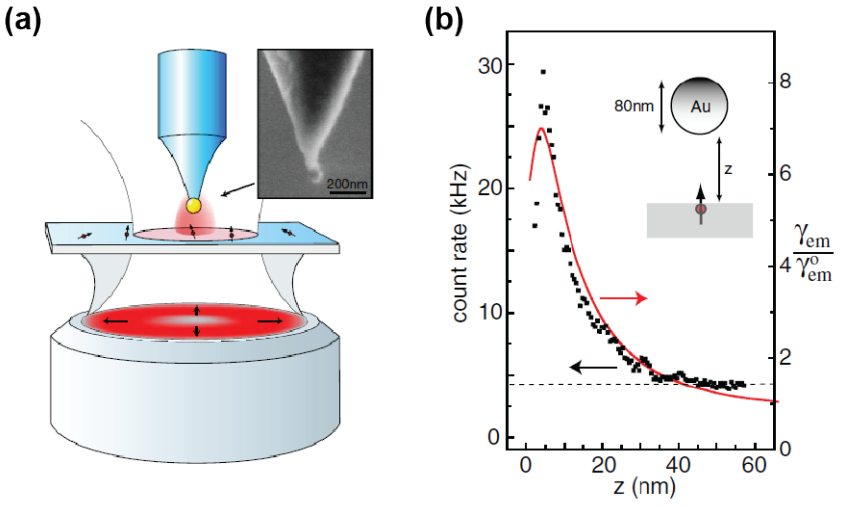

FIGURE 3.2: **Fluorescence near nanoparticles. (a)** Schematic of experimental setup for fluorescence detection (Inset: SEM image of a gold particle attached to the end of a pointed optical fiber). **(b)** Experimental fluorescence rate γ_{em} as a function of molecule-particle separation (normalised to free-space value γ^{0}_{em}. Taken from [131].

For nanoparticles in contact with the emitters or very short distances, the emission is strongly quenched [132, 133]; while, for optimised separations of only few nanometres, maximum enhancement factors are observed and can reach 50 when the LSP resonance of the nanoparticle is matched to the emission wavelength of the emitter [128]. Other studies have also shown a 20-fold enhancement of the emission in the case where the LSP resonance of the nanoparticle is matched to the excitation peak of the emitter [134], showing the important role of LSPs in both the control of excitation and emission processes. The decay rate of emitters is also increased [126, 134] due to the modification of the local density of states available for spontaneous emission compared to that in free-space. In the case of non-symmetric particles, such as nanorods, a strong polarisation dependence of the emission enhancement has been observed due to selective excitation of LSP resonances [135]. As nanoparticles have been shown to enhance spontaneous emission, subwavelength apertures drilled in metallic films have also received a lot of interest since the discovery of the enhanced transmission phenomenon [136]. Several experimental studies demonstrated spontaneous emission intensity and decay rate enhancements in isolated single holes due to the enhancement of the excitation intensity by confinement together with the enhancement of emission via the modification of the LDOS [137, 138].

3.2.4 Plasmonic nanoantennas

In order to further improve the emission and decay rate enhancements of emitters, combinations of the above mentioned nanoparticles have also been investigated. Typically fabricated using chemical processes or electron-beam lithography, these types of structures allow more flexibility than a single nanoparticle in that not only the shape, size and composition of the particles can be tuned, but also the separation between them. Structures such as nanoparticle dimers or bowtie antennas [139, 140], as shown in Figure 3.3, combine strong resonances, due to the coupling of the individual modes of the particles, together with a high local field enhancement in the nanoscale gap between the particles, leading to strong enhancement of the spontaneous emission of emitters located in the vicinity of the antenna gap.

This enhancement is highly dependent on polarisation, with higher enhancements when the electric field is along the axis of the nanoantennas, and on the gap between the particles

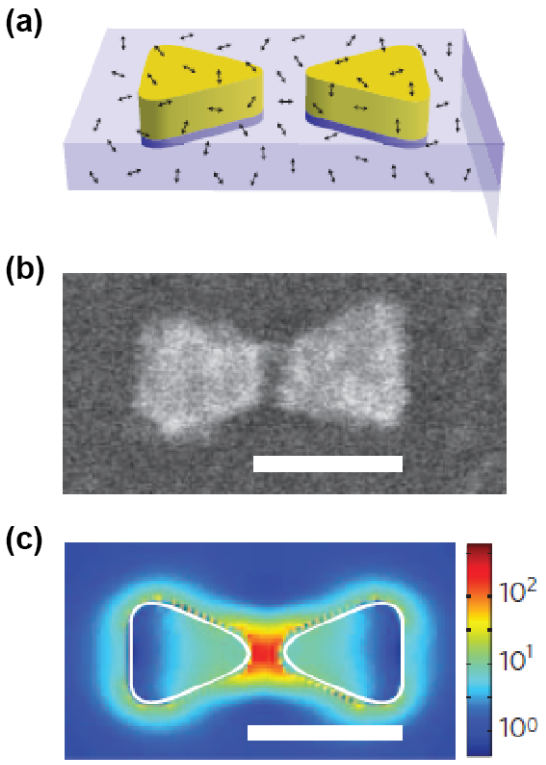

FIGURE 3.3: **Fluorescence near nanoantennas. (a)** Schematic of a bowtie nanoantenna coated with molecules in PMMA on a transparent substrate. **(b)** Scanning electron microscopy image of a gold bowtie nanoantenna. **c** Finite-difference time-domain calculation of local intensity enhancement. Scale bar 100 *nm*. Taken from [139].

[141–143]. Experimental studies have reported enhancement factors of the emission higher than for isolated nanoparticles, reaching values of the order of 10^3 in optimised cases [139]. Authors have demonstrated in various studies that the enhancement of emission intensity can be accompanied by an up to 30-fold increase of the decay rate of the emitters [139, 144], polarised emitted light [145] and reshaping of the emission spectrum of the emitters according to the spectral position of the resonance of the antenna [143, 145]. Various other designs including Yagi-Uda [146, 147] antennas; nanoapertures surrounded by gratings [148, 149]; or patch antennas consisting of emitters placed in the small gap between a metallic film and a metallic nanoparticle [150–152], have been used in order to achieve high-directionality of the emission. These studies report a high directional enhancement of the spontaneous emission along with high decay rates reaching enhancement factors up to 880 and 2300-fold enhancement in the total fluorescence intensity, useful for the design of fast single-photon sources [153].

3.2.5 Plasmonic/photonic crystals and cavities

Nanoparticles or nanoapertures can also be arranged in periodic arrays known as plasmonic crystals. When placed far enough apart, the nanoparticles forming the array don't interact with each other and the electromagnetic response of the array is similar to the electromagnetic response of each nanoparticle. However, when the periodicity of the nanoparticles is reduced to values of the order of the wavelength, the coupling between their individual electromagnetic responses modifies the response of the whole structure. Coupling to these collective modes led to both spontaneous emission and decay rate enhancement when overlapped with the emission spectrum of the emitters [154, 155], but also directional and polarisation dependent photoluminescence enhancement [4, 156, 157].

The work on plasmonic crystals and cavities for the control of spontaneous emission enhancement has been driven by previous research based on the use of photonic systems, such as photonic crystals and photonic cavities. Experimental studies of emitters in photonic crystals have shown the possible control of spontaneous emission in 3D photonic crystals [98, 158], but also in 2D photonic crystals [159]. In cavity-based systems, the modification of the LDOS and hence of the spontaneous emission rate enhancement can be evaluated by the following expression [88]

$$F_p = \frac{3}{4\pi^2}\left(\frac{\lambda}{n}\right)^3\left(\frac{Q}{V}\right) \tag{3.2}$$

where $\frac{\lambda}{n}$ is the wavelength in the host material, and Q and V are the quality factor and mode volume of the cavity, respectively representing the photon confinement with respect to time and space. High enhancement of the LDOS can therefore be achieved by designing cavities with high quality factors and small mode volumes.

Spontaneous emission can then be further controlled by introducing point defects in 3D and 2D photonic crystals as represented in Figure 3.4 and thus form photonic crystal cavities with very high quality factors and the smallest mode volume shown in dielectrics.

Spontaneous emission enhancement has also been demonstrated in other types of cavities such as micropillars or microdisks cavities [161]. Due to their very sharp resonances, photonic crystal cavities are also more suitably adapted for spontaneous emission enhancement of emitters with narrow emission linewidths.

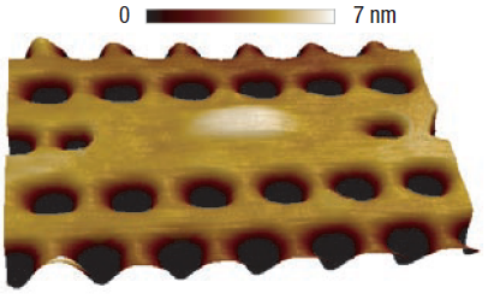

FIGURE 3.4: **AFM topography of a photonic crystal cavity** aligned to a hill of material on the surface arising from a QD buried 63 *nm* below. Taken from [160].

Compared to photonic cavities, plasmonic cavities have more moderate quality factors due to the losses introduced by metals. However, they have the advantage of showing very small mode volume to the presence of strongly bound SPPs at a metal-dielectric interface and hence show very high theoretical Purcell factors. In terms of experiments, large spontaneous emission enhancement of emitters located in the gap between a planar metallic film and a metallic nanowire has been demonstrated due to the coupling of the emitters to the gap-modes sustained by the cavity [162].

3.2.6 Hyperbolic metamaterials

Recently, metamaterials have received a lot of attention and have been shown to constitute an interesting alternative to photonic cavities in order to achieve non-resonant broadband spontaneous emission enhancement without the need of high confinement [90, 163]. Due to their open isofrequency surfaces, hyperbolic metamaterials, as described in Chapter 2, exhibit unique high-wavevector states and hence a theoretically infinite LDOS. This ultimately makes them perfect candidates for the control of spontaneous emission over large bandwidths, as $\Gamma(\omega) \propto \rho(\omega, r)$, where $\Gamma(\omega)$ is the spontaneous emission rate and $\rho(\omega, r)$ the LDOS at the position r of the emitter. The first experimental investigations of the enhancement of spontaneous emission with hyperbolic metamaterials were performed in 2010 with the study of the optical properties of dye-doped layers deposited on top of a silver nanorod-based metamaterial [90] and a metallo-dielectric multilayer system [164], both exhibiting hyperbolic dispersions. Time-resolved fluorescence measurements showed a reduction of the lifetime of the emitters by a factor of about 2, due to the presence of the unique electromagnetic states propagating in the metamaterial. Since

then, the enhancement of the decay rate of various type of emitters, such as quantum dots, nanodiamonds and organic dyes, has been demonstrated only using metallo-dielectric multilayer metamaterials with the aim of investigating the effect of the transition from elliptic to hyperbolic regime [94, 163, 165]. In order to further increase the radiative decay rates, emitters have then been placed inside the hyperbolic metamaterial, as the high-wavevector states present in hyperbolic metamaterials are propagating within the layers and the emitters experience higher confinement [166]. Theoretical studies have demonstrated the position and polarisation dependence of the enhancement of the radiative decay rates [92], and measured enhancements have been shown to be higher than on top of the multilayers, but remain moderate [167]. Hence, recent work has been focused on the out-coupling of the light coupled to the modes supported by the HMMs to the far field by direct nanopatterning of the HMM or addition of an out-coupling structure on top of the HMM. 1D gratings on metallo-dielectric multilayers covered with dye-doped layers have been theoretically and experimentally investigated, leading to a 76-fold enhancement of the spontaneous emission rate and about 80-fold enhancement of the emission intensity compared to the same HMM without nanostructure [92, 93]. Another design, consisting of cylindrical dielectric bullseye grating, has been theoretically studied on top of multilayered HMMs and its potential for highly directional out-coupling of the high-wavevector modes of the HMMs [166] has been shown. This design has then been applied experimentally to study the simultaneous spontaneous emission enhancement and out-coupling of high-wavevector modes of quantum dots embedded in a metallo-dielectric multilayer HMM. The results of this study led to a 10-fold enhancement of the spontaneous decay rate along with a 20-fold enhancement of the emission intensity [168].

In all these experimental studies, the spontaneous emission and out-coupling efficiencies have been shown to be highly dependent on the design of the HMMs, or their nanostructuring, as well as the location of the emitters with regard to the HMM. In this thesis, the tailoring of the spontaneous emission of emitters placed inside a nanorod-based HMM will be discussed. The inexpensive and straightforward fabrication process of this type of metamaterial, along with the high tunability of their geometrical properties, confer significant advantages with regard to the difficulties encountered in fabricating high quality factor metal-dielectric multilayers at nanoscale. The nanorod-based HMM geometry also provides significant advantages with regard to the positioning of the emitters inside the

metamaterial as the largest Purcell factors are obtained for emitters placed in the local field maxima [169] of the structure, which, for this type of HMM, is found to be concentrated between the nanorods within the assembly [100].

3.3 Energy transfer engineering

In the same way the spontaneous emission can be controlled by the design of suitable electromagnetic environments, research towards the engineering of non-radiative processes between emitters such as FRET has recently gained interest. Among the theoretical and experimental studies of FRET in nanophotonic environments developed over the past years, the influence of the LDOS on the energy transfer rate remains unclear, if mentioned at all, and several contradictory results have been obtained. In this process, the energy transfer between donor and acceptor is typically competing with other processes; such as the modifications of the donor and acceptor emission properties as well as losses to the metal, which are all influenced by the LDOS. Therefore, the careful design of the nanostructure is required in order to optimise the contribution of FRET with regard to all the other decay pathways available to the emitters.

A lot of the studies of the interaction of donor-acceptor FRET pairs with metallic nanoparticles, based on the coupling between the energy transfer and the LSP resonances exhibited by the metallic nanoparticles, have reported enhancement of the energy transfer rate, efficiency and range, depending on the geometry of the systems, but have generally not linked it to the change in the LDOS. Various systems have been investigated including a single metallic nanoparticle with a single donor-acceptor pair suggesting a 21-fold increase in the FRET rate together with an increase in the FRET radius [170], core-shell structures [171] and also nanoparticle arrays separating two monolayers of donor and acceptor emitters, leading as well to an increase of the FRET rate and the Förster radius compared to FRET without the nanoparticles [172, 173].

Among the work mentioning the relation between energy transfer and FRET rate, different types of dependences between the energy transfer rate and the LDOS have been suggested. Early studies using high quality factor microcavities, known to enhance the spontaneous emission of emitters, have shown an enhancement of the energy transfer rate up to 10 times. FRET rates following a linear dependence to the LDOS at the donor's emission

wavelength were shown and attributed to the alteration of the donor's oscillator strength by the microcavity [174, 175]. The same linear dependence was also first claimed in a study of energy transfer near a gold film, where the typical oscillations of the decay rate with distances from the metal film could be observed as well for the energy transfer rate [176]. A quadratic dependence of the FRET rate on the LDOS was subsequently modelled [177]. The FRET rate has also been shown to be nearly independent on the LDOS in the case of dielectric materials doped with donor and acceptor ions and immersed in solvent of different refractive indices [178, 179].

It is important to notice that most of these studies were taking into account ensembles of molecules and that potential disparities in the result of the relationship between FRET rate and LDOS could be the result of an imprecise control over the donor-acceptor distance, the pairing of a donor to multiple acceptors or cross-talk between donor-acceptor pairs [180]. Therefore, in order to minimise the influence of these factors, many of the recent studies of FRET and LDOS have considered single donor-acceptor pairs at well-defined distances from engineered electromagnetic environments. An experiment carried out for donor-acceptor pairs at fixed distances from a planar mirror [180] led to an energy transfer rate independent from the LDOS and similar conclusions were then drawn in studies involving microresonators, while varying the separation between the mirrors [181, 182]. Furthermore, inhibition of FRET was observed for donor-acceptor pairs located on top of metallo-dielectric multilayer metamaterials and the potential influence of collective behaviours on the modification of the energy transfer rate has been mentioned [183]. This collective behaviour has also recently been theoretically investigated in the case of metallic nanoparticles and planar mirrors [184, 185], highlighting the presence of new collective modes influencing the energy transfer rate. In contrast with these observations, a linear dependence of the FRET rate on the LDOS has been demonstrated in nanoapertures of different diameters in a gold film [186], as well as nanogap antennas [187] for different separations between donor and acceptor, leading to a 5-fold enhancement of the FRET rate but reduced efficiencies. These enhancements of the FRET rate have been attributed to the strong field gradient on the scale of the donor-acceptor separation [187, 188].

Several remarkable properties of FRET in electromagnetic environments with higher LDOS have been highlighted in these experimental investigations. Larger enhancement of the FRET rate have generally been observed for larger separations of the donor and acceptor.

This has been attributed to the fact that for short donor-acceptor distances, the direct dipole-dipole transfer is dominant; whereas, for larger separations, the contribution from the local environment of the emitters on the energy transfer is more pronounced [186]. Meanwhile, the increase in the FRET rate has often been accompanied with decreased FRET efficiencies due to the faster increase of the donor decay rate with regard to the FRET decay rate. Taking into account that the LDOS available to an emitter varies strongly with the position of the emitter in its environments, a precise positioning of the donor-acceptor pairs is advantageous.

Chapter 4

Experimental methods and simulations

This chapter gathers the experimental techniques for fabrication and characterisation of the samples as well as the methods used for data analysis. Firstly, general methods such as thin film sputtering, anodisation and electrodeposition used to fabricate the nanorod-based hyperbolic metamaterial will be described. The next section is dedicated to the standard characterisation techniques used in order to study the electromagnetic properties of the samples. Finally, the development of a time-resolved fluorescence microscopy setup to study the spontaneous emission of emitters in various electromagnetic environments will be presented together with data analysis methods.

4.1 Fabrication techniques

4.1.1 Sputtering

The first step in the fabrication of the nanorod-based hyperbolic metamaterials mainly used in the experiments performed in the following chapters is the deposition of thins films of tantalum pentoxide (Ta_2O_5), gold (Au) and aluminium (Al) in order to then produce the porous templates in which the nanorods will subsequently be embedded. This is done by physical vapour deposition (PVD) with a technique called magnetron sputtering. PVD consists in a vaporisation process where atoms of the material to deposit

are physically ejected from a solid source by bombardment and momentum transfer from energetic positively charged ions of an inert gas onto the target [189].

In the case of the nanorod-based HMM samples made for the following experiments, a 10 nm underlayer of tantalum pentoxide (Ta_2O_5) is typically sputtered onto a glass substrate followed by a thin ($7-10$ nm) layer of gold (Au) and finally a film of aluminium (Al) with a thickness of several hundreds of nanometers which is subsequently anodised to form a porous template. The deposition of an Ta_2O_5 layer is essential to the process as it constitutes an adhesion layer between the glass substrate and the gold layer, while the gold layer acts as an electrode for the electrodeposition of the material into the pores of the AAO template. Other samples such as simple gold thin films of various thicknesses were also fabricated using the same sputtering process of a 10 nm underlayer of Ta_2O_5 and the desired thickness of gold.

4.1.2 Anodisation

The fabrication of the arrays of nanorods discussed in Chapter 2 relies on the production of a layer made of a quasi-periodic array of holes with nanometric diameters and separations, acting as a template for further electrodeposition of the nanorods. The generation of these holes uses a process of controlled anodisation of aluminium, leading to the formation of porous alumina known as Anodised Aluminium Oxide (AAO). The process of anodisation of aluminium films occurs with the chemical reaction between the metal and an electrolytic solution when a voltage is applied through the solution and the metallic film is used as the anode. The pores diameter and separation can be controlled by the voltage applied and the type of acid used as the electrolyte. The use of sulfuric (H_2SO_4) or oxalic ($H_2C_2O_4$) acids at voltages between $20V$ and $60V$ typically result in pore diameters ranging from 12 nm to 60 nm and separations from 50 nm to 150 nm. Prior to the deposition of the metal in the pores, it is necessary to remove the barrier layer present at the bottom of the pores which insulates the electrode. Therefore, an etching process in a solution of 30 $mmol/L^{-1}$ sodium hydroxide ($NaOH$) is required. This process also slowly widens the diameter of the pores.

A two-step anodisation process can also be used in order to achieve highly ordered nanorods. This process consists in a first step anodisation of the aluminium film, during which the

formation of the pores randomly develops over the aluminium surface and gradually orders after long-period anodisation. The AAO layer created is then etched away in a solution of phosphoric acid H_3PO_4 (3.5 %) and chromic acid CrO_3 (20 $g.L^{-1}$) at 70^o, leaving the aluminium surface with small highly ordered dents in order to perform a second anodisation [190] before etching the barrier layer. Figure 4.1 depicts the standard fabrication steps of the nanorod-based metamaterial.

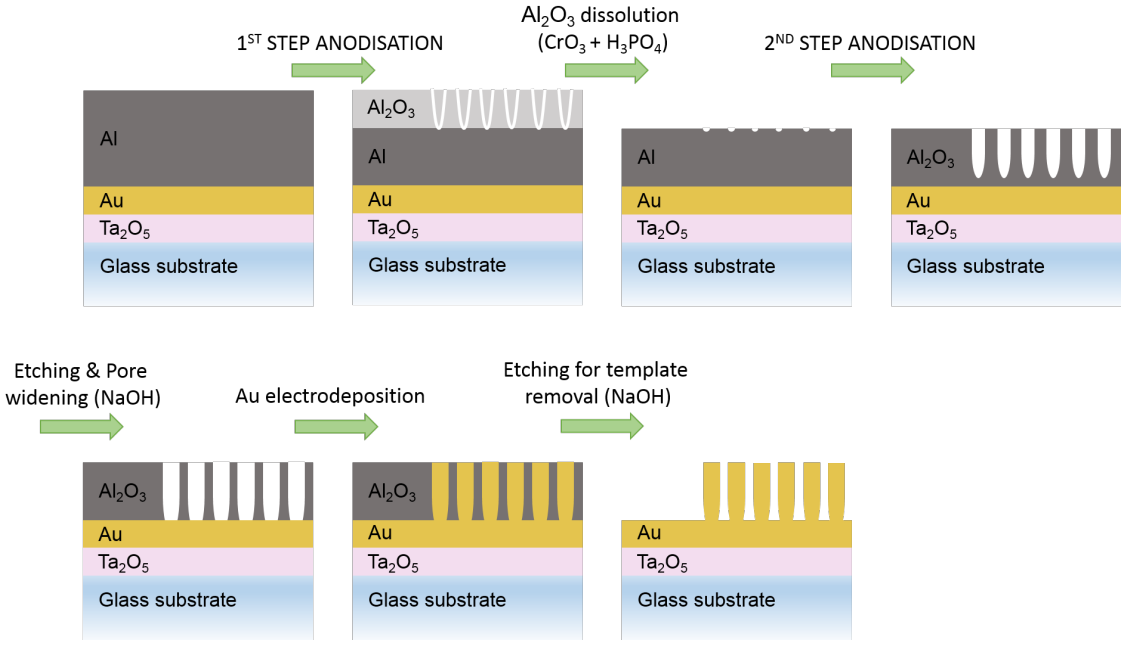

FIGURE 4.1: **Standard fabrication steps of the nanorod-based metamaterial.**

4.1.3 Electrodeposition

The nanorod system is then finally fabricated by electrodeposition of gold into the pores from a gold chloride based solution. The time of electrodeposition determines the length of the nanorods. For certain types of measurements, it is possible to completely dissolve the AAO template in order to obtain free-standing rods. This is achieved using the same etching process as described above. This then allows the placing of quantum dots, nanodiamonds or organic dyes solutions or polymeric layers in between the rods.

FIGURE 4.2: **Nanorod-based metamaterial sample. Left:** Sample following the anodisation, after the etching process, **Middle:** After gold deposition and **Right:** After removal of the AAO matrix (bottom part).

4.2 Characterisation techniques

4.2.1 Transmission/absorption and scattering spectroscopy

In order to characterise the optical properties of the samples or the emitters used, transmission measurements were taken using a tungsten-halogen lamp for varying polarisation or angles of incidence. Depending on the nature of the measurement, the incident light is either collimated or focused on the sample and, after passing through it, is collected using an objective lens. The transmitted light is then coupled to a spectrometer equipped with a CCD camera via a multimode optical fibre. Dark field illumination could be achieved by changing the illumination angle via a rotating arm. Figure 4.3 shows a typical setup.

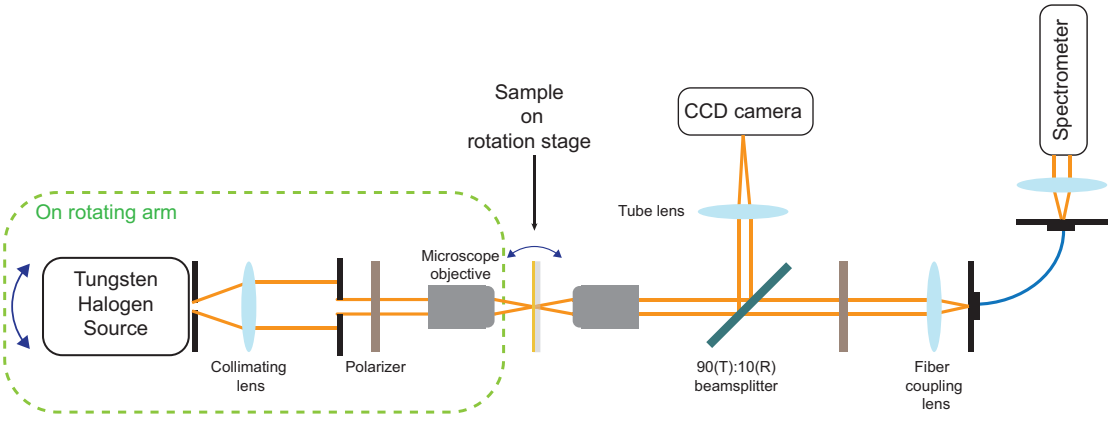

FIGURE 4.3: **Visible spectroscopy setup.**

4.2.2 Attenuated Total Reflection

To further probe the optical response of the samples and detect modes that are not available from free-space such as waveguided modes, Attenuated Total Reflection (ATR) measurements was used. In this configuration, the sample is placed in contact with a semi-cylindrical prism matching the refractive index of the sample's substrate and is illuminated through the semi-cylinder as shown in Figure 4.4. The minimum angle θ_c at which total internal reflection occur, called the critical angle, depends on the refractive indices of the semi-cylinder (n_1) and the sample (n_2) and is expressed as

$$\theta_c = sin^{-1}\left(\frac{n_2}{n_1}\right) \tag{4.1}$$

The incident beam passing through the semi-cylinder reflects from the internal surface in contact with the sample and creates an evanescent wave which extends into the sample. The penetration depth of the beam in the sample, given by the equation

$$d_p = \frac{\lambda}{2\pi(n_1^2 sin^2\theta - n_2^2)^{\frac{1}{2}}} \tag{4.2}$$

where λ is the wavelength of the light and θ is the angle of incidence of the beam relative to the normal of the semi-cylinder surface. The light not absorbed by the sample is reflected and then collected using an objective lens. The reflected light is then coupled to a spectrometer equipped with a CCD camera via a multimode optical fibre.

4.3 Time-resolved fluorescence spectroscopy

Time-resolved measurements, performed either in the time domain or frequency domain, provide information about intensity decay of the sample, which typically are single-exponential or multi-exponential. Complex intensity decays can for instance be the result of heterogeneity, resonance energy transfer or emitter-solvent interactions but also depend significantly on the local electromagnetic environment in which the emitters are placed. The following sections will briefly describe the different methods for time-resolved measurements and then focus on the experimental setup developed for this thesis.

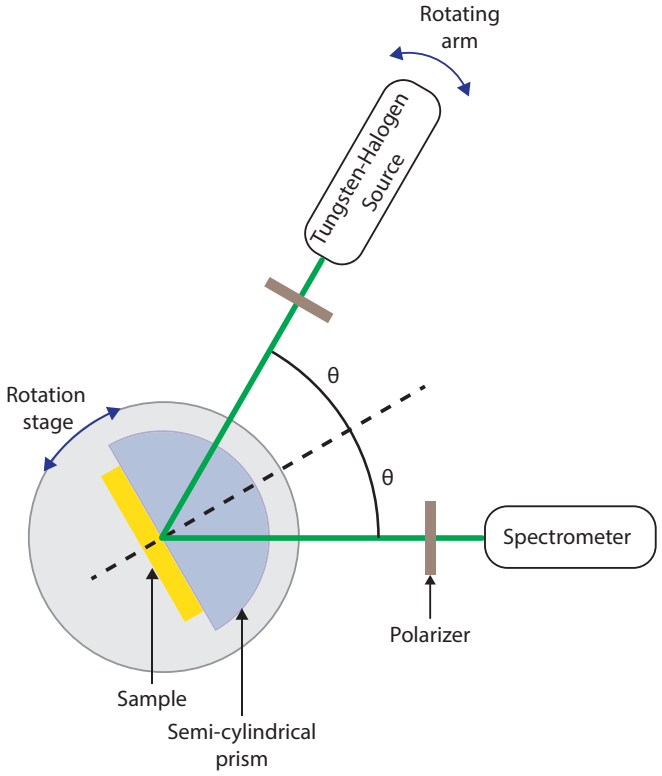

FIGURE 4.4: **ATR setup.**

4.3.1 Time-domain methods

Time-domain methods use a pulsed light source synchronised with high-speed detectors and electronics in order to record the time dependent intensity decay law of the sample after excitation. These measurements have so far been performed using different techniques, such as gated image intensifiers together with Charge-Coupled Device (CCD) cameras [191, 192] or Time-Correlated Single Photon Counting (TCSPC) [193]; having different time resolutions. In the case of the TCSPC technique, the time resolution only depend on the time response of the detector [194]. This time response varies depending on the type of detector used: usually of several hundreds of picoseconds for conventional photomultipliers (PMTs), it can reach only 50 ps for single-photon avalanche photodiodes (SPADs). Shorter lifetimes can then be determined by deconvolution of the instrumental response function from the recorded fluorescence decay [195].

4.3.2 Time-correlated single photon counting

4.3.2.1 Principle of TCSPC

The principle of TCSPC consists in measuring the time difference between the excitation of a fluorophore by a light pulse and the following emission of a single photon characteristic of the de-excitation of the fluorophore. By repeating this operation it is then possible to build the histogram of the times recorded, which corresponds to the fluorescence decay rate of the emitters. This technique relies on the fact that the probability of recording more than one photon per pulse is negligible due to the low-level and high-repetition rate (20-80 MHz) of the excitation signal. Figure 4.5 depicts a typical experimental TCSPC setup. The excitation path is split in two beams consisting in a small amount of the signal diverted onto a photodiode (PD) and the other part going to the microscope and hitting the sample. The fluorescence signal is then directed onto a single-photon detector delivering pulses for the individual photons detected. These pulses, as well as references pulses, are then sent to a TCSPC module.

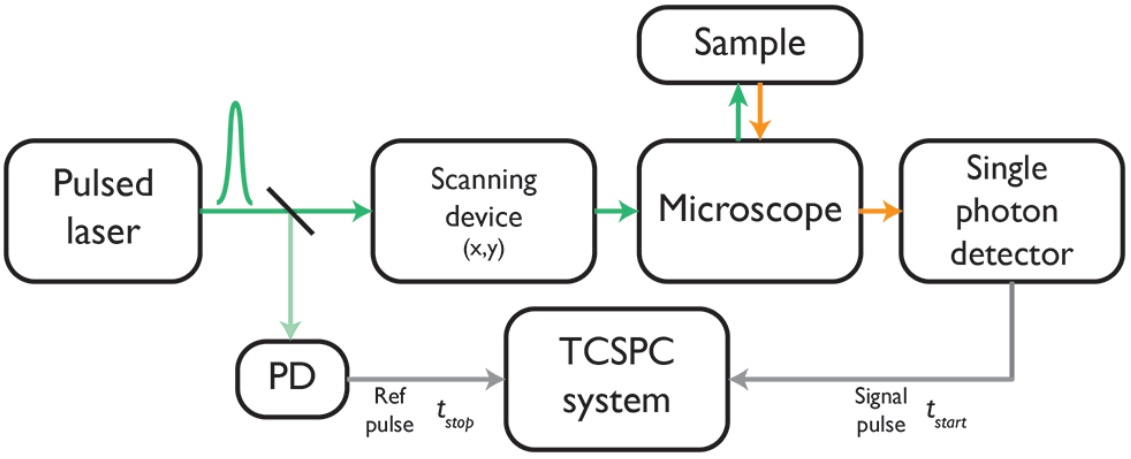

FIGURE 4.5: **Principle of TCSPC.**

The time difference measurement is then calculated via fast electronics described in more details in Figure 4.6a. A Constant-Fraction Discriminator (CFD) allows the detection of the signal pulse and a second CFD is then used to get a reference pulse from the light source. The outputs of these two CFDs are then used to start and stop a Time-to-Amplitude Converter (TAC), which will generate an output signal proportional to the time between the two pulses. This signal is sent to an Analog-to-Digital Converter (ADC), whose aim is to address a memory location corresponding to the time of the photon. The distribution

of photons over time is progressively built up (Figure 4.6b). TCSPC can also be used to perform Fluorescence Lifetime Imaging Microscopy (FLIM) which consists in an imaging technique based on the fluorescence decay rate of fluorescent molecules. Thus, each pixel of the image displayed corresponds to the fluorescence lifetime of the sample. This technique requires a scanning device which can be either an optical scanner, consisting in scanning the optical beam on the sample, or a scanning piezo-stage, where the sample is moving and the illumination is fixed. The TCSPC module is synchronized with the scanning device thanks to three different clock pulses (frame clock, line clock and pixel clock) allowing the determination of the beam position within the scanning area. In this case, not only the photons time is used to build up the distribution but also the spatial coordinates X and Y (Figure 4.6c).

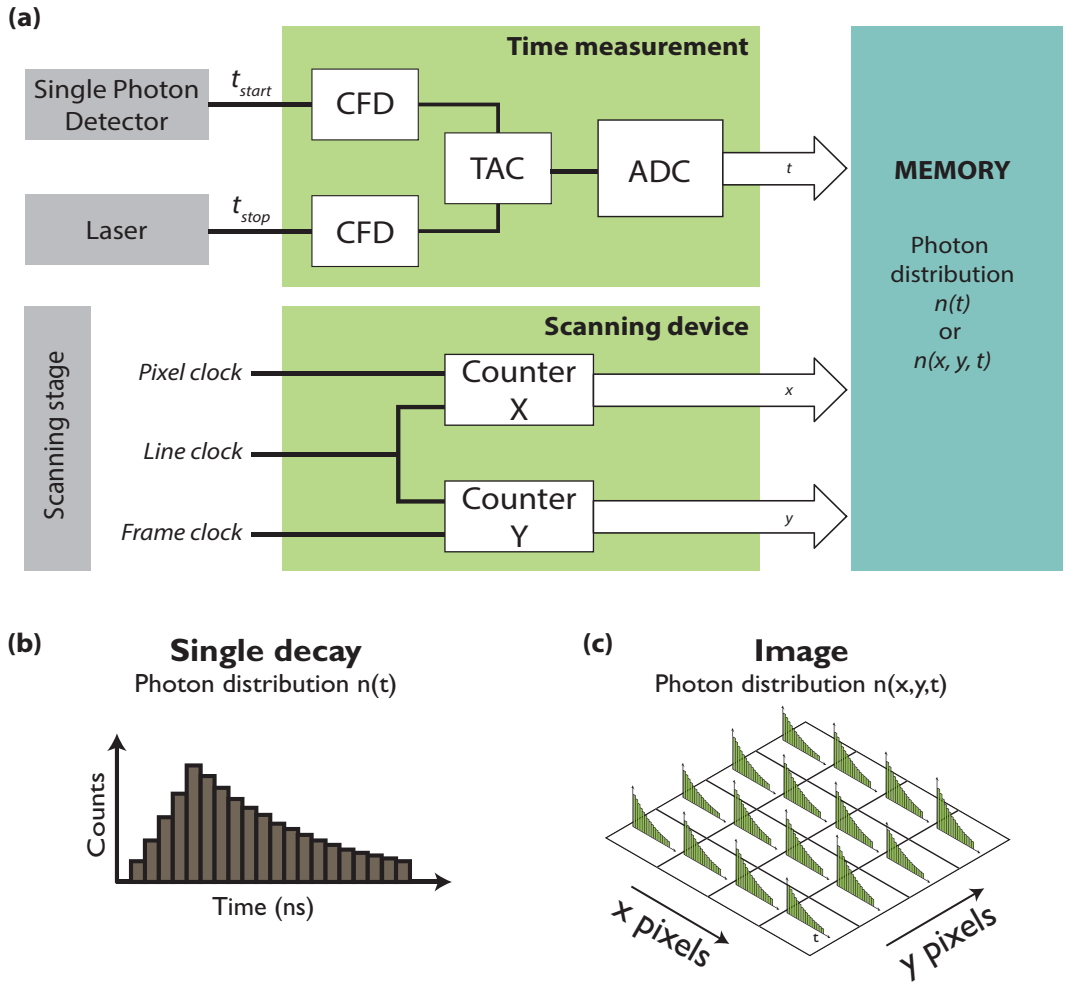

FIGURE 4.6: **Principle of TCSPC FLIM electronics (adapted from [194]).** (a) TCSPC electronics, (b) TCSPC data: Single measurement, (c) TCSPC data: FLIM.

4.3.2.2 Experimental setup

The TCSPC FLIM system used to carry out the following experiments is based on an inverted Nikon Eclipse TE 2000-E microscope. Figure 4.7 shows a diagram of the setup. A white-light pulsed laser source (Fianium Femtopower 1060) generates 400 fs pulses at a 20 MHz frequency. The beam is spatially filtered by focusing it onto a 10 μm pinhole, and then expanded and collimated before entering the microscope. A monochromator combined with an excitation filter and a dichroic mirror then allow the selection and direction of the excitation beam of a given wavelength through the microscpe objective focusing the light onto the sample. The fluorescence signal emitted by the molecules passes back through the objective and the dichroic mirror to finally reach the SPAD (ID 100-50, ID Quantique). Potential excitation light reflected by the sample is blocked by the dichroic mirror and the emission filter. Using another port of the microscope, spectroscopic measurements of the fluorescence signal can be performed (QE Pro, Ocean Optics). An additional excitation path similar to an upright microscope has been built for the case where transmission measurements are needed (see dashed green path in Figure 4.7).

Thanks to the modularity of the setup, a broad wavelength range including the visible and the near-infrared ranges of the electromagnetic spectrum (450 nm – 1700 nm) can be used. In exactly the same way shown in Figure 4.7 for visible excitation wavelengths (450 nm to 750 nm), the near-infrared laser beam is spatially and spectrally filtered using suitable optics. For clarity, only a single excitation path is shown in Figure 4.7. To overcome the issue of internal optics of the microscope being only optimised for transmission in the visible range of the spectrum, a specific removable path has been built for near-infrared wavelengths. This arm can be inserted between the dichroic filters wheel and the core of the microscope and uses optics suitable for the near-infrared range (see dashed orange path in Figure 4.7), ensuring maximum transmission in a region where emitters often have lower quantum yields. Two kinematic mirrors are used to direct the light towards a CCD camera in order to visualise the sample, a near-infrared SPAD (ID 220, ID Quantique) to perform time-resolved photoluminescence or a near-infrared spectrometer (NIR Quest, Ocean Optics) for spectroscopy.

A 3-axis piezo stage (LP200, Mad City Labs) generating the essential frame clock, line clock and pixel clock is used to scan the sample. In order to be able to build the distribution of

photons over time and location, these three TTL (Transistor-Transistor Logic) pulses are sent to the TCSPC module (SPC-150, Becker&Hickl) as well as a reference pulse from the laser and pulses from the SPAD detector. All the hardware components are controlled via LabVIEW and the SPCM Software from Becker&Hickl.

4.3.2.3 TCSPC data

The measurement of a fluorescence decay usually involves the recording of the intensity decay of the sample $D(t_i)$ and the instrument response function (IRF) $IRF(t_i)$, where i is the number of time channels used for the measurement. The IRF, representing the shortest time measurable by the instrument, can for instance be collected using reflected excitation light or a scattering solution of colloidal silica and no emission filter. However, if the detectors used have a strong wavelength dependent timing response, if might be more useful to collect an IRF at a wavelength closer to the emission wavelength of the sample. To do so, samples with very short lifetimes ($\approx 10\ ps$) and broadband emission such as LDS 798 dye [196], pinacyanol iodide [197] or Allura red [198] can be used. Another method is to quench dyes with nanosecond range lifetimes down to the picosecond range. This quenching can be achieved using collisional quenchers such as saturated potassium iodide [199] or sodium iodide solutions [200]. The shape of the IRF depends both on the type of single-photon detector and the timing electronics. The single-photon avalanche diode (SPAD) used in the TCSPC setup described above shows quite a narrow IRF of width 40 ps (Full Width at Half Maximum of the intensity).

The measured intensity decay of the fluorophore is represented by discrete values. Each point represents the number of photons that have been emitted in the corresponding time channel. The number of time channels used in experiments can be varied from 64 to 4096 regarding the complexity of the intensity decay.

4.3.3 Data analysis

The measured intensity decay $S(t)$ corresponds to a convolution of the IRF, $IRF(t)$, and the fluorescence from the sample, $D(t)$, expressed as:

$$S(t) = IRF(t) * D(t) = \int_0^t IRF(t')D(t-t')dt' \tag{4.3}$$

In order to analyse the intensity decay, the IRF has to be taken into account, especially if the lifetimes are expected to be of the order of magnitude of the IRF. In the case of long lifetimes, the intensity decay may be used without deconvolution of the IRF, as the effect of the IRF on the intensity decay is negligible. Several methods of TCSPC data analysis have been proposed such as nonlinear least squares [201–203], the method-of-moments [204] or methods based on Laplace [205, 206] or Fourier [207] formalisms. Each of these methods have advantages and drawbacks regarding the type of intensity decay that need to be analysed [208, 209]. For example, some of them require preliminary assumptions on the type of the intensity decay. Hence, in the case of complex intensity decays, it might be preferable to use methods that don't require such assumptions. Only methods that have been used in the following experiments will be described in details in the next subsections.

4.3.3.1 Nonlinear least squares

The nonlinear least squares method is one of the most widely used technique to analyse spontaneous emission decays. This method is based on the choice of a model to describe the experimental data, which is typically mono- or multi-exponential in the case of spontaneous emission decay. This method also requires the choice of initial values for the free parameters of the model (amplitudes A_j and decay constants τ_j of the j^{th} component). The aim is then, via an iterative process, to optimise the parameters values in order to get the best match between the experimental data and the calculated decay. This is done by minimizing the weighted sum of the squares of deviations of the calculated points, $Y(t)$, from the experimental ones $D(t)$ for all i time channels of the measurement. The goodness-of-fit parameter, called chi-squared, is given by equation 4.4:

$$\chi^2 = \sum_{i=1}^{n} w_i \left\| D(t_i) - Y(t_i) \right\|^2 \tag{4.4}$$

where w_i is the weight of each measurement point, which is usually estimated as the standard deviation $w_i = \frac{1}{\sigma_i}$ of the measurements.

In the case of TCSPC measurements, the probability of measuring n photons during a certain period of time is given by a Poisson distribution. For each time channel i, the standard deviation σ_i is then known to be the square root of the number of photon counts $\sigma_i = \sqrt{D(t_i)}$, assuming there is no other source of uncertainty in the data. Thus, if the model chosen corresponds well to the data, χ^2 should be close to the number of time channels. A reduced chi-squared χ^2_R value is typically defined as:

$$\chi^2_R = \frac{\chi^2}{i-p} = \frac{\chi^2}{\nu} \tag{4.5}$$

where ν is the number of degrees of freedom, i is the number of time channels and p the number of fitted parameters. χ^2_R is then expected to be close to unity for a suitable model. If the model used is not appropriate to describe the data, the deviations between model and experiment will be larger, leading to a value of χ^2_R greater than 1. Very small values of χ^2_R may indicate an error in the determination of the uncertainties in the measurements.

Several algorithm are available to iteratively perform the least-squares estimation of nonlinear parameters [210]. The most commonly used algorithm for fitting of exponential decays is the Levenberg-Marquardt algorithm [211, 212], showing robust and rapid convergence properties [213]. In order to take into account the IRF of the system, the model $Y(t)$ is first of all convoluted to the instrumental response $IRF(t)$ and then iteratively compared to the experimental data $S(t_i)$. The implementation of this method will not be discussed but more details can be found in [211, 214].

4.3.3.2 Inverse Laplace transform

In most of the experimental studies performed in the next chapters, another analysis method based on the inverse Laplace transform approach has been mainly used. As opposed to a method based on a predefined model, resulting in the fitting of the spontaneous emission data with a discrete set of exponentials, the inverse Laplace transform method is used to interpret the spontaneous emission data in terms of a continuous distribution of lifetimes. Due to the nature of the spontaneous emission processes occurring for emitters placed in the electromagnetic environments considered, such as metallic films or metamaterials, which are strongly dependent on the distance and orientation of the emitters with regard

to the structures, the distribution-like description of the spontaneous emission is more appropriate. This type of method does not rely on any preliminary assumption on the emission process and hence does not require the choice of a specific model to fit the time-resolved photoluminescence decays [205, 215]. This procedure consists in solving the integral equation

$$D(t) = \int_0^\infty F(\tau) e^{-\frac{t}{\tau}} d\tau \tag{4.6}$$

where $D(t)$ is the time dependent fluorescence decay, deconvoluted from the instrumental response function and $F(\tau)$ is the weighted fluorescence lifetime distribution.

An analytical method developed by Provencher [215] was implemented to fit the spontaneous emission decays presented in the next chapters. As inverse problems, such as inverse Laplace transforms, are known to be ill-defined, an iterative fitting procedure based on a regularised inverse Laplace transform was used in order to achieve stable results. This procedure consists in minimising the following equation

$$\sum_{i=1}^{n} w_i \left\| D(t_i) - Y_{i,fit} \right\|^2 + \alpha^2 \sum_{j=1}^{N_{reg}} \left\| r - Rg \right\|_j^2 \tag{4.7}$$

where the first term represents the weighted sum of the squares of deviations of the fit $Y_{i,fit}$ from the experimental decay $D(t)$ for each time channel of the measurement and the second term is the regularisor. The fitting function $Y_{i,fit} = Ag$ is based on an inverse Laplace transform where $A = e^{-t_i/\tau}$, with τ a vector containing the time range probed for the lifetime distribution, and g is the relative amplitude of the components of the lifetime distribution. The regularisor term, composed of two arrays r ($N_{reg} \times 1$) and R ($N_{reg} \times n$), is typically chosen in order to eliminate solutions deviating from expected behaviours and its importance is set by the constant α. The regularisor implemented to fit the experimental data presented in the scope of this thesis was based on the principle of parsimony, consisting in favouring smooth solutions with the minimum number of peaks [215] by defining the regularisor $r - Rg$ as the second derivative of g. In order to reduce the number of available solutions to fit the data, constraints such as $g > 0$ can be applied on the lifetime distribution function.

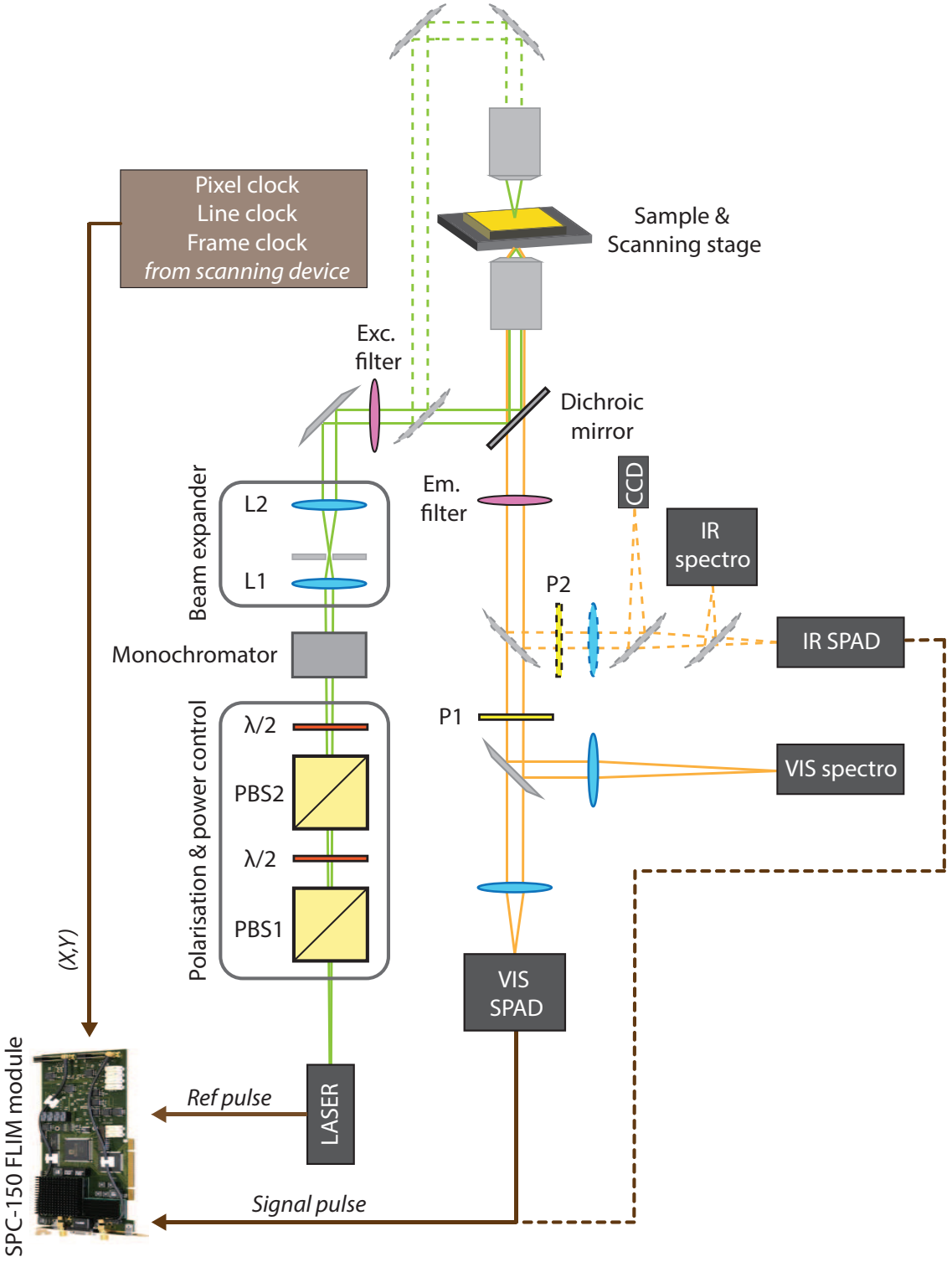

FIGURE 4.7: **TCSPC FLIM setup.**

Chapter 5

Spontaneous emission in nonlocal materials

When the behaviour of a physical system at a given point depends on its state at another spatially separated region, the system is described as being non-local. This non-locality is shown to be present in engineered composites, metamaterials, where coherent surface plasmons mediate the coupling between the unit cells of artificial electromagnetic crystals.

In this chapter, the process of spontaneous emission in a non-local environment is analysed both experimentally and theoretically using a plasmonic nanorod metamaterial platform. This platform has been recently demonstrated to enable a topological transition between elliptic and hyperbolic dispersions. Experimentally, a broadband, macroscopically averaged lifetime reduction of the order of 30 was demonstrated, while microscopic reductions in lifetime are orders of magnitude higher. New theoretical and numerical approaches capable of calculating the local density of photonic states in non-local media were also developed. Although non-local effects have a weak impact on linear reflection and transmission through the metamaterial [104], they are essentially dominating the dynamics of emitters' decay, and other quantum optical processes, inside a nanorod metamaterial, where the density of photonic states is fundamentally altered by the presence of an additional propagating mode inside the metamaterial [169].

5.1 Samples

5.1.1 Emitters

For this study, four organic dye molecules (fluorescein (D1), Alexa 514 (D2), ATTO 550 (D3) and ATTO 647N (D4)) with their peak emission wavelengths respectively around 514 nm, 550 nm, 575 nm and 670 nm, were used to probe local density of states of the metamaterial. Solutions containing dyes D1 and D2 were prepared with ethanol (refractive index 1.36) at a dye concentration of 2.5×10^{-5} $mol.L^{-1}$. In the case of D3 and D4, the dye molecules were dissolved at a concentration of 10^{-6} $mol.L^{-1}$ in a water based solvent (refractive index 1.33). The dye solutions were then introduced in the metamaterial using a flow cell, which was positioned on a confocal microscope for fluorescence measurements.

5.1.2 Metamaterial parameters

The nanorod metamaterial was fabricated by gold electrodeposition into highly ordered nanoporous AAO on a glass coverslip, according to the two-step anodisation procedure described in Chapter 4. The AAO matrix was subsequently dissolved in order to achieve free standing nanorods. The nanorod parameters used in the reported experiments were 50 ± 2 nm in diameter, of 100 nm period and 250 ± 5 nm height.

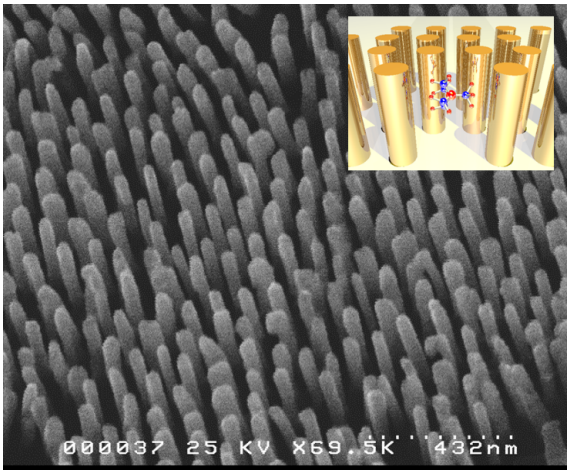

FIGURE 5.1: **SEM image of the metamaterial.** Gold nanorod-based metamaterial. Inset: schematic of the metamaterial with a fluorescent molecule inside it.

Figure 5.1 shows an SEM image of the sample used. In order to ensure a correct comparison between the measurements for different emitters, the same metamaterial sample was used

for all four dyes. Therefore, after each measurement, the dye solution was washed out and the sample cleaned by oxygen plasma treatment.

In order to further characterise the sample, extinction spectra of the metamaterial for various illumination angles were measured for different dielectric hosts (Figure 5.2). For free standing gold nanorods, i.e in air (Figure 5.2b), the typical mode structure of this type of metamaterial is observed. In this case, both transverse and longitudinal modes are overlapping due to the low refractive index between the nanorods. The same spectra were then taken by immersing the sample in ethanol (Figure 5.2b) or water (Figure 5.2c), in which the molecules were dispersed. By increasing the refractive index of the dielectric host embedding the nanorods, a red-shift of the longitudinal mode can be observed (from about 540 nm in (a) to 581 nm in (b) and 584 nm in (c)).

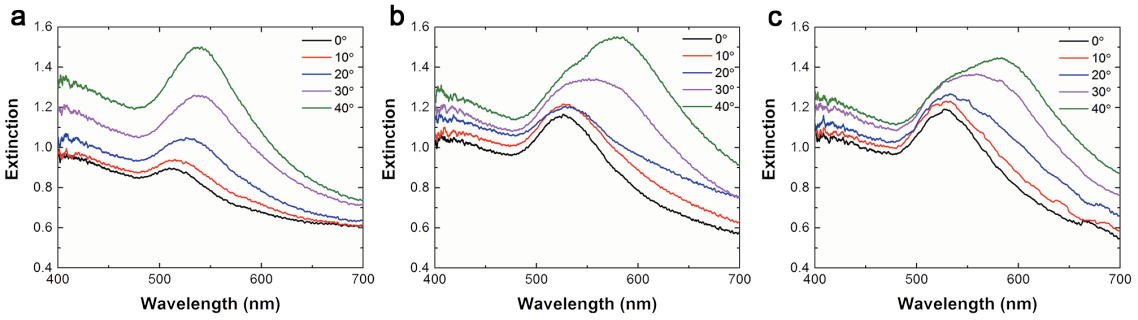

FIGURE 5.2: **Experimental extinction spectra of the gold nanorods in different dielectric hosts.** Experimental extinction spectra ($-log(Transmission)$) of the metamaterial consisting of free standing nanorods for different angles of incidence of TM-polarised light in (a) air, (b) ethanol and (c) water.

5.2 Electromagnetic waves in the metamaterial and topology of isofrequency surfaces

For wavelengths of light much larger than all the characteristic sizes of the composite, such as the diameter and separation of the nanorods, the optical properties of the metamaterial can be described with an effective permittivity, which can be used to calculate transmission, reflection and absorption spectra of the composite. As mentioned in Chapter 2, the optical properties of a nanorod metamaterial resemble those of an homogeneous uniaxial anisotropic medium with its optical axis parallel to the nanorods (z-direction). Homogeneous anisotropic media support the propagation of two types of waves that

differ by their polarisation. While ordinary waves (TE modes), with the electric field normal to the metamaterial's optical axis ($\mathbf{E} \perp z$), do not experience an anisotropy of dielectric permittivity, extraordinary waves that have their magnetic field normal to the metamaterial's optical axis ($\mathbf{H} \perp z$) are strongly affected by the material anisotropy.

A local EMT using the Maxwell-Garnett approximation described in Chapter 2 section 2.3.4.3 was employed to determine the effective dielectric permittivity of the metamaterial. The permittivity of electrochemically deposited gold was described using the Drude model with corrections for the restricted mean free path of electrons [216], which has previously been shown to be in quantitative agreement with experimental results [104, 216]. As represented in Figure 5.3, the sign of the real part of the component of the effective dielectric permittivity along the nanorods ε_{zz}^{loc} changes from positive to negative at a wavelength of about 575 nm. Therefore, the composite operates in the elliptic dispersion regime for wavelengths below 575 nm and in the hyperbolic dispersion regime for longer wavelengths ($\epsilon_{xx} = \epsilon_{yy} > 0$ *and* $\epsilon_{zz} < 0$). The region around 575 nm, corresponding to the ENZ region ($\varepsilon_{zz}^{loc} \approx 0$), is representative of the effective plasma frequency of the metamaterial [217]. Figure 5.3 also depicts the peak emission wavelengths of the four dyes used in the following experiments, spanning the elliptic, ENZ and hyperbolic dispersion regimes.

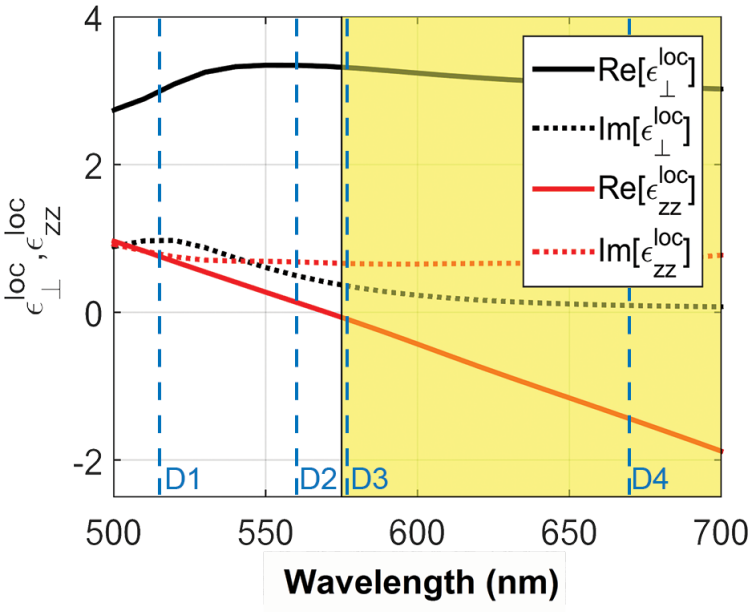

FIGURE 5.3: **Local effective medium parameters of the metamaterial (Au nanorods in ethanol).** Vertical dashed lines indicate the emission wavelengths of the dyes used for the PL lifetime measurements.

According to the dispersion relation for such material described by Equation 2.26b in Chapter 2 the isofrequency surfaces of the metamaterial at different wavelengths were calculated. The geometrical properties of these isofrequency surfaces are often referred to as the optical topology of the metamaterial [163]. For the composite used in this work, the optical topology exhibits typical ellipsoidal isofrequency surfaces for TE modes in both elliptic and hyperbolic dispersion regimes as depicted in Figure 5.4(a, b). The dispersion of TM modes in the hyperbolic regime is described by a hyperboloid (Figure 5.4d), while in the elliptic regime, it is represented by an ellipsoid in the center of the Brillouin zone, which is increasingly deformed for higher wavevectors (Figure 5.4c).

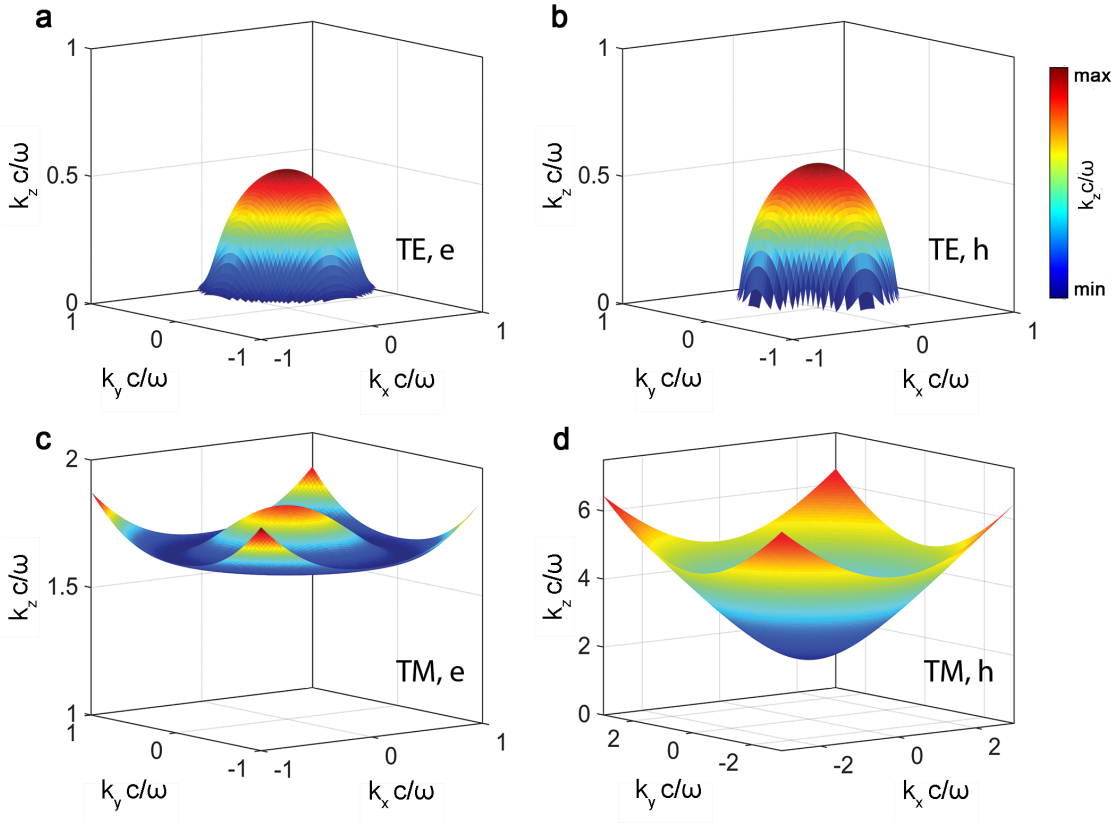

FIGURE 5.4: **Isofrequency surfaces describing the dispersion of the propagating modes in the metamaterial with parameters as in Figure 5.2b calculated with the local EMT. (a,c)** elliptic (denoted e) regime ($\lambda = 550\ nm$), **(b,d)** hyperbolic (denoted h) regime, ($\lambda = 650\ nm$) for **(a,b)** TE- and **(c,d)** TM-polarized modes. The colormap represents the magnitude of $k_z c/\omega$.

The optical topology of a metamaterial is known to have a significant effect on its quantum optical properties, theoretically leading to a singularity in the local density of optical states in homogeneous hyperbolic media [89], which in turn can strongly affect the rate of spontaneous emission [88] or other processes such as nonradiative energy transfer between

molecules [183]. Recent experimental studies, mostly focused on emitters near a layered metamaterial designs, have demonstrated relatively modest 5 to 10-fold enhancements of the decay rate in the hyperbolic dispersion regime and smaller enhancements in the elliptic dispersion regime [163]. Similar results were reported for emitters on top of hyperbolic plasmonic nanorod metamaterials [167]. However, the geometry of the system used in previous studies prevented a characterisation of the emission dynamics in the non-local metamaterial regime, most pronounced inside nanorod metamaterials operating in the elliptical dispersion regime [104, 105, 218, 219].

5.3 Consequences of optical non-localities

In the wavelength range in which the nanorod metamaterial supports the propagation of an additional TM-polarised mode as described in 2.3.4.4, the topology of the metamaterial can be calculated using the dispersion relation of TM-polarised waves for non-local media described by Equation 2.28. Comparing Figure 5.4 and Figure 5.5, it is seen that while the differences are minimal in the hyperbolic regime of dispersion, the behaviour in the elliptic dispersion regime is drastically different. The isofrequency of one of the TM-polarised waves qualitatively agrees with an ellipsoid, predicted by the local dispersion relation (Equation 2.26b) and the second TM-polarised mode, which is absent in the local effective medium theory, has a hyperbolic-like topology (Figure 5.5c).

The differences between the local and non-local EMTs were also investigated by looking at the extinction properties of the metamaterial slab for the metamaterial parameters used in this work. The calculated spectra from both methods are almost identical with small deviations at the larger angles of incidence (Figure 5.6), with the non-local EMT providing better correspondence to the shape of the experimentally measured spectra (Figure 5.2(a,b)).

While non-locality is shown to have only a weak effect on the transmission properties of the metamaterial, a large disagreement between the predictions of the two approaches exists for the evaluation of the emission properties of dipoles embedded inside this type of metamaterial. From the point of view of an emitter, the presence of an additional electromagnetic wave represents a separate emission decay channel that drastically increases the LDOS in the elliptic regime and affect the radiation dynamics.

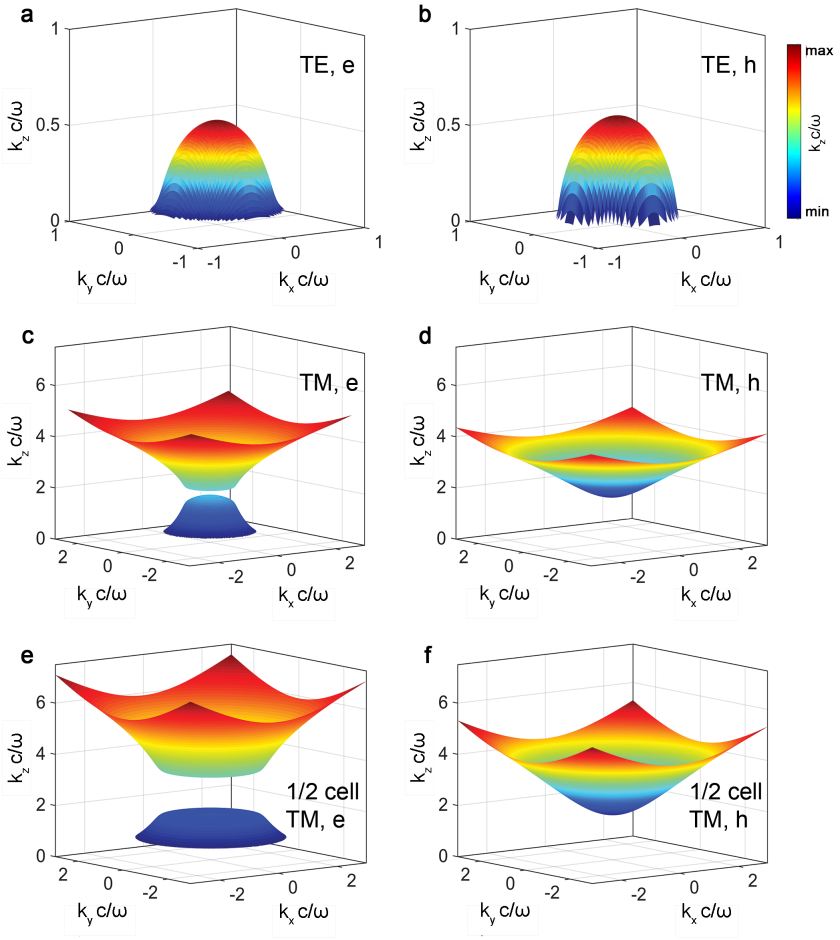

FIGURE 5.5: **Dispersion of the modes supported by the nanorod metamaterial calculated using the non-local effective medium theory. (a,c,e)** elliptic (denoted e) regime ($\lambda = 550\ nm$) and **(b,d,f)** hyperbolic (denoted h) regime ($\lambda = 650\ nm$) in the case of **(a,b)** TE- and **(c-f)** TM-polarized modes for **(a-d)** the metamaterial considered in experiments (as in as in Figure 5.2b) and **(e,f)** metamaterial with 50% unit cell and nanorod diameter (25 nm diameter, 50 nm period). The scaling does not change the local effective medium parameters of the composite (Figure 5.4). The colormap represents the magnitude of $k_z c/\omega$.

5.4 Engineering non-local response by scaling metamaterial's unit cell and losses

The dispersion of modes in plasmonic nanorod composites can be controlled by scaling the unit cell, a process that does not change the local effective medium response. The predicted changes in the dispersion of optical modes as a result of geometry scaling are summarised in Figure 5.5(e, f). Material losses can be controlled by the choice of plasmonic metal or by fabrication (for example, annealing) and serve as an additional degree of freedom for engineering the optical properties of a metamaterial. The dispersion of the modes

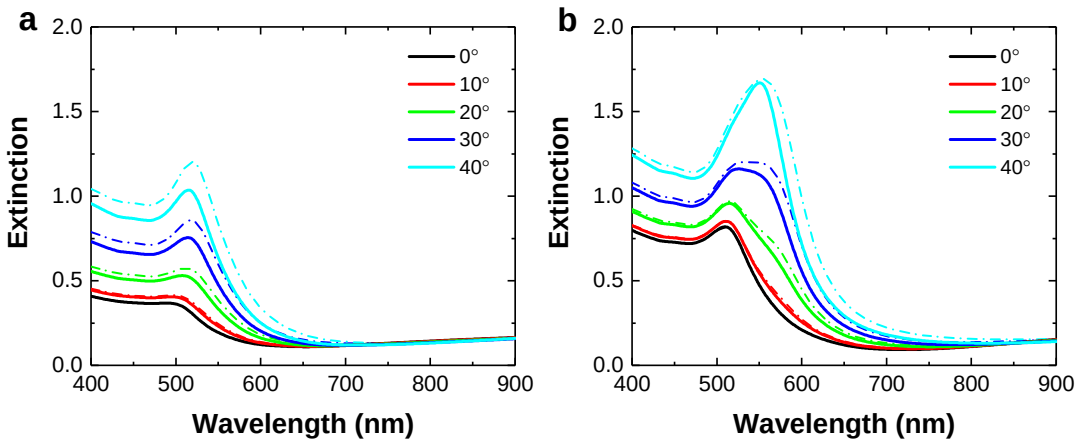

FIGURE 5.6: **Calculated extinction spectra of the nanorod metamaterial for different angles of incidence** in **(a)** air and **(b)** ethanol using (dashed lines) local and (solid lines) non-local EMT.

supported by the nanorod composite, predicted by local and non-local EMT clearly shows that the dispersion of TE-polarised modes does not significantly depend on materials absorption or unit cell size and is close to those presented in Figure 5.4(a, b). On the other hand, when the metamaterial operates in the elliptic regime, absorption, along with unit cell configuration, play an important role in defining the topology of TM-polarised modes (Figure 5.7). When the losses are small, the two TM-polarised modes represent well-separated branches in the wavevector space, with the lower branch having elliptical behaviour and the upper branch exhibiting hyperbolic-like topologies (Figure 5.7(a, d)). As the unit cell becomes smaller (Figure 5.7(d-f)), the behaviour of the elliptic branch approaches the predictions of the local effective medium theory (Figure 5.7g), while the upper branch moves "up", increasing the effective index of the mode. As losses increase, the two TM-polarised modes approach each other (Figure 5.7(b, c)). Scaling the size of the unit cell of the metamaterial still drastically affects the topology of these waves (Figure 5.7(e, f)). Note that when losses are high, the local EMT converges to the upper (hyperbolic) wave (Figure 5.7i). However, in the regime of moderate losses, realised in this work, the local EMT becomes invalid, predicting the response that does not match the properties of either of the two modes of the metamaterial (Figure 5.7h). When the metamaterial operates in the hyperbolic regime, the elliptical branch of the TM dispersion cuts off, and the propagation of light is dominated by the hyperbolic branch (Figure 5.8). The effect of the spatial dispersion is now essentially limited to a quantitative correction

of the dispersion.

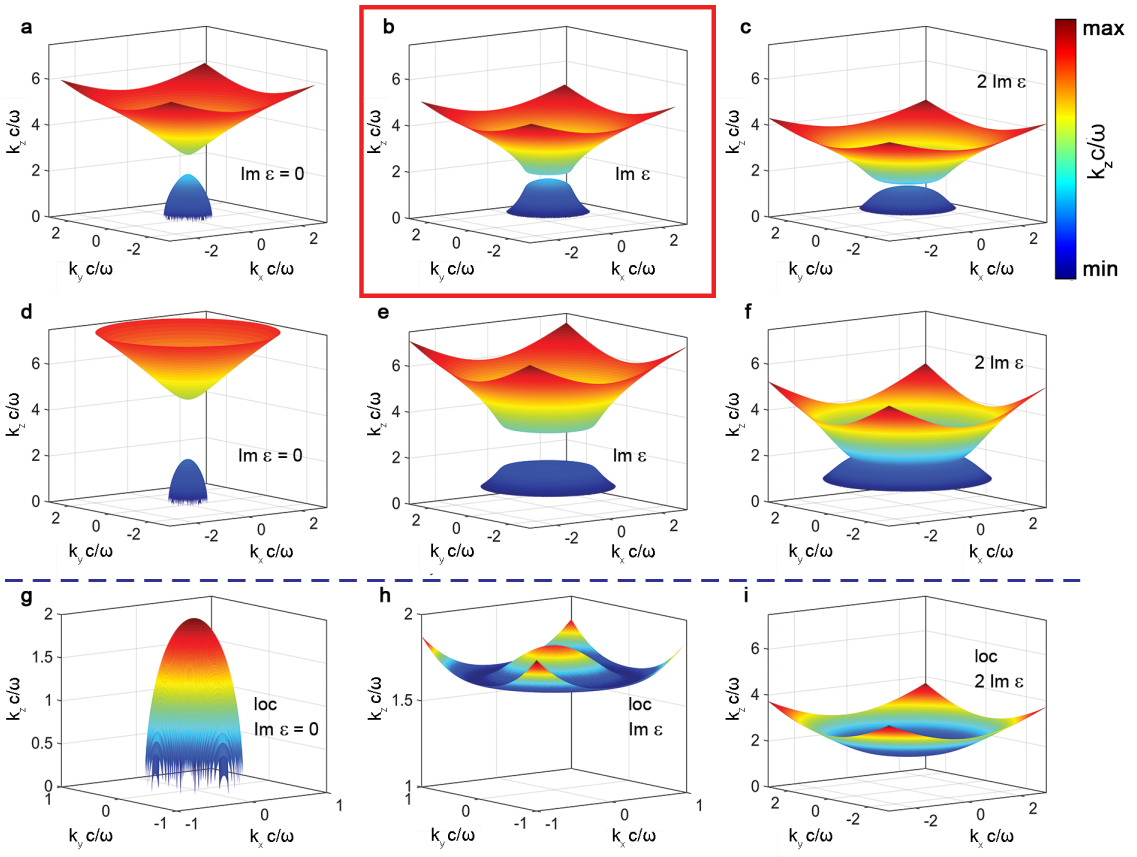

FIGURE 5.7: **Dispersion of TM-polarised modes supported by nanorod composites in the elliptical regime ($\lambda = 550\ nm$) for different material absorption and geometry. (a, d, g)** hypothetical loss-less metamaterial, **(b, e, h)** absorption as in the experiment, **(c, f, i)** twice larger absorption than in (b, e, h); **(a-f)** non-local effective medium theory for metamaterials with (a-c) $a = 100\ nm$, $r = 25\ nm$ as in the experiment and (d-f) 50% unit cell ($a = 50\ nm$, $r = 12.5\ nm$), **(g-i)** local effective medium theory; the solid box (b) highlights the dispersion of the modes in the metamaterial used in the experiment; the dashed line separates predictions of non-local and local EMTs from each other. The colormap represents the magnitude of $k_z c/\omega$.

5.5 Photoluminescence and time-resolved analysis

In order to experimentally study the effect of non-locality on the emission properties of emitters, time-resolved photoluminescence was performed using the experimental setup described in section 4.3.2.2 of Chapter 4. The excitation wavelength for each dye was chosen according to its absorption spectrum: 470 nm for fluorescein (D1) and Alexa 514 (D2), 525 nm for ATTO 550 (D3) and 633 nm for ATTO 647N (D4). The excitation light was focused onto the sample using a 100× oil immersion objective with a numerical

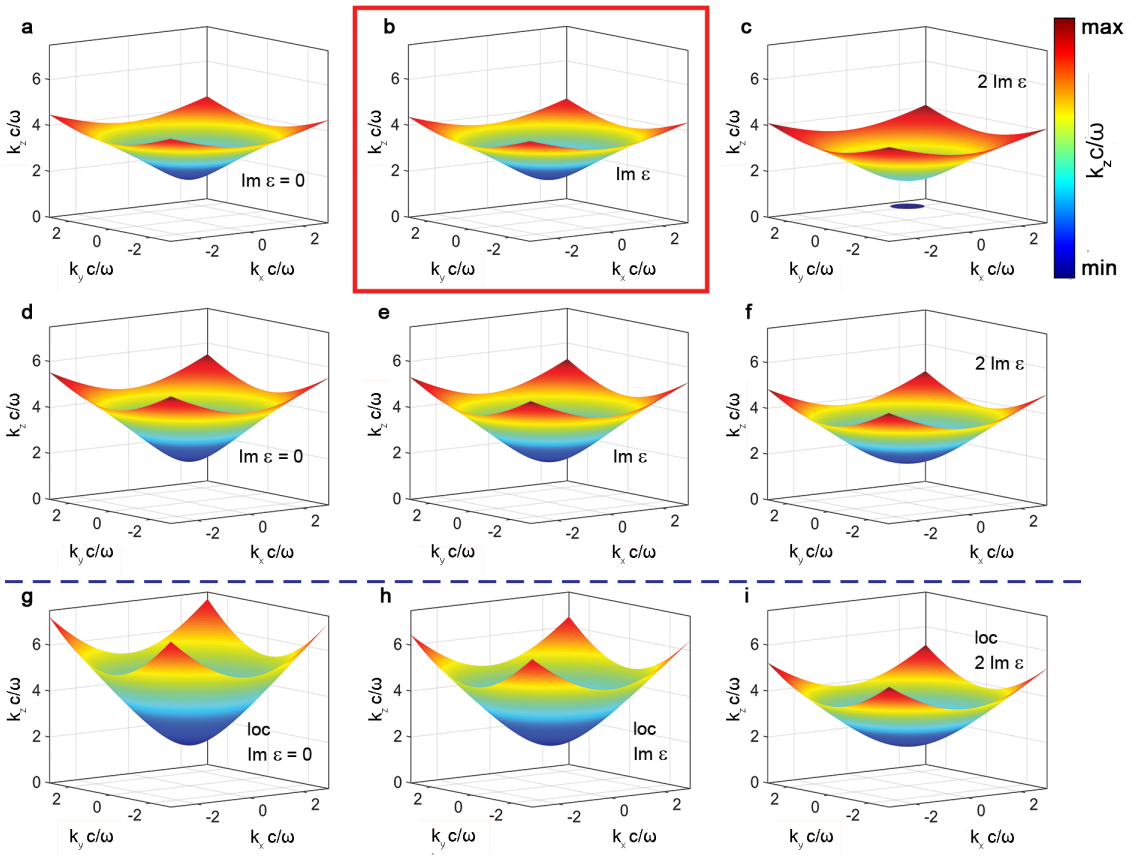

FIGURE 5.8: **Dispersion of TM-polarised modes supported by nanorod composites in the hyperbolic regime ($\lambda = 650\ nm$) for different material absorption and geometry. (a, d, g)** hypothetical loss-less metamaterial, **(b, e, h)** absorption as in the experiment, **(c, f, i)** twice larger absorption than in (b, e, h); **(a-f)** non-local effective medium theory for metamaterials with (a-c) $a = 100\ nm$, $r = 25\ nm$ as in the experiment and (d-f) 50% unit cell ($a = 50\ nm$, $r = 12.5\ nm$), **(g-i)** local effective medium theory; the solid box (b) highlights the dispersion of the modes in the metamaterial used in the experiment; the dashed line separates predictions of non-local and local EMTs from each other. The colormap represents the magnitude of $k_z c/\omega$.

aperture of 1.49 and the resulting photoluminescence signal collected by the same objective. Appropriate band-pass filters centered on the peak emission wavelength of each dye were used to collect the photoluminescence signal and prevent any laser contribution to the measured light. For each dye, a set of three measurements have been taken: inside the metamaterial, on a thin (50 nm) gold film and on a glass substrate for reference. The photoluminescence spectra of the different dyes on glass and inside the metamaterial are shown in Figure 5.9.

The decay dynamics of the four fluorescent dyes with different emission wavelengths spanning elliptic and hyperbolic regimes of dispersion is summarised in Figure 5.10. Although all the studied emitters show nearly single-exponential fluorescence decay in a

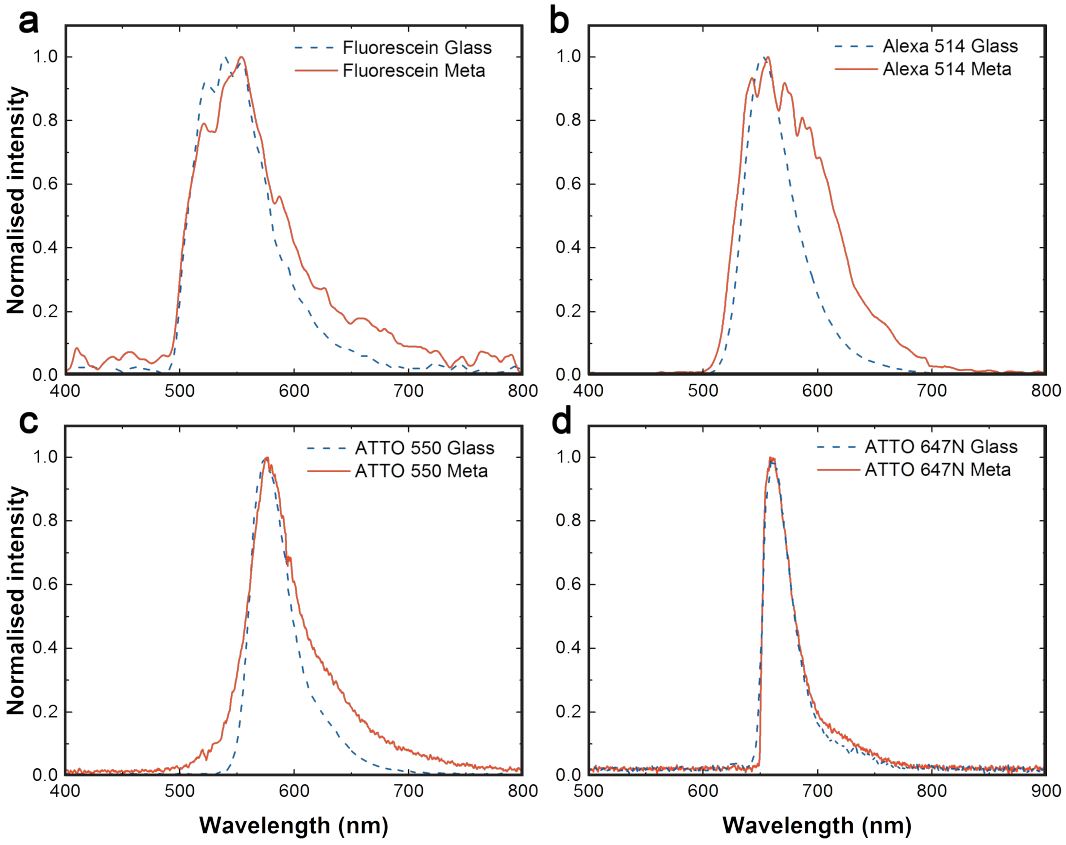

FIGURE 5.9: **Emission spectra of the emitters (blue) on a glass surface and (red) inside the metamaterial. (a)** fluorescein (D1), **(b)** Alexa 514 (D2), **(c)** ATTO 550 (D3) and **(d)** ATTO 647N (D4).

homogeneous environment, the presence of plasmonic surfaces and nanostructures makes the dynamics multi-exponential. This effect is the direct result of an ensemble of emitters contributing to the signal, with each individual emitter having its own position- and polarisation dependent decay rate in the structured environment.

To analyse the dynamics of the emitters, the inverse Laplace transform method presented in Chapter 4 was used, leading to the distributions of lifetimes represented in Figure 5.11. Emitters located above a glass substrate show smooth localised lifetime distributions peaked around their standard values of a few nanoseconds. The comparison of the decays for glass and gold interfaces reveals the expected behaviour, caused by the presence of the metal and related plasmonic excitations [220]. The overall peak to peak rate enhancement obtained is less than 2. For example, the lifetime distribution for D1 emitters (Figure 5.10) is peaked at 3.9 ns, representing the reduction of the macroscopically averaged lifetime by a factor of ≈ 1.2. The dynamics measured for the emitters inside the metamaterial exhibit

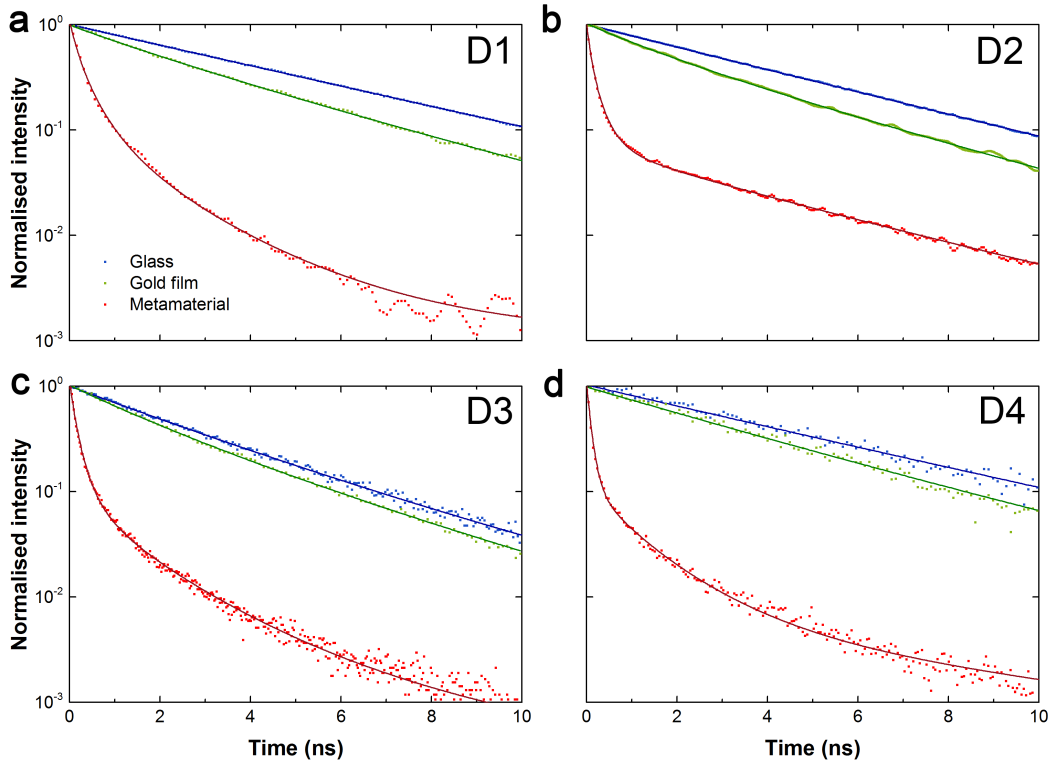

FIGURE 5.10: **Fluorescence dynamics of the emitters (blue) on a glass surface, (green) on an Au film, (red) inside the metamaterial.** The studied emitters are **(a)** fluorescein (D1), **(b)** Alexa 514 (D2), **(c)** ATTO 550 (D3) and **(d)** ATTO 647N (D4). Dotted and solid lines respectively represent experimental results and dynamics recovered by applying an inverse Laplace transform to the experimental data.

even faster decays with even broader distributions (7–100 times) of lifetimes than for a single metal interface (Figure 5.11). The span of the lifetime distributions reflects a strong position-dependent decay rate enhancement for the emitters inside the nanorod array unit cell [221]. A substantial lifetime reduction was observed for all wavelengths.

The inverse Laplace transform approach was then verified by recovering the spontaneous emission lifetime distribution near a smooth gold film from the distribution obtained for the emitters on glass.

5.5.1 Theoretical lifetime analysis of the ensemble of emitters near a gold film

The spontaneous emission of an emitter near a metallic surface can be theoretically studied by considering a randomly oriented oscillating point dipole at a distance d above the

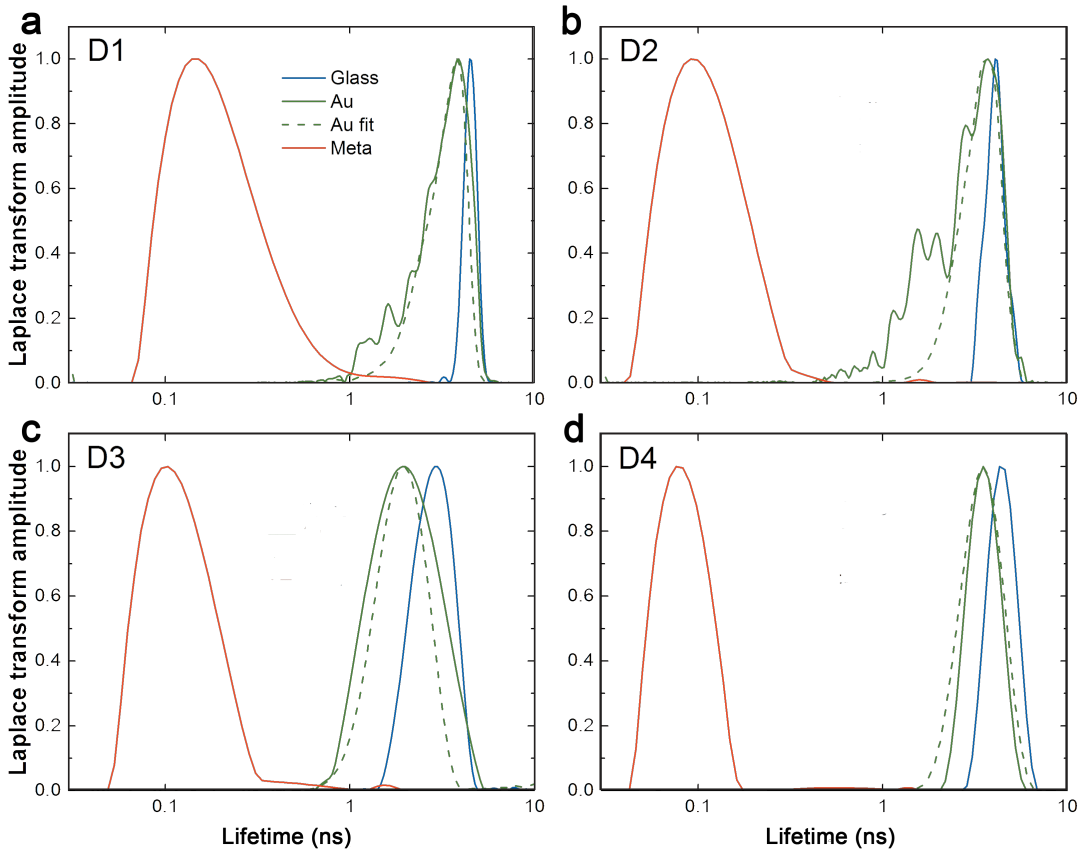

FIGURE 5.11: **Experimental fluorescence lifetime distribution of the emitters in different environments.** The distributions are extracted from the PL measurements using a Laplace transform method: (blue) on glass substrate, (green) on Au film and (red) inside the metamaterial. Dashed green lines represent the lifetime distributions above the smooth gold surface recalculated from the measured lifetime distributions in the dielectric environment shown with blue lines. **(a)** D1: Fluorescein. **(b)** D2: Alexa 514. **(c)** D3: ATTO 550. **(d)** D4: ATTO 647N.

metallic surface. In order to evaluate the modification of the decay rate of the emitter with regard to its distance from the metallic film, an method developed by Ford and Weber in [111] has been implemented. In this approach, the dipolar field is written as the superposition of TM- and TE-polarised plane waves and the influence of the metallic interface was explained by its plane wave reflection coefficients. The power dissipated by the dipole above the metal surface can then be approximated as a sum of the different power dissipation channels for an emitter near a metallic interface, yielding

$$\mathcal{P} = \mathcal{P}_{PH} + \mathcal{P}_{SP} + \mathcal{P}_{LSW} \tag{5.1}$$

where $\mathcal{P}_{PH}$ is the power radiated via photons, $\mathcal{P}_{SP}$ via surface plasmons and $\mathcal{P}_{LSW}$ that via lossy surface waves as described in Chapter 3 section 3.2.1 [111].

Taking into account the known power radiated by a dipole far from the metal surface $\mathcal{P}_{inf}$ (distance between the emitter and the metallic interface $z \rightarrow \infty$) as well as the quantum yield η intrinsic to the emitter and the medium in which they are embedded, both the local quantum yield of the emitter $Q_{loc}(z)$ and the total decay rate enhancement factor $\Psi(z)$, as a function of the distance between the emitter and the metallic interface, can be calculated for both parallel and perpendicular components of the dipole, leading to

$$\Psi(z) = \eta \frac{\mathcal{P}_{PH}(z) + \mathcal{P}_{SP}(z) + \mathcal{P}_{LSW}(z)}{\mathcal{P}_{inf}} + (1 - \eta) \tag{5.2a}$$

$$Q_{loc}(z) = \frac{\mathcal{P}_{PH}(z)/\mathcal{P}_{inf}}{(\mathcal{P}_{PH}(z) + \mathcal{P}_{SP}(z) + \mathcal{P}_{LSW}(z))/\mathcal{P}_{inf} + (1 - \eta)/\eta} \tag{5.2b}$$

In order to take into account the random orientation of the emitters above the metallic surface, $\Psi(z)$ and $Q_{loc}(z)$ were calculated separately for dipoles aligned with each coordinate axis, and the overall values were calculated as the average $M(z) = \frac{1}{3}M_x(z) + \frac{1}{3}M_y(z) + \frac{1}{3}M_z(z)$ where $M = \Psi(z),\ Q_{loc}(z)$.

Given the experimental lifetime distribution of emitters near a glass substrate $F^{exp}_{Glass}(\tau)$, the corresponding distribution near a gold film can be calculated using the following expression

$$F^{theor}_{Au}(\tau) \approx \int_{d_{min}}^{d_{max}} |\mathbf{E}_{pump}(z)|^2 \, Q_{loc}(z) n(z) F^{exp}_{Glass}(\frac{\tau}{\Psi(z)}) dz \tag{5.3}$$

where $\Psi(z)$ is the position dependent polarisation-averaged decay rate enhancement factor near the gold surface, $|\mathbf{E}_{pump}(z)|^2$ is the position dependent intensity of the excitation light, $Q_{loc}(z)$ is the emitter local quantum yield and $n(z)$ is the density distribution of emitters along the depth of focus, which was assumed to be uniform. The depth of focus $(d_{max} - d_{min})$ was taken equal to $\approx 175\ nm$ for the best fit to the experimental data and an almost perfect agreement between theoretical predictions and experimental measurements

of the lifetime distributions was observed (Figure 5.11). Slight deviations between the fitting and the experimental data may arise due to the sensitivity of the inverse Laplace transform to the noise in the experimental data and the assumption on $n(z)$, which in principle, may encapsulate inhomogeneities in the solution.

5.5.2 Fluorescence decay rate calculations from EMT formulations

The experimental results of emission inside the metamaterial were then compared to calculations of the emission decay rates based on both local and non-local EMT, implemented by one collaborators. To do so, a Green's function formalism was used to analyse the emission rate modification [33]. In this approach, the emission rate is proportional to the imaginary part of the Green's function, representing the electric field $\mathbf{E}$ generated by the point dipole $\mathbf{d}$ at the location of the dipole [33, 169, 220]

$$\frac{\Gamma}{\Gamma_0} = \frac{3c^3}{2\omega^3} \frac{\mathrm{Im}(\mathbf{E} \cdot \mathbf{d})}{|W_0|^2} \tag{5.4}$$

where Γ_0 is the emission rate in free space, while Γ is the rate modified by the surrounding environment and W_0 is the power radiated by the dipole in free space and used as a normalisation constant. Out-of-plane (z-direction) and in-plane polarised dipoles were considered separately and the total emission rate was calculated as the weighted-average of the two dipole directions. This assumption is related to a completely random distribution of dye molecules inside the solution. The transfer matrix formalism was then used to take into account the effect of multiple reflections of the dipole's emission inside the composite layer [222]. In the non-local case, two TM-polarised modes were considered as independent emission channels. However, the obtained results suggest that the hyperbolic-like mode dominates the emission in both elliptic and hyperbolic regimes, similar to what has been previously reported in emission inside infinite idealised metamaterial [223].

According to Figure 5.12a, the local EMT predicts a strong enhancement of the decay rate in the ENZ regime, in sharp contrast with the experimentally observed behaviour. At the same time, the experimental data are in closer agreement with the predicted wavelength dependence of the decay rate given by the non-local EMT. The remaining quantitative difference between the predictions of the non-local EMT that averages the response of the

composite and the experimental data stems from the strong dependence of the LDOS on the position of the dipole within the unit cell. It is important to note that neither the local nor non-local EMT calculations allow the discrimination of the emitter's position in the unit cell of the array. Therefore, both methods provide an estimate of the average lifetime.

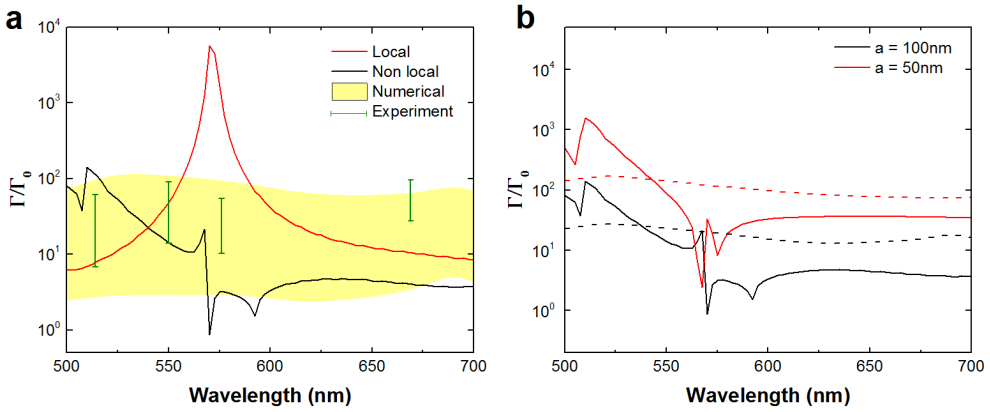

FIGURE 5.12: **Spectral dependence of the spontaneous emission lifetime modification. (a)** Spectral dependence of the lifetime averaged over the dipole orientation: (red) local theory, (black) non-local theory, (bars) experimental data corresponding to the width of the lifetime distribution at 10% of the modal amplitude (Figure 5.11), (shaded area) the width of the simulated lifetime distribution at 10% of the modal amplitude obtained applying the inverse Laplace transform to the decay curves after the averaging over the dipole position within the elementary cell of the metamaterial (Supplementary Figure S3a). **(b)** Spectral dependence of the enhancement rate obtained with the non-local theory (solid lines) and the full-wave numerical modelling at one position within the metamaterial (dashed lines, position 3 in Supplementary Figure S3a): (black) the metamaterial as in (a) used in the experiments ($d = 50\ nm$, $a = 100\ nm$) and (red) the metamaterial with 50% unit cell ($d = 25\ nm$, $a = 50\ nm$) that yields an identical local effective medium response.

5.5.3 Fluorescence decay rate calculations from numerical modelling

Numerical modelling was also performed using a pre-built model implemented in Comsol Multiphysics software (Finite Element Method (FEM)). The enhancement of the decay rate at various locations inside the nanorod metamaterial was calculated as a ratio of power flow from a point dipole placed at a given position and the corresponding value for a dipole in vacuum. In order to cross-check reliability of the numerical results, two methods were used for the power flow estimation: 1) via a Poynting vector flux through a small sphere (5 nm radius) enclosing the point dipole and 2) via the energy dissipation rate of the dipole, $W(\mathbf{r}) = -\frac{1}{2}\,\mathrm{Re}\,[\mathbf{J}^*(\mathbf{r}) \cdot \mathbf{E}(\mathbf{r})]$, where $\mathbf{E}(\mathbf{r})$ is the electric field produced by the dipole at the point of its location and $\mathbf{J}(\mathbf{r})$ is the dipole current. Both methods,

related by the Poynting's theorem, showed excellent agreement with each other. To take into account the arbitrary orientation of an emitting dipole, the power flow was calculated separately for emitters aligned with each coordinate axis, and the overall enhancement was calculated as the average $\Psi(\mathbf{r}) = \frac{1}{3}\Psi_x(\mathbf{r}) + \frac{1}{3}\Psi_y(\mathbf{r}) + \frac{1}{3}\Psi_z(\mathbf{r})$ [224].

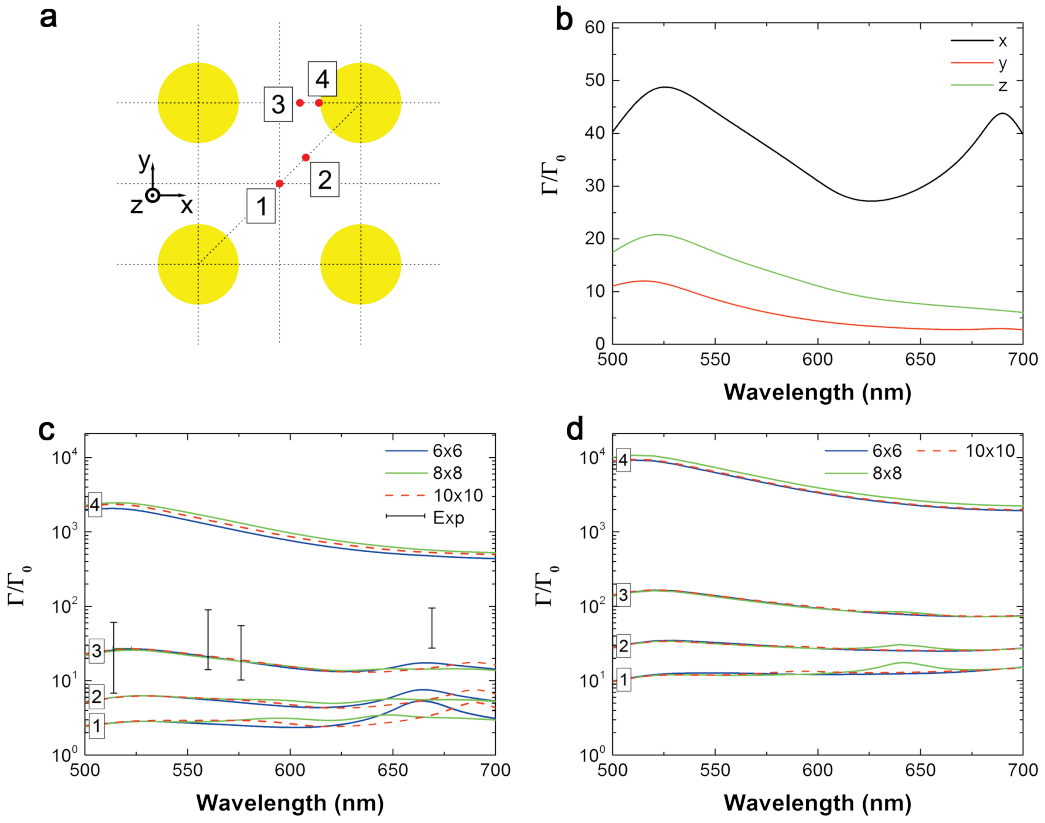

FIGURE 5.13: **Numerical simulations of the Purcell factor in metamaterials. (a)** Schematic of the metamaterial with the position of the emitters used in the simulations. All the emitters are situated in the middle of the nanorod length. **(b,c,d)** Spectral dependence of the Purcell factor for (b) a dipole with different orientations at position 3 inside the metamaterial, (c,d) a randomly oriented dipole at different positions inside the nanorod metamaterial (as indicated in (a)) for the metamaterials with (b,c) period $a = 100\ nm$ and nanorod radius $r = 25\ nm$ (as in the experiment) and (d) $a = 50\ nm$ and $r = 12.5\ nm$, corresponding to the same local effective medium parameters. The coloured lines in (c, d) correspond to different sizes of the finite nanorod array used in the simulations (as indicated in the legends) showing the convergence to the behaviour of the infinite metamaterial; bars in (c) represent the experimental data corresponding to the width of the lifetime distribution at 10% of the modal amplitude (Figure 5.11). In all simulations, the internal quantum yield of the emitter was considered to be 1.

In order to simulate an infinite number of nanorods in the metamaterial, the number of rods in the finite-size arrays was gradually increased with periodic boundary conditions on the sides of the nanorod patch. The convergence of the Purcell factor with the number of the nanorods within the simulation domain (Figure 5.13(c, d)) confirms that a 10×10

nanorod array with periodic boundary conditions can be used to analyse the behaviour of a dipole in infinite metamaterial. The averaging over the dipole position within the unit cell of the array of the metamaterial was performed, assuming a uniform distribution of the emitters, with a position-dependent decay rate and local excitation efficiency, and the excitation light illuminating the metamaterial from the substrate side. This yields the following expression: $I(t) \propto \int_{e-c} |\mathbf{E}_{pump}(\mathbf{r})|^2 Q_{loc}(\mathbf{r}) n(\mathbf{r}) e^{-\Psi(\mathbf{r})\Gamma_0 t} d^3r$. The integration was performed over the dye-filled volume within the elementary cell, taking into account the density distribution of emitters $n(\mathbf{r})$. $Q_{loc}(\mathbf{r})$ is a local quantum yield defining how much of the emitted power is measured in the far-field. The local pump intensity was found to vary by only 8% between 470 nm and 633 nm excitation wavelengths used in the experiment and was averaged for these values. Since this equation yields a multi-exponential decay, a similar procedure to the inverse Laplace transform was applied in order to recover the theoretically predicted lifetime distribution.

From the results obtained, it can be seen from Figure 5.12a that the spectral dependences of the enhancement of the emission rates observed either in experiments or from direct numerical solutions of Maxwell's equations have similar features. Both show a broad spread of lifetimes at all emission wavelengths and a weak wavelength dependence of the distribution. The experimental data show that the distribution of decay rate enhancements, from 10 to 100 (for the high and low-lifetime cut-offs, respectively, at 10% of the modal contribution), is almost independent of the wavelengths across elliptic, ENZ and hyperbolic regimes. The results of Figure 5.13(c) also confirm the strong dependence of the LDOS on the position of the dipole in the unit cell mentioned in the previous section.

5.5.4 Engineering emission lifetime with metamaterial non-locality

Adjusting the geometry and/or composition of a metamaterial opens the door for engineering the quantum optics inside the composites. This is illustrated in Figure 5.12 where the lifetime dynamics in the composite studied above are compared with the emission dynamics in a similar metamaterial with nanorod diameter and unit cell dimensions scaled by 50%. It is interesting to note that the reduction of the unit cell does not make the optical response of metamaterial appear more local; i.e., it does not lead to the enhancement of local density of states at ENZ and hyperbolic frequencies. Rather, 3D

numerical simulations and non-local effective medium theory predict that the reduction of unit cell size yields an order of magnitude higher broadband enhancement of decay rate (Figure 5.12 and Figure 5.13(c, d)), despite the local effective medium parameters of the metamaterial being the same. Note that both non-local EMT and numerical solutions of Maxwell equations predict comparable enhancement of the decay rate as a result of the unit cell reduction. As before, the quantitative difference between predictions of non-local EMT and numerical solutions reflects the limitation of an effective medium response, that nevertheless reveals the important physics and provides a relatively fast estimate of the radiation decay enhancement. Numerical solutions of Maxwell equations enable one to calculate the detailed optical response at any location at the expense of computational complexity and time.

5.5.5 Validity of the different approaches

Local effective medium theories, under some conditions, provide an avenue to understand and design transmission and reflection of composite media. However, as shown above, a local EMT drastically fails when applied to calculations of a macroscopic Purcell effect. At the same time, a non-local EMT can be used to calculate Purcell enhancement in nanorod composites. From the fundamental science standpoint, non-local EMT provides a quantitative description of the quantum optics of the composite, identifies the dominant decay channels for the molecules, and can be used to engineer these channels. From the applications standpoint, non-local EMT allows one to avoid complex and extremely time- and memory-consuming numerical solutions of Maxwell equations for applications that rely on macroscopic number of fluorophores, distributed throughout the composite. In applications that require analysis of a position dependent Purcell effect, numerical solutions of Maxwell equations cannot be avoided.

5.6 Conclusion

In summary, spontaneous radiation of an emitter inside nanorod-based metamaterials exhibiting non-local electromagnetic behaviour was experimentally demonstrated and analysed theoretically and numerically. It was shown that the effect of structural non-locality,

which results in the so-called additional electromagnetic modes in the metamaterial, has a significant impact on the density of photonic states inside the composite media and, as the result, quantum electrodynamic processes. The modal structure of a non-local composite material has a major impact on spontaneous decay dynamics, setting a fundamental limit on the overall emission rate enhancement and determines its spectral behaviour. Careful consideration of the structural non-locality allows the design of the density of optical states, with the geometrical parameters of the metamaterial composite, beyond the limitations of the standard effective medium model, thus opening new opportunities for engineering and tailoring quantum optical processes inside metamaterials.

Chapter 6

Spontaneous emission inside a hyperbolic metamaterial waveguide

Guided light is of particular importance to provide the capability of integrating new light sources, such as single-photon sources, into new photonic devices. So far, most of the studies have been focused on the effect of the local environment of the emitters on free-space radiated emission, and the known experimental and theoretical studies were dominantly limited to "infinitely" thick bulk metamaterials. Hence, no significant interactions between the slab boundaries were seen due to propagation losses, and effects related to waveguided or cavity modes were suppressed. In this study, the spontaneous emission properties of various dyes in a finite-size metamaterial design made of a nanorod-based planar waveguide were investigated.

While an "infinite" metamaterial was considered in the previous chapter, here, a planar waveguide with finite structure, e.g. finite thickness, was studied. It was shown that the structure of the guided modes plays a significant role in the modification of the spontaneous emission properties. An enhancement of the fluorescence coupled to the waveguided plasmon-polariton modes of the metamaterial was demonstrated. The spectrum and lifetime of the emission could be controlled separately for TM and TE polarisations by coupling to different modes of the waveguide.

6.1 Samples

The set of samples used in these experiments were made of gold nanorod-based HMMs embedded in a dye-doped polymethylmethacrylate (PMMA) matrix, as depicted in Figure 6.1. In order to probe the relationship between the Purcell factor and the specific regime of the metamaterial dispersion, several organic dyes were chosen with their emission wavelengths spanning the elliptic ($\varepsilon_{xx} > 0, \varepsilon_{zz} > 0$) and hyperbolic dispersion ($\varepsilon_{xx} > 0 > \varepsilon_{zz}$) regimes of the metamaterial.

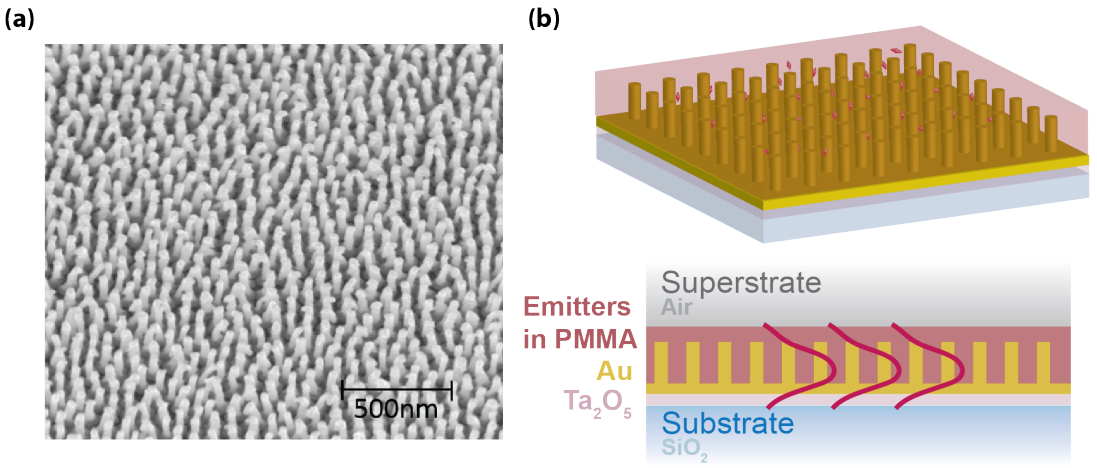

FIGURE 6.1: **Gold nanorod-based hyperbolic metamaterial planar waveguide** **(a)** SEM image of the nanorod-based metamaterial after removal of the AAO template (sample tilted at 30^o) and **(b)** 3D (top panel) and 2D (bottom panel) schematics of the dye-doped sample. The nanorods layer constitutes the planar waveguide, infinite in the directions perpendicular to the nanorods length and confined in the direction parallel to the nanorods.

Four identical samples were fabricated according to the process described in Chapter 4, using gold electrodeposition into an AAO matrix, which was subsequently removed. In this work, the metamaterial geometrical dimensions were approximately 38 nm rod diameter, 80 nm rod period and 150 nm rod length. The small geometrical parameters of a unit cell compared to the wavelength of the incident light allowed the anisotropic behaviour of the metamaterial to be described using an effective medium theory using the Maxwell-Garnett approximation. Using a transfer matrix method, the effective dielectric permittivity of the HMM could then be calculated. As shown in Figure 6.2, the nanorod-based metamaterial embedded in PMMA shows the presence of an epsilon-near-zero (ENZ) range around 596 nm, corresponding to the effective plasma frequency ω_p^{eff} of the metamaterial for which $\mathrm{Re}[\varepsilon_{zz}(\omega_p^{eff})] = 0$. This represents the onset of the hyperbolic dispersion regime

(grey area in Figure 6.2). Below this value, where all the components of the effective dielectric permittivity are positive, the dispersion regime is known as elliptic.

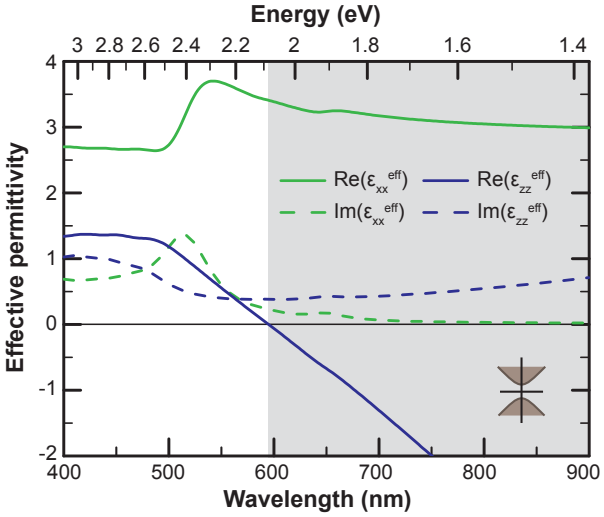

FIGURE 6.2: **Effective dielectric permittivity of the nanorod-based system embedded in PMMA.** The greyed area represents the hyperbolic dispersion regime of the metamaterial.

The dye-doped PMMA layer, with a doping concentration of 1.5 $wt\%$, was then spin-coated inside and on top of the metamaterial, forming a 50 nm overlayer above the metamaterial. Four laser dyes (Rhodamine perchlorate dyes) with different emission wavelengths distributed over a wide range of the visible spectrum were used: Rhodamine 590 (R590), Rhodamine 610 (R610), Rhodamine 640 (R640) and Rhodamine 700 (LD700). Figure 6.3 shows the absorption and emission spectra of the four dyes. The emission peaks of R590, R610 and R640 remain in the elliptic dispersion regime whereas the emission peak of LD700 is located in the hyperbolic dispersion regime of the metamaterial.

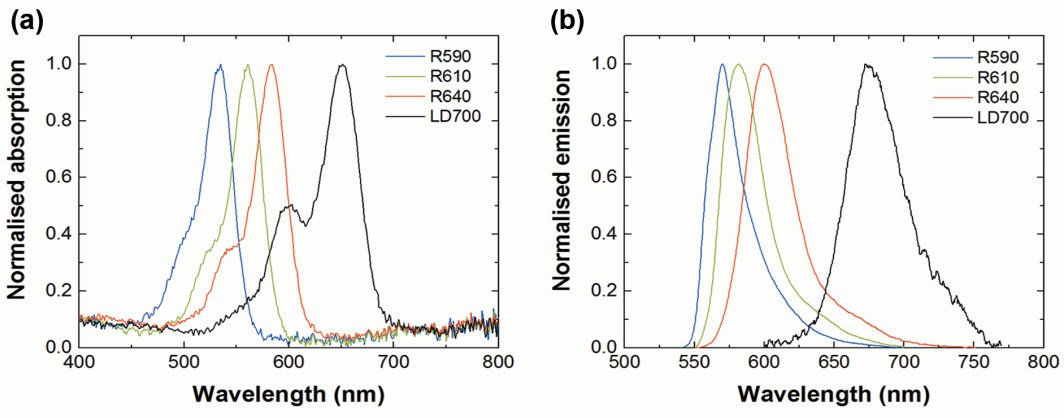

FIGURE 6.3: **(a) Absorption and (b) emission of rhodamine perchlorate dyes.**

6.2 Mode structure of the metamaterial waveguide

Figure 6.4 shows the experimental extinction spectra of the samples after annealing and before deposition of the dye. These spectra are typical of nanorod-based metamaterials and exhibit two distinct dipolar resonances: a transverse mode (T-mode), occurring at shorter wavelengths (520 nm) and associated with the electron motion perpendicular to the nanorod long axis and also a longitudinal mode (L-mode), excited when the electric field of the incoming light has a component along the long axis of the rods, dominating the spectrum at higher wavelengths (650 nm). The extinction spectrum of the sample on which the LD700 dye was deposited exhibit a 15 nm blue-shift compared to the other spectra. This could be due to a slight variation in the diameter of the pores after etching.

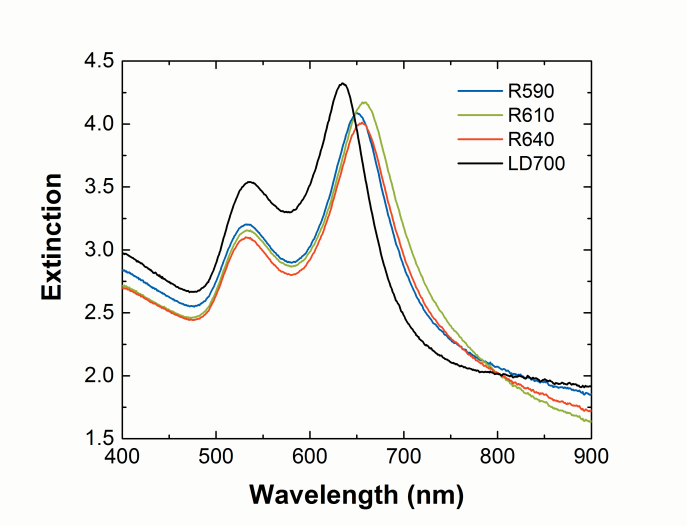

FIGURE 6.4: **Experimental extinction spectra ($-log(Transmission)$) of the four nanorod samples in AAO matrix after annealing at an angle of incidence of 45^o.**

The extinction spectra of the samples after deposition of the dye-doped PMMA layer are shown in Figure 6.5. The presence of the dye-doped PMMA matrix resulted in a blue-shift of the longitudinal mode to about 590 nm compared to the nanorods in their AAO matrix as $n_{PMMA} < n_{AAO}$. Along with both transverse and longitudinal modes, a third small peak corresponding to the absorption wavelengths of the dyes can be seen at different wavelengths for each sample. In the case of the sample with LD700 dye, this peak appears around 650 nm.

The experimental extinction spectra of the nanorod-based metamaterial embedded in the LD700-doped layer were then modelled via transfer-matrix method, using an effective

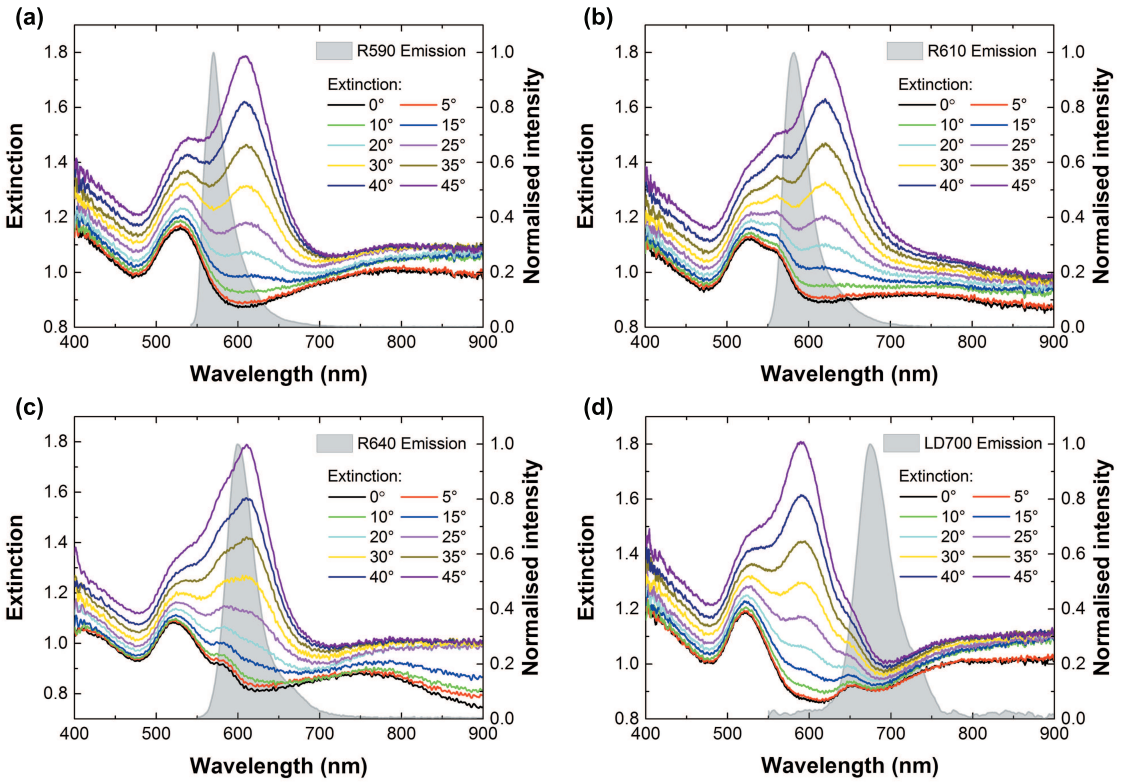

FIGURE 6.5: **Experimental extinction spectra** ($-log(Transmission)$) **of the four HMM samples after deposition of the dye-doped PMMA layers for different angles of incidence of TM-polarised light together with the emission spectra of the dyes.** **(a)** R590 sample, **(b)** R610 sample, **(c)** R640 sample, **(c)** LD700 sample.

medium theory for TM-polarised light. However, the modelled extinction spectra for the measured geometrical parameters were not in good agreement with the experimental spectra. The cause for this mismatch has been attributed to the fact that the dye-doped PMMA did not fully fill the space between the nanorods. To solve this issue in the modelling of the system, the refractive index of the embedding medium was slightly reduced from 1.49 (PMMA) to 1.41 to account for the partial filling of the layer. The results of the modelling in various embedding media are depicted in Figure 6.6 for the sample doped with LD700 and show a good agreement with the experimental spectra of figures 6.4 and 6.5d. For indication, the extinction spectra of the gold nanorods in air are depicted in figure 6.6b. In this case, the effective refractive index of the HMM is reduced and the longitudinal mode is strongly blue-shifted resulting in an overlap between the transverse and longitudinal modes.

In order to further study the mode structure of the metamaterial, the presence of waveguided modes situated between the light-lines of the substrate and the superstrate was investigated,

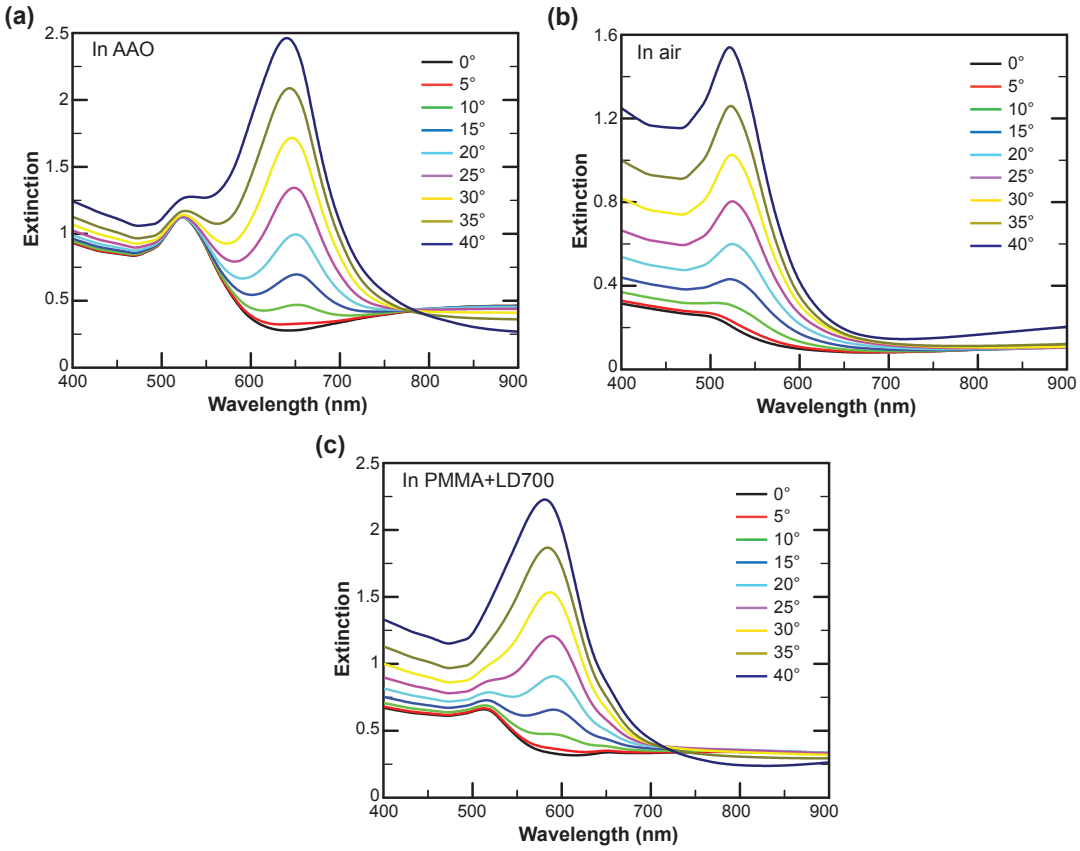

FIGURE 6.6: **EMT modelling of extinction spectra of the nanorod samples in various environments for different angles of incidence of TM-polarised light.** **(a)** Metamaterial in air, **(b)** Metamaterial in AAO matrix, **(c)** Metamaterial in LD700-doped PMMA.

as depicted in Figures 6.8(a, c). These modes can be accessed in total internal reflection using a prism coupler matched to the refractive index of the substrate, as depicted in Figure 6.7a. A local EMT was also used in order to model the dispersions of reflection for TE and TM polarisations (Figures 6.8(b, d)). It should be noted that while the local EMT can reasonably well predict far-field linear optical properties of a nanorod metamaterial [104] and waveguided modes [225], the Purcell effect can be significantly influenced by the non-local response of the composite [226]. The local EMT was used to describe only the waveguided mode structure of the metamaterial.

As evidenced by the experimental and modelled dispersions of reflection plotted in Figures 6.8(a, b), the metamaterial slab with the geometrical parameters considered here and in the spectral range of interest acts as a waveguide for bulk plasmon-polariton modes for TM-polarised waves. The mode observed exhibits almost flat dispersion near a wavelength of about 680 nm and thus a low group velocity (v_g). Therefore, a high LDOS (ρ) of the

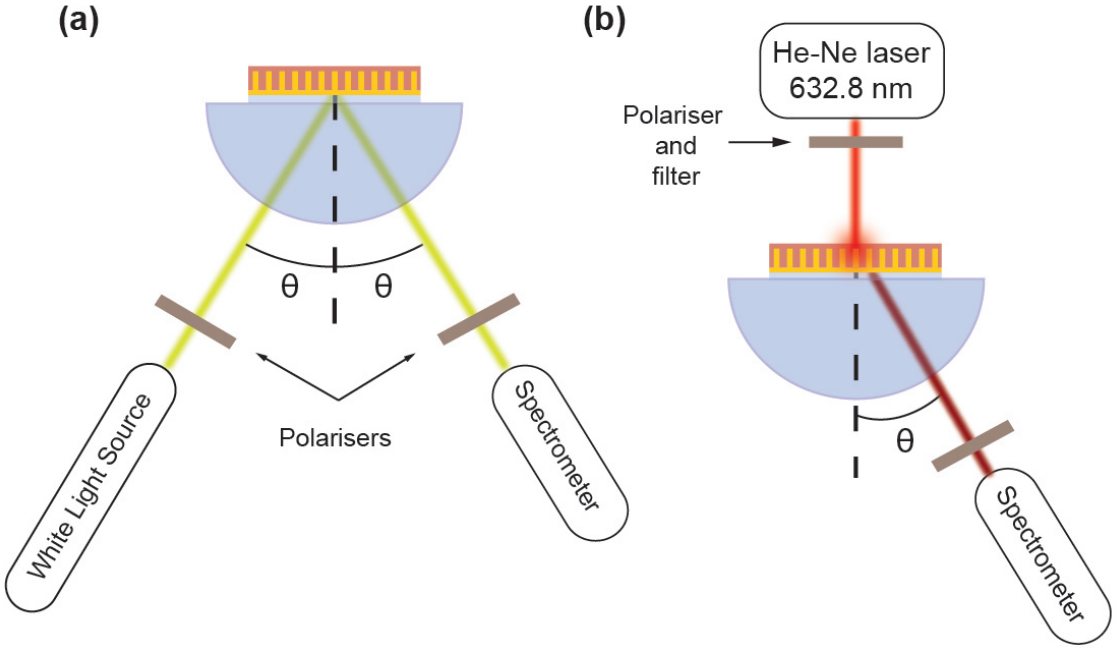

FIGURE 6.7: **Schematics of experimental setups for the measurements of dispersions of reflection and photoluminescence. (a)** ATR measurements **(b)** Photoluminescence measurements.

mode can be inferred since $\rho \propto 1/v_g$. Higher order TM modes, situated closer to the effective plasma frequency of the metamaterial, could not be seen in the experimental dispersion of reflection due to the large ohmic losses of gold in this spectral range. In that same wavelength range, the slab also supports a single conventional TE mode similar to transparent dielectric waveguides, as shown in Figures 6.8(c, d), since it is only affected by the $\varepsilon_{xx} = \varepsilon_{yy} > 0$ components of the effective permittivity tensor of the metamaterial slab. The strong spectral overlap between the TM1 mode of the metamaterial slab and the emission spectrum of the bare LD700 dye (Figure 6.8), can lead to a significant coupling of the emitted light into this mode. As a result of the random orientations of the molecules inside the matrix, the emission of the dye can couple to both TE and TM modes of the metamaterial. Spontaneous emission into the TM mode is however favoured due to the large spectral overlap with the bare dye emission spectrum.

6.3 Photoluminescence coupled to the metamaterial mode

The coupling of the photoluminescence of the LD700 dye to the waveguided modes of the metamaterial was probed by measuring the emission of the dye using radiation leakage for

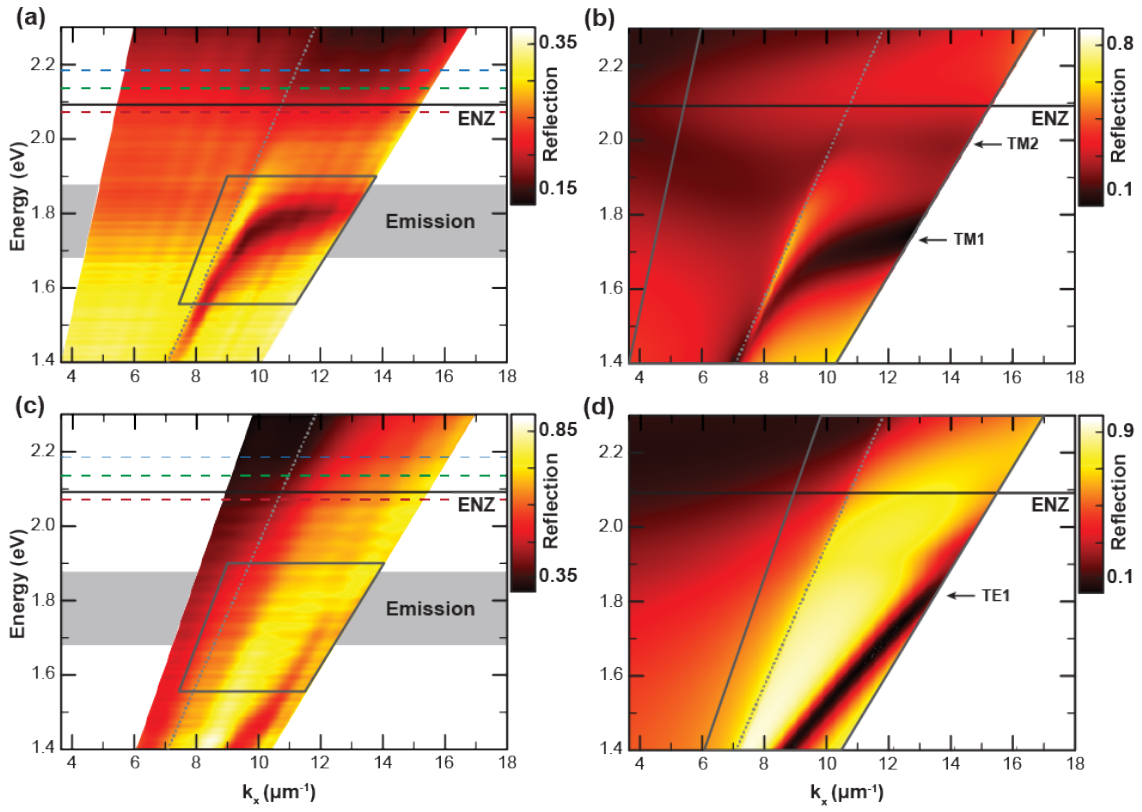

FIGURE 6.8: **Mode structure of the metamaterial slab.** Reflection dispersions of the metamaterial slab waveguide for **(a, b)** TM and **(c, d)** TE polarisations: **(a, c)** experimental measurements and **(b, d)** EMT modelling. The position of the effective plasma frequency of the metamaterial (solid horizontal line), the light line in air (grey dotted line), the emission band of the LD700 dye (greyed region) and the peak emission wavelengths of the other dyes studied (dashed lines, color coding as in figure 6.5.

both TE and TM polarisations. To do so, the measurements were performed in the same configuration as reflection measurements, where the sample was placed in contact with a hemi-cylindrical prism coupler and excited with a $5mW$ He-Ne laser, as depicted in Figure 6.7b. The spectral dependences of the PL intensity, for both TE and TM polarisations, were separately measured for different detection angles and then normalised to the PL spectrum near normal incidence (at an angle of 5^o), revealing the influence of the coupling to the waveguided mode. The quantum yields of the four emitters where measured by a relative determination method, using the known quantum yield of R610 dye from the literature ($Q_{R610} = 0.95$). The following quantum yields were then obtained for the other emitters: 0.54 for R590, 0.76 for R640 and 0.25 for LD700.

Figure 6.9a shows the experimental angular dispersion of the TM-polarised photoluminescence, which follows the dispersion of the TM waveguided mode. This indicates the

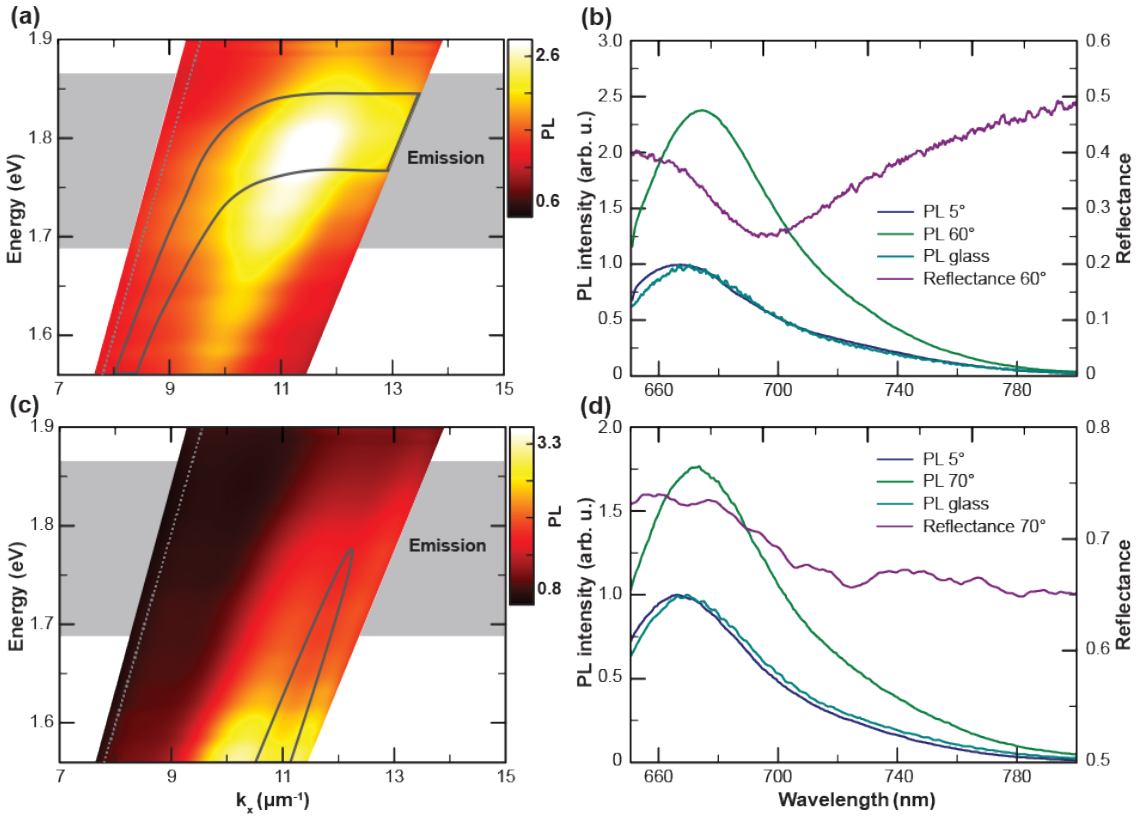

FIGURE 6.9: **Emission in waveguided modes. (a, c)** Experimental dispersions of the photoluminescence enhancement measured for **(a)** TM and **(b)** TE polarised emission. The PL spectra are normalised to the PL spectrum near normal detection (5^o). The position of the TM and TE modes from Figures 6.8(a, c) are added as a guide to the eye. The position of the light line in air (grey dotted line), the emission band of the LD700 dye (greyed region) are represented. **(b, d)** Spectra of the photoluminescence measured for the LD700-doped PMMA on a glass substrate and in the metamaterial at a detection angle of 5^o, 60^o (in (b)), 70^o (in (d)) and the corresponding reflectance spectra for (b) TM and (d) TE polarised light. The PL spectra on glass and near normal detection are normalised to 1, the PL spectrum at higher angles of detection are normalised to the maximum intensity measured at 5^o.

predominant coupling of the emission to the mode, where the photoluminescence intensity is 2.5 times stronger than the photoluminescence intensity scattered directly into free-space, despite the additional losses associated with the waveguiding of bulk plasmon-polaritons in the metamaterial slab. According to Figure 6.9b, a red-shift of the emission maximum is observed with respect to the emission of LD700 in a PMMA matrix deposited on a glass substrate. This shift is consistent with the dispersion profile of the guided mode and is determined by the overlap of the LDOS associated with the mode, the dipolar emission spectrum of the fluorophores inside the metamaterial layer and their spatial distribution inside the nanorod array. Even higher emission enhancements can in principle be achieved by further adjusting the waveguide dispersion to the emission spectrum of the

fluorophores, which can be done by carefully varying the thickness of the metamaterial waveguide. Similarly to the TM-polarized PL, the TE-polarised photoluminescence follows the dispersion of the TE waveguided mode but the intensity increase is however lower than for the TM-polarised waveguided emission as shown in Figure 6.9c. It should be noted that the high relative intensity increase in Figure 6.9c can be seen at the wavelengths away from the emission peak in the polymer matrix, which corresponds to the wavelength range where the overall PL intensity is very low (Figure 6.9d), causing a high relative enhancement.

6.4 Time-resolved photoluminescence

The spontaneous emission rate of the four laser dyes was then investigated on a glass substrate as well as inside the metamaterial using the TCSPC setup described in Chapter 4. TM-polarized excitation light (532 nm for R590/R610/R640 and 633 nm for LD700) was focused on the sample with a 4x, $NA = 0.10$ objective and the resulting PL collected by a high numerical aperture objective (90x, $NA = 0.90$), within a 64^o angle range, corresponding to the numerical aperture of the objective. Different filters were used to remove the laser contribution to the measured light. Time-resolved PL decays of the emitters were measured inside the metamaterial and in a polymer matrix for reference.

Although the emission wavelengths of the R590, R610 and R640 dyes are outside the region of the bulk plasmon-polariton modes, they all remain close to the ENZ wavelength range and experience the influence of their local electromagnetic environment. The contribution of all optical modes available for the emitters to decay was measured, collecting all the emission angles up to the numerical aperture of the objective used. While mono-exponential decays of the photoluminescence have been observed for the emitters in a PMMA layer deposited on glass, a more complicated decay profile has been measured for the emitters placed inside the metamaterial as depicted in Figures 6.10(a, c). This is consistent with a distance and polarisation dependent distribution of the emitters within the nanorod-based metamaterial, leading to a distribution of the spontaneous decay rates [169] and thus, multi-exponential decays of the photoluminescence. In order to analyse the emitters decay dynamics, the inverse Laplace transform method described in chapter 4 was used to extract the distribution of lifetimes shown in Figures 6.10(b, d).

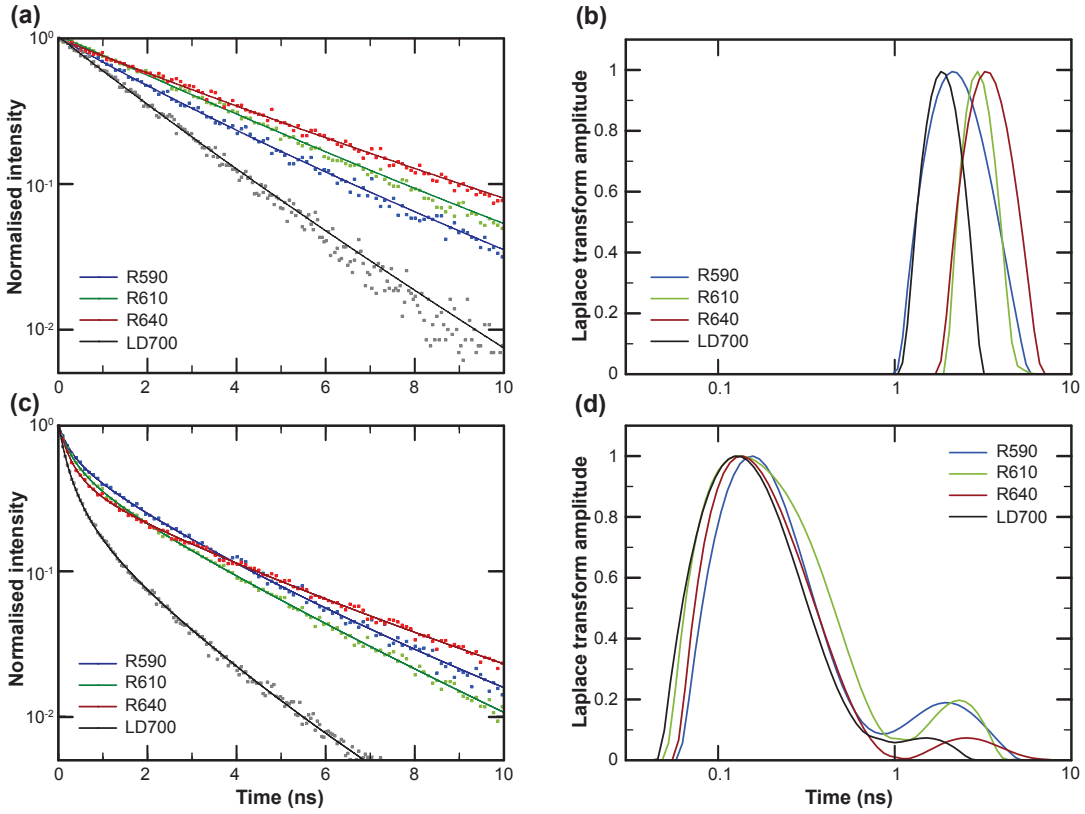

FIGURE 6.10: **Fluorescence dynamics of the emitters and fluorescence lifetime distributions. (a, c)** Fluorescence dynamics of the four dyes embedded in a PMMA layer and deposited (a) on a glass substrate and (c) inside the metamaterial. Solid lines represent the dynamics recovered by applying an inverse Laplace transform method to the experimental data (dotted lines). **(b, d)** Experimental fluorescence lifetime distributions extracted from the time-resolved photoluminescence measurements (b) on a glass substrate and (d) inside the metamaterial.

While the different dyes exhibit fluorescence lifetimes comprised between 2 and 3 ns when embedded in an uniform PMMA matrix, strongly modified decay rates have been observed for all emitters when constrained by the metamaterial as shown in Figure 6.10(c, d). The lifetime distributions observed in Figure 6.10(b, d) are strongly determined by the emitters' positions within the metamaterial and may be strongly influenced by its non-local response [226]. Indeed, on a microscopic level beyond the effective medium approximation, such nanorod-based metamaterials support cylindrical surface plasmons close to the emission wavelength of the dyes emitting both in the elliptic and hyperbolic dispersion regimes [105, 223]. In this case, a strong enhancement of the spontaneous emission of emitters placed in the vicinity of the nanorods is predicted [169]. For the emitters in the metamaterial environment, two distinct families of lifetimes are observed (Figure 6.10d), one corresponding to a lifetime reduction of 2-3 times and the other with a

broad distribution which corresponds to the strongest decay reduction of almost 50 times.

6.5 Numerical simulations

A pre-built model implemented in Comsol Multiphysics software was then employed for the numerical simulations of the spontaneous emission properties of a emitter inside or in the vicinity of the nanorod array. The full-vectorial numerical modelling takes into account the local fields, which were not described by the local EMT. The nonlocal corrections for the waveguided modes considered in this work is estimated from comparison between the EMT and numerical simulations to be of the order of a few percent. In these simulations, the modification of the decay rate was determined as the ratio of power flow flux from a point dipole emulating the dye emitter placed at a given position inside or outside the metamaterial to the corresponding power flow for a dipole in uniform PMMA [111]. In order to model an infinite nanorod array, finite-size square arrays were modelled with their sizes gradually increased, while the convergence of the results was monitored. The simulation domain was surrounded by a set of perfectly matched layers ensuring the absence of reflections form the outer boundaries. The observed results revealed that a 8×8 nanorod array can be used to analyse the dye emission in an infinite metamaterial slab. The two same methods described in Chapter 5 were used in order to calculate the power flow flux $F(\mathbf{r})$. The first method consisted in integrating the Poynting vector over a surface of a small sphere of radius 5 nm enclosing the point dipole, while the second used the dipole energy dissipation rate $W(\mathbf{r}) = -\frac{1}{2}\,\mathrm{Re}\,[\mathbf{J}^*(\mathbf{r}) \cdot \mathbf{E}(\mathbf{r})]$, where $\mathbf{E}(\mathbf{r})$ is the electric field of the dipole at the position of the dipole and $\mathbf{J}(\mathbf{r})$ is the dipole current. To take into account the arbitrary orientation of emitting dipole, the power flow flux was calculated separately for dipoles directed along each of the coordinate axes, and the averaged value was calculated as $F(\mathbf{r}) = \frac{1}{3}F_x(\mathbf{r}) + \frac{1}{3}F_y(\mathbf{r}) + \frac{1}{3}F_z(\mathbf{r})$ [224].

By comparing the experimental results to the numerical simulations, these two families of lifetimes can be ascribed to the emitters situated in a polymer layer above the metamaterial (weak decay rate modification) and within the metamaterial (strong decay rate modification). Numerical modelling confirms a strong position dependence of the spontaneous emission rate with respect to the nanorod in both lateral directions (xy-directions) as well as with respect to the surface of the metamaterial waveguide (z-direction). This is

illustrated by the simulated power flow along the waveguide for the emitters at different positions within the waveguide. In particular, the efficient coupling to the TM1 mode, observed experimentally in Figure 6.9a is confirmed by the simulations (Figure 6.11d). In a good correspondence between simulations and experiment, the TM mode is narrower and TE mode is much broader. As expected, the most efficient coupling to TE and TM modes is achieved for the emitters at different positions in the metamaterial slab as it strongly depends on the emitter position with respect to the mode profile (Figure 6.11(c, d)).

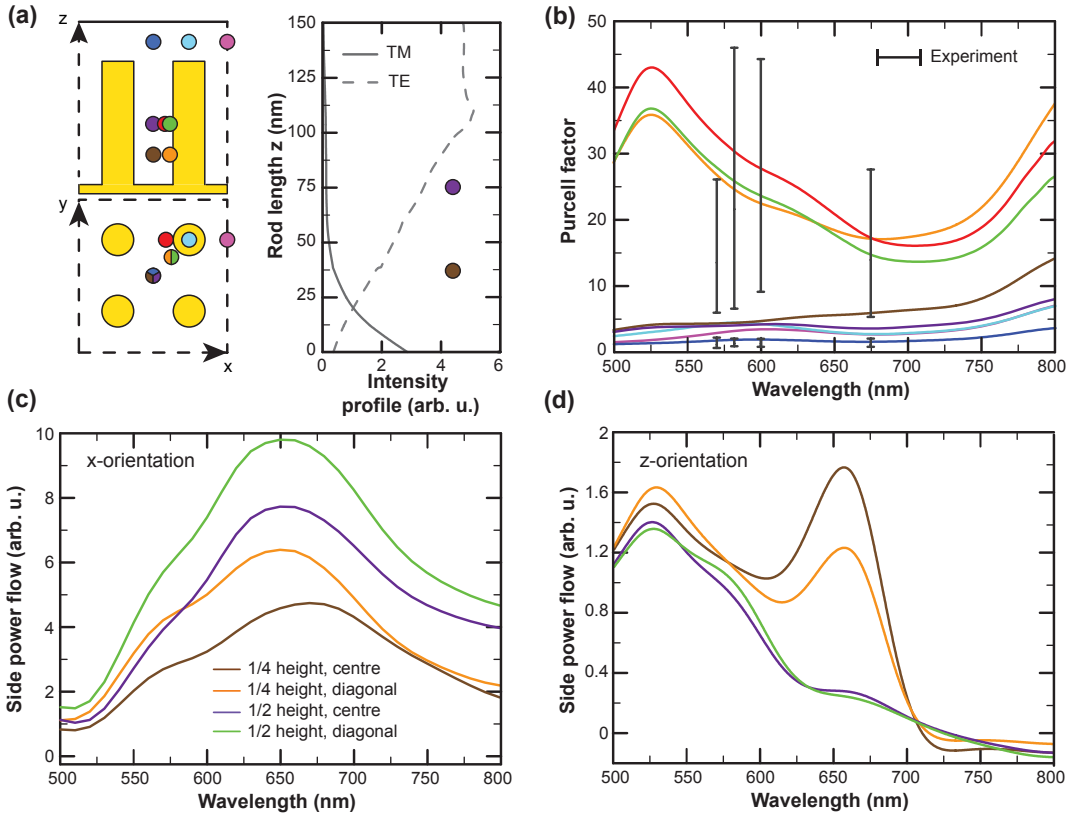

FIGURE 6.11: **Numerical simulations of the spontaneous emission rate modification inside a nanorod-based HMM. (a)** Left panel: Side and top views of a 4×4 nanorod array. The eight coloured dots represent the different positions of the dipoles considered in the simulations. Right panel: intensity profiles of TE-polarised ($|E_x|^2$) and TM-polarised ($|E_z|^2$) modes propagating in the y-direction. **(b)** Spectral dependence of the lifetime averaged over the dipole orientation for different locations of the dipoles represented in (a). The black vertical bars correspond to the experimental data related to the width of the lifetime distribution at 50 % of the modal amplitude for both peaks in Figure 6.10d). **(c, d)** Side power flow integrated over an 8×8 nanorod array for different locations of a dipole oriented in the (c) x-direction and (d) z-direction inside the metamaterial (colour coding as in (c)).

The fluorescence processes inside the nanostructured composite have a complex nature. Emitters situated inside metamaterials are always influenced by the near-field of adjacent

nanorods where the electromagnetic field is dominated by high-wavevector components [219]. In this case, a conventional EMT theory, which does not account for internal local fields, is not applicable, and the interaction of the near-field with the exact nanorod geometry needs to be considered. It should be noted, however, that the extension of EMT to take into account the non-local effects, allows a partial description of local plasmonic fields and thus related fluorescence processes [105, 226]. At certain wavelengths, this near-field-mediated emission may then be coupled to a set of the metamaterial slab modes [169, 217]. These modes can be adequately described by the EMT and describe the fluorescence evolution in the far-field of the emitter and its outcoupling to free-space.

The transition dipole moments of the dye molecules dispersed in PMMA have random orientations. Hence, they can emit into both TM and TE modes of the metamaterial slab and subsequently out-couple in free space beyond the metamaterial. The emission efficiency in each particular mode depends on the emitter position with respect to the adjacent nanorods, dipole moment orientation and the field distribution of the slab modes at the emission frequency.

The role of the availability of the slab modes can be clearly seen in the experimental results (Figure 6.9(a, c)): at lower frequencies, the emission into the metamaterial slab is dominated by the TE-polarised mode, while at $\approx 1.8\ eV$ (corresponding to the wavelength of 700 nm), the TM mode starts to play an essential role. The same can be observed in the numerical results (Figure 6.11(c, d)). The coupling to the TM mode is efficient only for the dipole located at the quarter-rod height. This is due to the field overlap with the available waveguided mode strongly localized near metamaterial-substrate interface (right panel of Figure 6.11a), whereas the TE mode profile extends across the metamaterial slab.

The integrated free-space emission following outcoupling of the modes in the substrate and superstrate, integrated over all angles in glass and in PMMA amounts to 5—16 % of the intensity emitted by the dipole in the slab. For example, for the wavelength of 670 nm, 8 % of the total emission is outcoupled in the superstrate and 5 % in the substrate for the dipole in the centre of the unit cell (purple dipole in left panel of Figure 6.11a) as shown in Figure 6.12a. The remaining energy is coupled to the metamaterial modes and eventually dissipated. At the same time for the dipoles diagonally located inside the metamaterial (green dipole in left panel of Figure 6.11a), the out-coupling efficiency in free space is

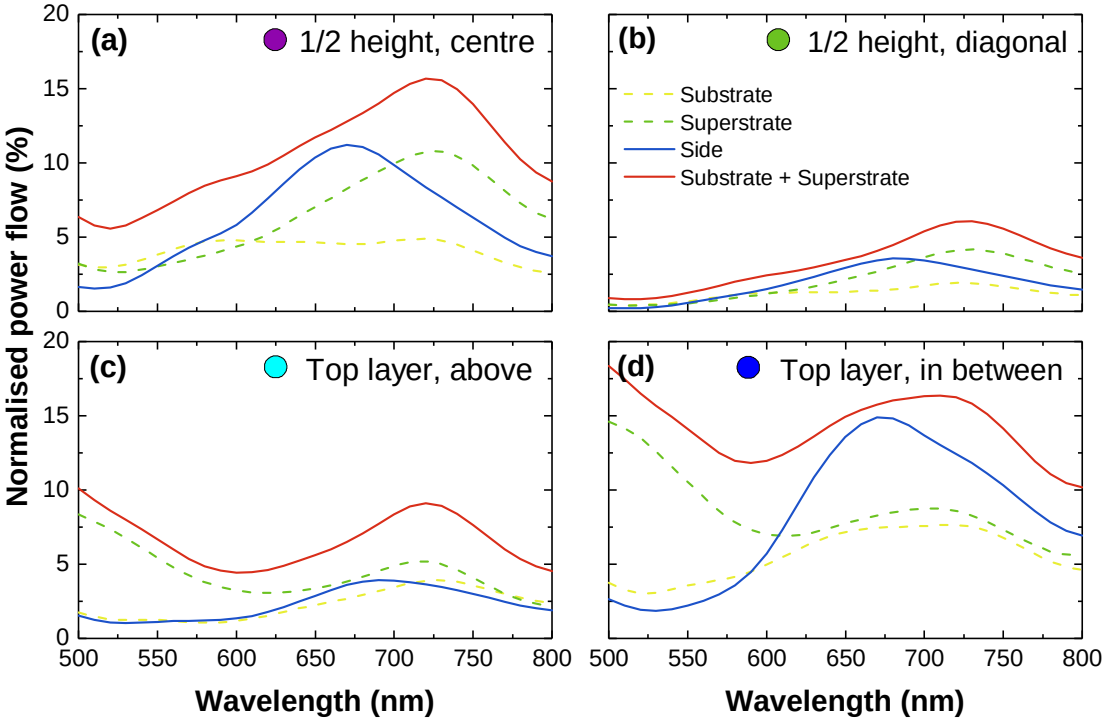

FIGURE 6.12: **Spectral dependence of the emission intensity of the dipole into various channels for different positions of the dipole in the unit cell.** Percentage of the total emission intensity of the dipole coupled to the waveguided mode of the system, and outcoupled to free-space in the substrate or the superstrate for the dipole **(a)** at 1/2 rod height, central position, **(b)** at 1/2 rod height, diagonal position, **(c)** in the overlayer, above a rod and **(d)** in the overlayer, in between rods. The colour coding is as in Figure 6.11.

only 1-6 %, depending on the emission wavelength, as the quenching is higher for these positions of the emitters, since they are located closer to the nanorods (Figure 6.12b).

Similarly, for emitters outside but in the near-field proximity of the metamaterial slab (dark blue dipole in left panel of Figure 6.11a), free-space radiation accounts for 10-18 % of the total radiation depending on the wavelength, with, for a wavelength of 670 nm, 8 % of the total emission directed in the superstrate and 7 % in the substrate primarily via the metamaterial mode (Figure 6.12d). The rest of the emission is coupled to truly-waveguided metamaterial modes which are not coupled to the superstrate and dissipated. For the emitters situated above individual rods (light blue dipole in left panel of Figure 6.11c), the coupling to free-space radiation corresponds to 4-10 % depending on the wavelength, with at 670 nm, 4 % emitted in the superstrate and 3 % in the substrate (Figure 6.12e). Therefore, far-field emission efficiency is not strongly dependent upon whether emitters are

placed inside or outside the metamaterial since the high density of optical states ensures significant emission radiation in the waveguided metamaterial modes.

These observations also confirm that the mode structure of the metamaterial layer or resonators may have a more significant role in the waveguided or free-space emission intensity, while the rate enhancement effect is, to a large extent, determined by the local fields near the nanorods [221]. Thus, despite the high Purcell factor observed for certain emitter locations, the overall intensity enhancement is moderate, due to the averaging over all the positions of the emitters inside the metamaterial. Nevertheless, in the experiments with precisely positioned single molecules, both strong reduction of the lifetime and increase of the total emitted intensity should be pronounced. In the nanorod metamaterial, the ultimate limit of the lifetime shortening is defined by the practical cut-off of the available modes with large wavevectors associated with cylindrical surface plasmons of the nanorods and their interaction as well as material losses [226]. Smaller separations and lower losses would allow higher-wavevector modes accepted by the metamaterial composite, and the practical limit is defined by the available fabrication methods. Other factors limiting the lifetime shortening are related to the emitters' positioning [226] and their non-negligible size [96].

Effective quantum yield is another important consideration for spontaneous emission engineering in addition to the decay rate. Various plasmonic nanoantennas provide modest rate enhancements with reasonably good quantum yield but the emission is radiated in free space. For practical, integrated optics applications, the coupling to waveguided modes is beneficial, which can be achieved with the proposed approach. The propagation lengths of the TM hyperbolic waveguided modes in a plasmonic metamaterial are quite small due to the strong field confinement and are on the order of a few μm depending on the wavelength, as estimated from numerical simulations, which corresponds to few hundreds of nanorods. However, such metamaterial waveguides can be seamlessly integrated in low-loss (e.g., Si-based) waveguides [227] for making use of bright and fast light sources provided by high Purcell enhancement. The interplay between the emission rate increase, the quantum yield (influenced by non-radiative quenching), and coupling to a required waveguided mode strongly depends on the position of the emitters with respect to the nanorod forming the metamaterial as was shown in [226] and in this work.

6.6 Conclusion

In this chapter, the spontaneous emission inside a hyperbolic metamaterial slab has been investigated and the role of the waveguided modes of the metamaterial layer in this process has been highlighted. A very strong, almost 50-fold, acceleration of the spontaneous decay has been observed for emitters inside the metamaterial slab, which is strongly position dependent. At the same time, only weak rate modification (2-3 times) was observed for the emitters in the proximity to the metamaterial waveguide interface. In both cases, up to approximately 18% of the radiation, depending on the emitter position with respect to the nanorods, is coupled to far-field radiation in the substrate and the superstrate, with the remaining energy coupled to the true waveguided modes of the slab. These results demonstrate the capability of such active hyperbolic metamaterials to exhibit highly tuneable electromagnetic properties for the design of integratable enhanced and fast light sources for various nanophotonic components with the potential to enable the creation of highly integrated single-photon sources. The emission coupled to a metamaterial waveguide can be accessed by incorporating a metamaterial slab in or onto dielectric photonic waveguides, including Si photonic circuitry. Spontaneous emission modification inside hyperbolic metamaterial waveguides can also be implemented in other systems, such as metal-dielectric multilayers or natural hyperbolic materials, potentially allowing a more controllable positioning of the emitters inside the waveguide.

Chapter 7

Spontaneous emission enhancement of a long-lifetime Ruthenium complex in metamaterials

Phosphorescent dyes typically show long lifetimes compared to conventional fluorescent dyes, owing to the nature of the transitions involved in the spontaneous emission process. In this chapter, the spontaneous emission of a Ruthenium complex $Ru(dpp)_3Cl_2$ is studied in different material environments. Very large reductions of the spontaneous emission lifetime are shown for emitters placed on a thin gold film and inside a nanorod-based hyperbolic metamaterial, reaching factors up to 2800. The key mechanism of the enhancement, in this case, failed to be predicted by the standard electromagnetic local density of states description, typically employed for the Purcell factor analysis of dipolar transitions.

7.1 Ruthenium complex

In this study, Ruthenium-tris(4,7-diphenyl-1,10-phenanthroline) dichloride complex dissolved in both water and glycerol was used at a concentration of $4 \times 10^{-6}\ mol.L^{-1}$. Figure 7.1 depicts the structural formula of the complex.

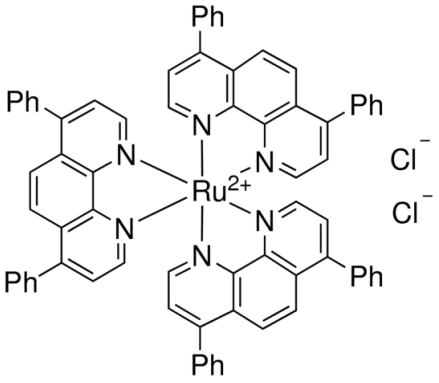

FIGURE 7.1: **Structural formula of Ruthenium-tris(4,7-diphenyl-1,10-phenanthroline) dichloride complex.**

$Ru(dpp)_3Cl_2$ is a transition metal complex which is constituted of a central ion of Ru^{2+} surrounded by 3 diphenyl-phenanthroline ligand molecules to form the complex. Due to the presence of the ligands, these complexes exhibit unique electronic transitions involving charge transfer from the d-orbitals of the metal to the ligands which are called metal-to-ligand charge-transfer (MLCT) states. Following absorption to the MLCT singlet state, fast and efficient intersystem crossing occurs and electrons relax to the triplet MLCT state. Emission from this triplet state is classified as phosphorescence and exhibits lifetimes typically of the order of several microseconds, shorter than usual phosphorescent states lifetimes [11]. This efficient intersystem crossing and reduced lifetime of the triplet excited state is due to the presence of the Ruthenium transition-metal ion, inducing strong spin-orbit interactions and leading to the mixing between the singlet and triplet excited states. This mixing ultimately enables the theoretically spin-forbidden triplet to ground-state transitions and therefore increases the efficiency of the phosphorescence process [228, 229]. Is is also worth mentioning that the emission of this complex is strongly reduced by the presence of oxygen due to dynamic quenching.

7.2 Nanorod metamaterial

As in the previous chapters, the nanorod-based metamaterial was fabricated by gold electrodeposition into highly ordered nanoporous AAO on a glass coverslip, using the two-step anodisation procedure described in Chapter 4. The geometrical parameters of the nanorod-based metamaterial used in the following experiments were approximately

50 *nm* rod diameter, 100 *nm* rod spacing and 150 *nm* rod length. Figure 7.2 depicts the extinction spectra of the free-standing nanorod-based metamaterial.

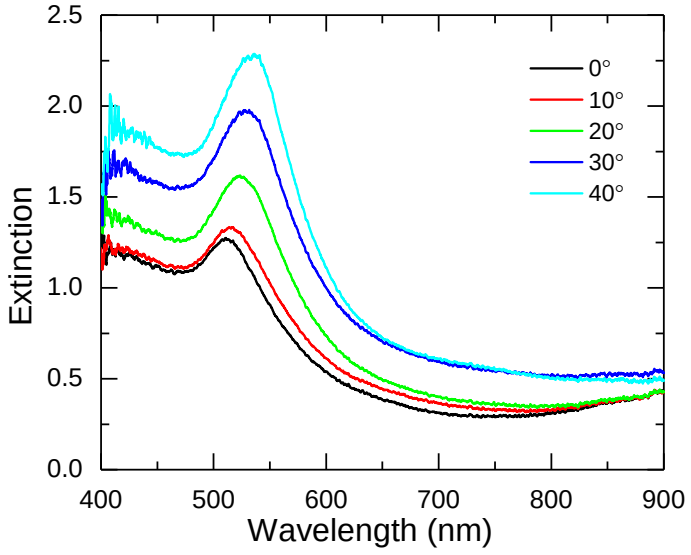

FIGURE 7.2: **Experimental extinction spectra ($-log(Transmission)$) of the free-standing nanorod-based metamaterial.**

Employing the TCSPC technique described in Chapter 4, the decay dynamics of the Ruthenium complex in both water and glycerol were measured. Three material environments have been considered: a glass substrate, a 50 *nm* gold film and the nanorod-based metamaterial. For this study, a 475 *nm* excitation wavelength was chosen, according to the absorption spectrum of the complex. The laser beam was focused on the sample using a 100× oil immersion objective with a numerical aperture of 1.3 and the photoluminescence signal collected via the same objective. A 488 *nm* longpass dichroic mirror and a bandpass filter (620 *nm*, bandwidth 40 *nm*) centered on the emission peak of the complex were used for the lifetime measurements. Fluorescence spectroscopy has also been performed for the emitter on glass and inside the metamaterial.

7.3 Experimental results

7.3.1 $Ru(dpp)_3Cl_2$ in water

The results of the time-resolved study of the Ruthenium complex in water for different material environments are presented in Figure 7.3. The experimental decay dynamics are represented in Figure 7.3a together with the fit performed using the inverse Laplace transform method described in Chapter 4. The corresponding lifetime distributions are shown in Figure 7.3b.

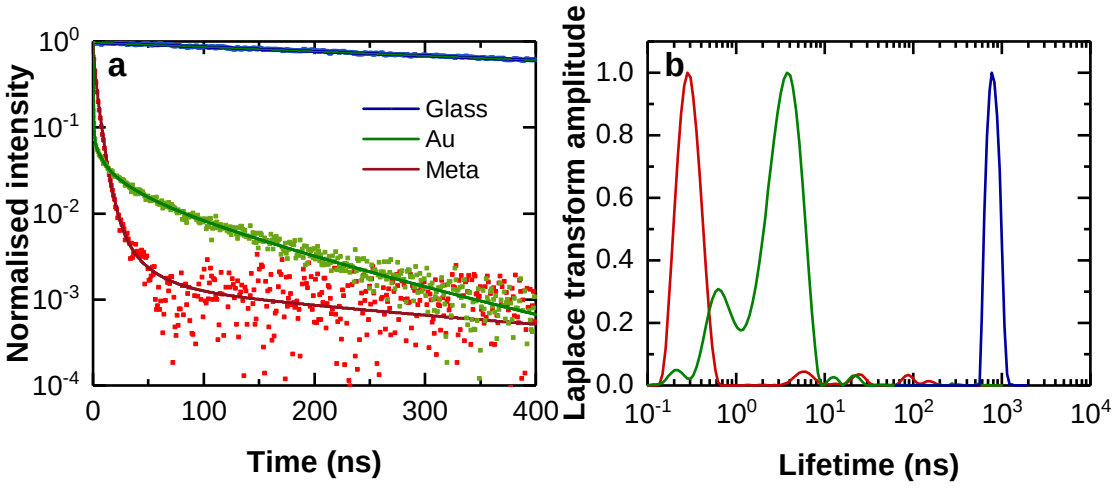

FIGURE 7.3: **Time-resolved analysis of $Ru(dpp)_3Cl_2$ in water. (a)** Emission dynamics and **(b)** lifetime distributions for the emitters on a glass substrate (blue), on a 50 nm thick gold film (green) and inside the nanorod-based metamaterial (red). In (a), the dotted lines represent the experimental measurement and the solid lines are the fit performed using the inverse Laplace transform method.

In the case of the complex deposited on glass, the experimental decay dynamics is mono-exponential with a component of the lifetime distribution centered around 830 ns. The measurements on the gold film and inside the nanorod-based metamaterial exhibit much more complicated decay dynamics. For emitters placed on the gold film, the dependence of the lifetime on the position of the emitters with regard to the gold surface led to a multi-exponential decay, as can be seen from Figure 7.3(a, b). The gold-film modified distribution is centred on 3.8 ns, corresponding to the Purcell factor of approximately 220. The large span of the lifetime distribution is mainly related to the distance and polarisation dependent distribution of the emitters with regard to the environments but can also be influenced by the level of noise in the experimental data.

The dynamics of the emitters, modified by the presence of nearby plasmonic surfaces, in particular made of noble metals, is well understood. As described in Chapters 3 and 5, the modification of the spontaneous emission lifetime is mainly due to mirror-reflected waves, excitation of surface waves and quenching [111], which all apply in this case. Therefore, the theoretical prediction of the distribution on the gold film was then obtained using the theoretical formulation of the Purcell enhancement near a gold film developed in Chapter 5 section 5.5.1. This method takes into account the position with regard to the metallic surface and the spatial orientation of the emitter, as well as the experimentally measured lifetime distribution of the Ruthenium complex on glass slide. An internal quantum yield of 0.4 was used for the complex in water, which is the maximum value found in the literature.

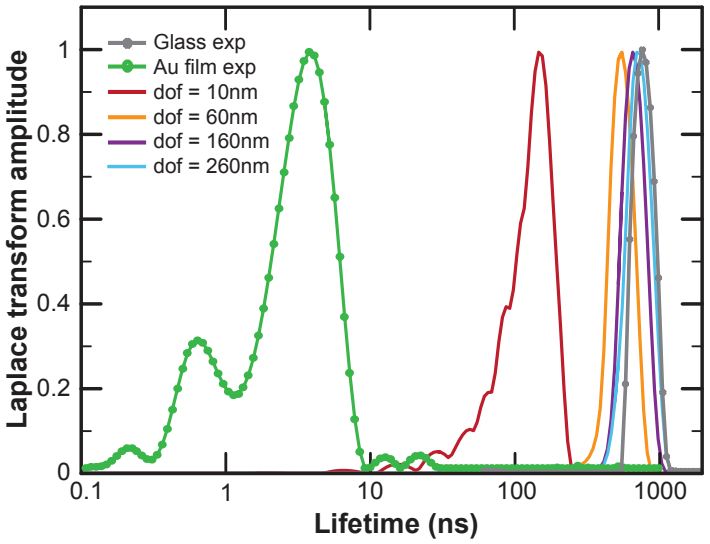

FIGURE 7.4: **Theoretical lifetime distributions above the smooth gold surface recalculated from the measured lifetime distributions of the complex in water deposited on glass for different depth of focus (dof).** Lines with symbols are experimental data measured on glass and above the gold film, lines only are the theoretical estimations.

From the results depicted in Figure 7.4, it is observed that even for a very small depths of focus (which is not realistic in the conducted experiments), the theoretical estimations of the lifetime distributions on the gold film remain orders of magnitude larger than the lifetime distributions observed in experiments. It is worth noting that this fitting approach was conducted on conventional fluorescent dyes in Chapter 5 and led to a good agreement between theoretical and experimental approaches, verifying the validity of the method.

The Ruthenium complex in water was then deposited inside the nanorod-based hyperbolic

metamaterial, following removal of the AAO template in which the nanorods were electrochemically grown. The resulting time dynamics and lifetime distributions are shown in Figure 7.3(a, b). The distribution shows a maximum peak around 0.28 ns, corresponding to an almost 3000-fold enhancement of the spontaneous emission lifetime. As described in Chapter 5, local effective properties of the metamaterial cannot be directly employed for the calculation of the emitters' dynamics. However, a comprehensive analysis of the decay rates of emitters inside a nanorod-based metamaterial, taking into account spatial averages and non-local corrections was developed [226]. Being proven to predict the correct decay rates in the case of widely used dipolar fluorophores, the theory predict an averaged Purcell enhancement of about 30, also consistent with other reports. However, in the reported case and similarly to the gold film scenario, the proven theoretical description fails to predict the modification of the spontaneous emission lifetime. Therefore, this approach relying on the modification of the LDOS appears to be inapplicable in the case of phosphorescent emission.

The emission spectra of the complex on glass and inside the metamaterial are depicted in Figure 7.5. A slight red-shift of the emission inside the metamaterial is observed with regard to the complex deposited on glass, owing to the interaction with the nanorods.

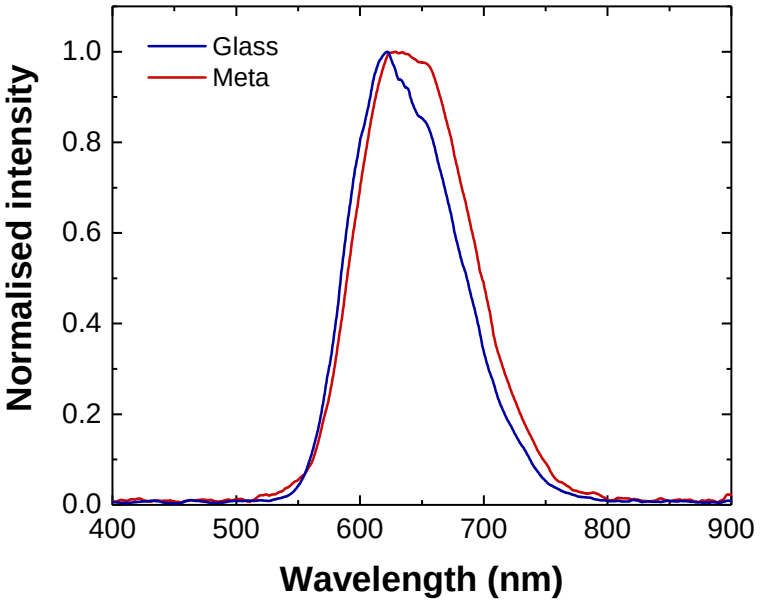

FIGURE 7.5: **Emission spectra of $Ru(dpp)_3Cl_2$ in water.** Emission spectra on a glass substrate (blue) and inside the nanorod-based metamaterial (red).

7.3.2 $Ru(dpp)_3Cl_2$ in glycerol

As mentioned above, this complex has shown to be an efficient oxygen sensor. In order to minimise the effect of oxygen in the lifetime measurements, the same experiments were also conducted in glycerol, which is much more viscous than water and therefore limits the dynamic quenching from molecular oxygen. Fluorescence spectroscopy was performed for the complex on glass and inside the metamaterial as shown in Figure 7.6, where again the emission spectrum inside the metamaterial exhibits a slight red-shift compared to the emitter on glass.

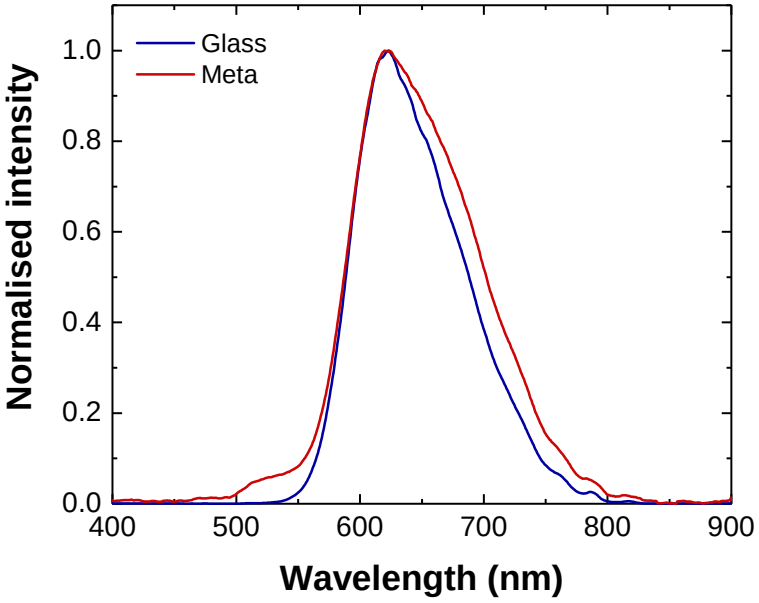

FIGURE 7.6: **Emission spectra of $Ru(dpp)_3Cl_2$ in glycerol** Emission spectra on a glass substrate (blue) and inside the nanorod-based metamaterial (red).

The results from the time-resolved analysis on different substrates can be observed in Figure 7.7a, where the complex exhibits a mono-exponential decay when deposited on glass and multi-exponential decays in the case of the gold film and the metamaterial. The corresponding lifetime distributions are depicted in Figure 7.7b. The lifetime distribution in the case of glass is centered around 4500 ns. An almost 1000-fold reduction of the lifetime is observed when the emitter is placed near the gold surface and a 2650-fold reduction in the case of the emitters inside the metamaterial.

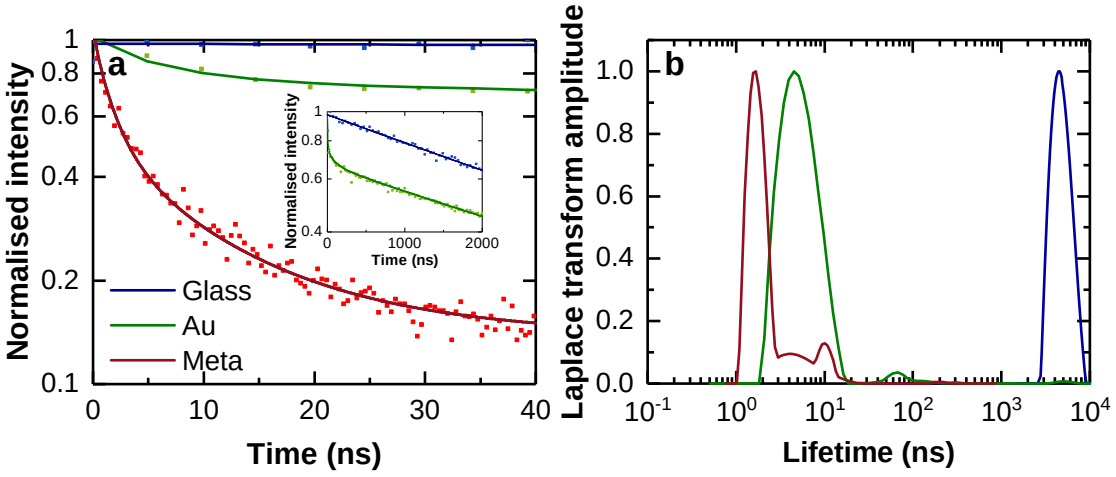

FIGURE 7.7: **Time-resolved analysis of $Ru(dpp)_3Cl_2$ in glycerol.** **(a)** Emission dynamics and **(b)** lifetime distributions for the emitters on a glass substrate (blue), on a 50 *nm* thick gold film (green) and inside the nanorod-based metamaterial (red). In (a), the dotted lines represent the experimental measurement and the solid lines are the fit performed using the inverse Laplace transform method.

In this case also, a theoretical prediction of the distribution on the gold film was obtained from the experimental distribution on glass for different depths of focus, as represented in 7.8. The same conclusion as for the complex in water can be observed and confirm the inapplicability of the method for phosphorescence measurements.

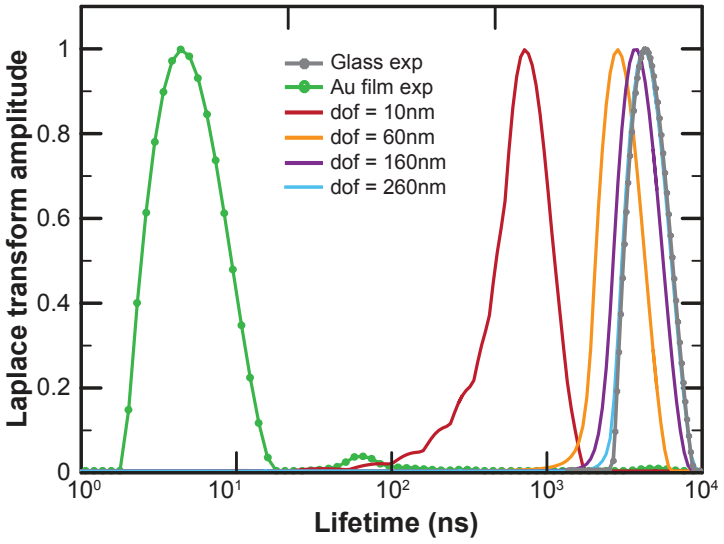

FIGURE 7.8: **Theoretical lifetime distributions above the smooth gold surface recalculated from the measured lifetime distributions of the complex in water deposited on glass for different depth of focus (dof).** Lines with symbols are experimental data measured on glass and above the gold film, lines only are the theoretical estimations.

7.4 Conclusion

In this experimental study, a very large enhancement of the spontaneous emission lifetime of a Ruthenium-based complex has been demonstrated in various plasmonic environments including a nanorod-based hyperbolic metamaterial, for which the enhancement factor reached a factor of almost 3000. In this context, the modification of the spontaneous lifetime of the complex could not be predicted by the standard electromagnetic local density of states description, employed for the analysis of fluorescent dyes. This could potentially be attributed to the specific nature of the transitions involved in the emission process. From an application point of view, the large range of spontaneous emission lifetimes available enables the development of novel fast and efficient light-emitting sources.

Chapter 8

Förster Resonance Energy Transfer inside a gold nanorod-based hyperbolic metamaterial

Förster resonance energy transfer is a powerful tool used in various domains ranging from bioapplications, in order to measure distances between two fluorescent emitters at the nanoscale, to organic photovoltaics and light-emitting devices. However, FRET is limited to ranges up to 10 nm due to a dependence on the distance between donor and acceptor to the sixth power, and enhancing the energy transfer would allow to extend the possibilities of FRET. As shown in the previous chapters, the engineering of the LDOS in the vicinity of emitters using nanostructured environments with appropriate electromagnetic properties has been shown to greatly enhance their spontaneous emission properties. Hence, the possibility of using these engineered environments to control the energy transfer between emitters has recently gained a lot of interest.

As described in Chapter 3, experimental studies on energy transfer in different material environments with engineered LDOS have led to controversial results. Therefore, the question of the dependence of the energy transfer on the modification of the LDOS remains open. As well as experimental studies, several theoretical studies generally based on the

calculation of Green functions have been performed. A linear dependence of the energy transfer rate on the donor emission dynamics, suggested in several experiments, was also supported by a theoretical work by Dung *et al.* [230], while a quadratic dependence on the LDOS was experimentally shown and modelled by Nakamura in [176, 177]. Several other theoretical developments also demonstrated that Förster energy transfer rates were independent of the modification of the LDOS [180, 183, 231] but highly dependent on the positioning of the donor-acceptor pairs with regard to the material environment.

In this chapter, the energy transfer between a donor-acceptor pair on double stranded DNA linkers located in different plasmonic environments was investigated. While a gold film provides only a moderate enhancement of the LDOS, emitters placed inside a gold nanorod-based hyperbolic metamaterial experience a high enhancement of the LDOS, leading up to a 13-fold increase of the FRET rate. The FRET efficiencies as well as the free-space emission intensities of the acceptor have also been studied.

8.1 Donor-acceptor pair

8.1.1 Molecules

For this study, donor-acceptor pairs are constituted of ATTO 550 and ATTO 647N molecules. Table 8.1 shows a few properties such as absorption and emission peak wavelengths as well as the quantum yield of these two dyes. These dyes typically exhibit strong absorption, high fluorescence quantum yield and high photostability. As presented in Figure 8.1, the normalised emission spectrum of the donor and the normalised absorption spectrum of the acceptor show a spectral overlap which is one of the key condition for FRET to be able to occur. The Förster radius, R_0, for these two molecules in pure water is equal to 6.5 nm.

TABLE 8.1: Properties of ATTO dyes

	ATTO 550	ATTO 647N
Absorption peak (nm)	554	646
Emission peak (nm)	576	664
Quantum yield (%)	80	65

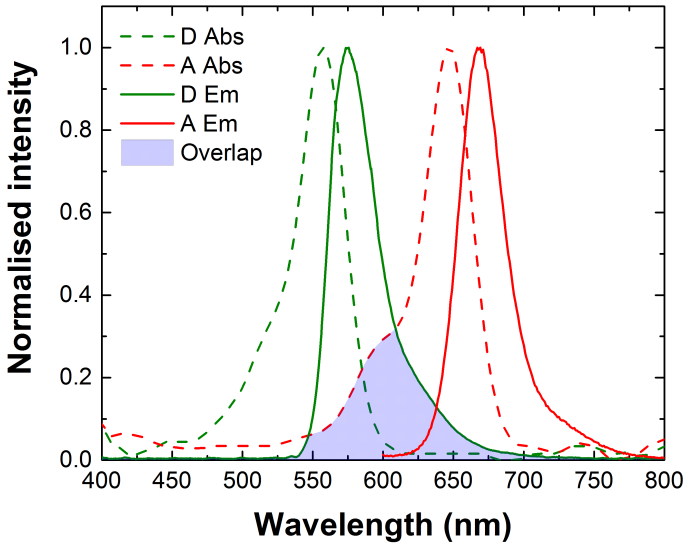

FIGURE 8.1: **Absorption (dashed lines) and emission (solid lines) spectra of ATTO 550 and ATTO 647N dyes.** The blue shaded area represents the spectral overlap between the emission of the donor (ATTO 550) and the absorption of the acceptor (ATTO 647N).

8.1.2 Hybridisation

In order to control the separation between donor and acceptor, the emitters are attached to complementary single-stranded DNA oligonucleotides of known lengths and then hybridised. Three different lengths of DNA strands were used: 10, 20 and 30 base pairs respectively corresponding to 3.4 nm, 6.8 nm and 10.2 nm, providing three different FRET efficiencies. Table 8.2 shows the modified complementary DNA sequences.

TABLE 8.2: Properties of oligonucleotides

Name	**Sequence** $(5' \rightarrow 3')$	**Modification**
Donor 30	GTGATCGCAGCAAACGTCGGCTTCCAGGAC	$5' - ATTO550$
Acceptor 30	GTCCTGGAAGCCGACGTTTGCTGCGATCAC	$5' - ATTO647$
Donor 20	GTGATCGCAGCAAACGTCGG	$5' - ATTO550$
Acceptor 20	CCGACGTTTGCTGCGATCAC	$5' - ATTO647$
Donor 10	GTGATCGCAG	$5' - ATTO550$
Acceptor 10	CTGCGATCAC	$5' - ATTO647$

Prior to hybridisation, the complementary oligonucleotides were resuspended at the same molar concentration (100 $\mu mol.L^{-1}$) in an annealing buffer composed of 10 $mmol.L^{-1}$ Tris-HCL, 1 $mmol.L^{-1}$ EDTA and 30 $mmol.L^{-1}$ NaCl. The pH of the solution was then

adjusted to 7.85 with NaOH. Equal volumes of both complementary strands were then mixed and heated at $90°C$ for 5 minutes and cooled to room temperature for an hour.

8.1.3 Polyacrylamide gel electrophoresis

A gel electrophoresis [232], allowing the separation of the DNA fragments based on their sizes, was performed to verify the hydridisation of the modified single DNA strands. The type of polymer and the concentration used for the gel are typically chosen with regard to the length of the DNA strands to resolve. Higher gel concentrations result in a larger polymer to water ratio and thus smaller pores. In order to separate short fragments of DNA, typically in the range of 1 to 500 base pairs, a 20 % polyacrylamide gel was chosen in this study. A dense loading buffer containing a tracking dye (BlueJuice^{TM}gel loading buffer, Invitrogen) was then added to the samples and to a DNA ladder in order to ease the loading of the samples into the wells and to make the DNA fragments visible in the gel. A DNA ladder contains fragments of DNA of known lengths that can be run at the same time as the samples for reference.

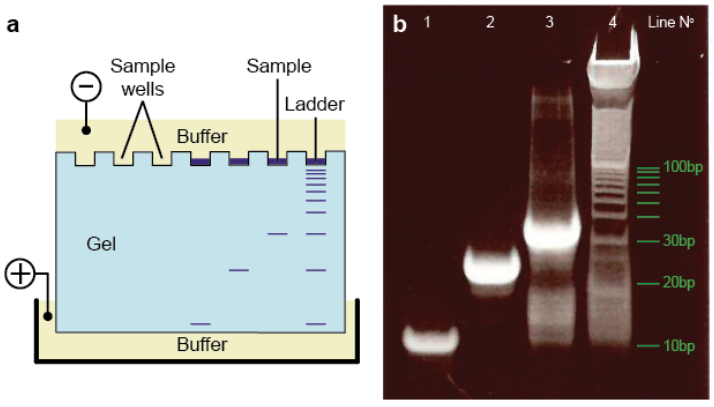

FIGURE 8.2: **Polyacrylamide gel electrophoresis. a.** Schematic of gel electrophoresis setup, **b.** Result of polyacrylamide gel electrophoresis for the double stranded DNA fragments.

To perform the electrophoresis, the gel was mounted in a gel-casting chamber. The top and bottom of the gel were immersed in a conductive buffer respectively containing a cathode and an anode. By applying an electric field through the porous gel (150 V for 75 minutes), the negatively charged DNA strands loaded in small wells at the top of the gel were pulled towards the positive electrode as shown in Figure 8.2a. The velocity of migration of the fragments being inversely proportional to their lengths, the separation of

the sample's constituents led to distinct bands that could be compared to the bands of the DNA ladder. The gel was finally disassembled, rinsed and stained with a dye which binds to DNA (SYBR® gold) in order to be revealed under UV light.

Figure 8.2b shows the result of the gel electrophoresis after revelation. Line $N°1, 2, 3$ and 4 respectively contained the 10, 20 and 30 base pairs DNA samples and the DNA ladder (10 bp DNA Ladder, Invitrogen). As predicted, the shorter DNA strands migrated quicker than the longer ones through the gel and therefore covered longer distances. By comparing the bands of the DNA ladder to the samples, the correct lengths (10 bp, 20 bp and 30 bp) of the DNA samples were observed. Despite the quite clear result shown by the gel electrophoresis on the hybridization of the complementary DNA strands, the quality of the bands obtained was not optimal. The presence of diffused bands and "smiling" of the bands could have been the result of an inhomogeneous heat buildup in the gel or an excess of DNA [233].

8.2 Samples

In this experimental study, five different environments were considered in order to investigate the dependence of the LDOS on the energy transfer between the donor and the acceptor: a glass coverslip was used as a reference sample while a gold thin film (50 nm thickness) and a gold nanorod-based metamaterial with and without its AAO template, allowing the donor-acceptor pairs to be located inside and on top of the metamaterial were considered. A free-standing polymer coated gold nanorod-based metamaterial was also investigated to limit quenching of the emission intensity for donor-acceptor pairs located close to each individual nanorod. Figure 8.3 depicts the different environments used.

8.2.1 Nanorod metamaterial

The nanorod-based metamaterials were fabricated by gold electrodeposition into a highly ordered nanoporous AAO templates on glass coverslips following the method described in Chapter 4. The geometrical parameters of the nanorod arrays used in the following experiments are 48 nm diameter, 100 nm period and 250 nm height. The AAO template of the sample was subsequently dissolved in order to obtain free-standing nanorods. Figure

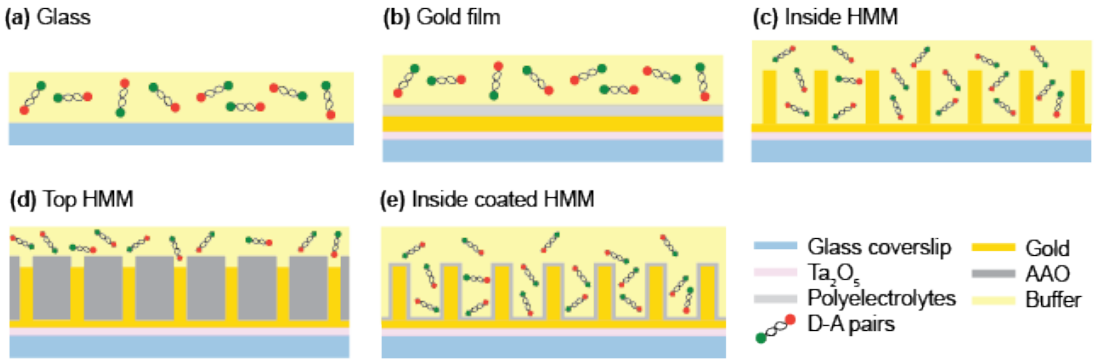

FIGURE 8.3: **Samples used for FRET study. (a)** Donor-acceptor pairs on glass, **(b)** on a 50 *nm* thick gold film, **(c)** inside the free-standing gold nanorod-based metamaterial, **(d)** on top of the gold nanorod-based metamaterial and **(e)** inside the polymer coated gold nanorod-based metamaterial.

8.4(a) depicts a SEM image of the gold nanorod-based metamaterial sample used in the following experiments and Figure 8.4(b, c) shows the optical properties of this sample in air and in water, respectively.

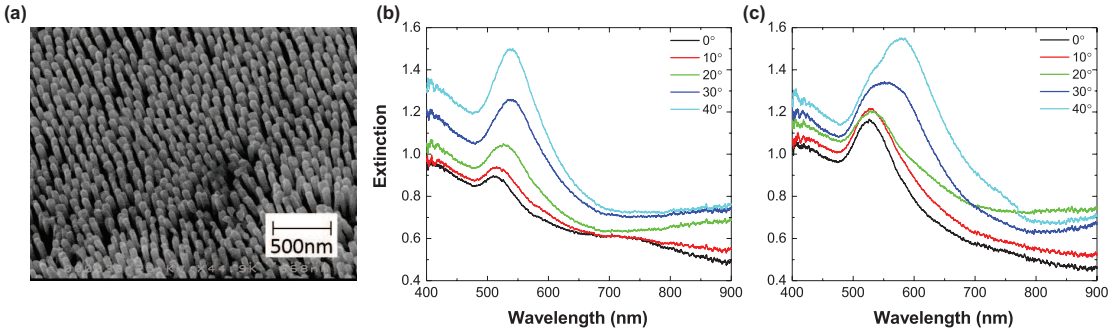

FIGURE 8.4: **Free-standing gold nanorod-based hyperbolic metamaterial. (a)** SEM image of the sample tilted at 45^o, **(b,c)** Experimental extinction spectra ($-log(Transmission)$) of the free-standing gold nanorod-based metamaterial in (a) air and (b) water for different angles of incidence of TM-polarised light.

An additional sample with the same geometrical parameters was then fabricated in order to study the energy transfer for donor-acceptor pairs located on top of the metamaterial. Due to the fabrication process, a layer of porous AAO remained on top of the gold nanorods as depicted in Figure 8.3d. Ideally, this top layer of AAO could be milled in order to obtain a flat top surface. Figure 8.5 shows the experimental extinction spectra of this sample for different angles of incidence of TM-polarised light.

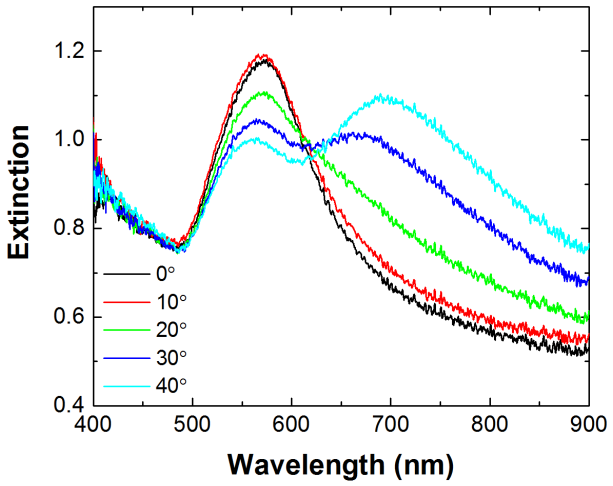

FIGURE 8.5: **Experimental extinction spectra ($-log(Transmission)$) of the gold nanorod-based metamaterial in its AAO matrix from Figure 8.3d.** Spectra were measured for different angles of incidence of TM-polarised light.

8.2.2 Polymer coated nanorod metamaterial

In order to coat the gold nanorod-based metamaterial with a thin layer of polymer, a new sample was used. The diameter of the nanorods was estimated at 57 nm, their length at 153 nm and their period at 102 nm. The coating of the gold nanorod sample with a thin layer of polymer to prevent quenching was performed using a layer-by-layer deposition technique. Each polyelectrolyte layer was prepared by alternating the deposition of poly(allylamine hydrochloride) (PAH) and polystyrene sulfonate (PSS). For each deposition step, the plasmonic gold nanorod metamaterial was immersed in a polyelectrolyte solution (10 $mg.mL^{-1}$ in 1 $mmol.L^{-1}$ NaCl aqueous solution) for 30 minutes and washed thoroughly with pure water (18 $M\Omega$). Figure 8.6b shows a SEM image of the sample after coating.

The layer-by-layer process was initiated with the cationic PAH layer in order to facilitate the attachment of the first polyelectrolyte layer to the gold nanorods through amine-gold interactions and terminated with the PSS layer to facilitate the electrostatic immobilisation of the dye molecules to the spacer layer. The thickness of the deposited polymer layer was measured by TEM on a sacrificial sample. The nanorod were pulled off the substrate by sonication and subsequently covered with gold nanoparticles in order to visualise the gap between the nanorods and the gold nanoparticles. The sample used in the following experiments was prepared in order to achieve a 7.5 nm spacing layer. Figure 8.6a depicts

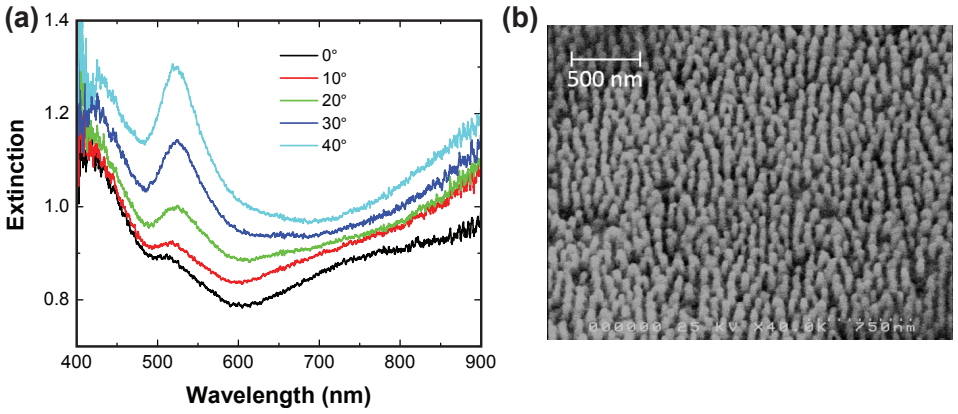

FIGURE 8.6: **Experimental extinction spectra ($-log(Transmission)$) of the polymer coated free-standing gold nanorod-based metamaterial from Figure 8.3e and SEM image. (a)** Experimental extinction spectra measured for different angles of incidence of TM-polarised light in air, **(b)** SEM image of the sample tilted at 45^o.

the extinction spectra of the coated nanorod sample for different angles of incidence for TM-polarised light.

8.3 Experimental results

For all measurements, the solution of donor-acceptor pairs was diluted to a concentration of 1 $\mu mol.L^{-1}$. The substrates were then placed on a confocal microscope and 1 μL of the solution was subsequently drop-casted onto the samples. The same metamaterial sample was used for each set of measurement comprising acquisitions for the three different lengths of donor-acceptor pairs and both the donor and the acceptor alone. Photoluminescence spectroscopy and time-resolved analysis were performed using the experimental setup described in Chapter 4. A 532 nm wavelength laser beam, focused on the samples with a 100× immersion oil objective ($NA = 1.49$), was used to excite the donor. The fluorescence signal was detected through the same objective. Appropriate dichroic mirrors and band-pass filters were used to separate the fluorescence signal from the excitation light.

8.3.1 Time-resolved photoluminescence and Laplace transform analysis

The FRET rate modification together with the LDOS enhancement in the different environments were evaluated by recording the decay dynamics of the donor for different

donor-acceptor lengths using a TCSPC technique. The emission decays were then analysed using the inverse Laplace transform described in Chapter 4.

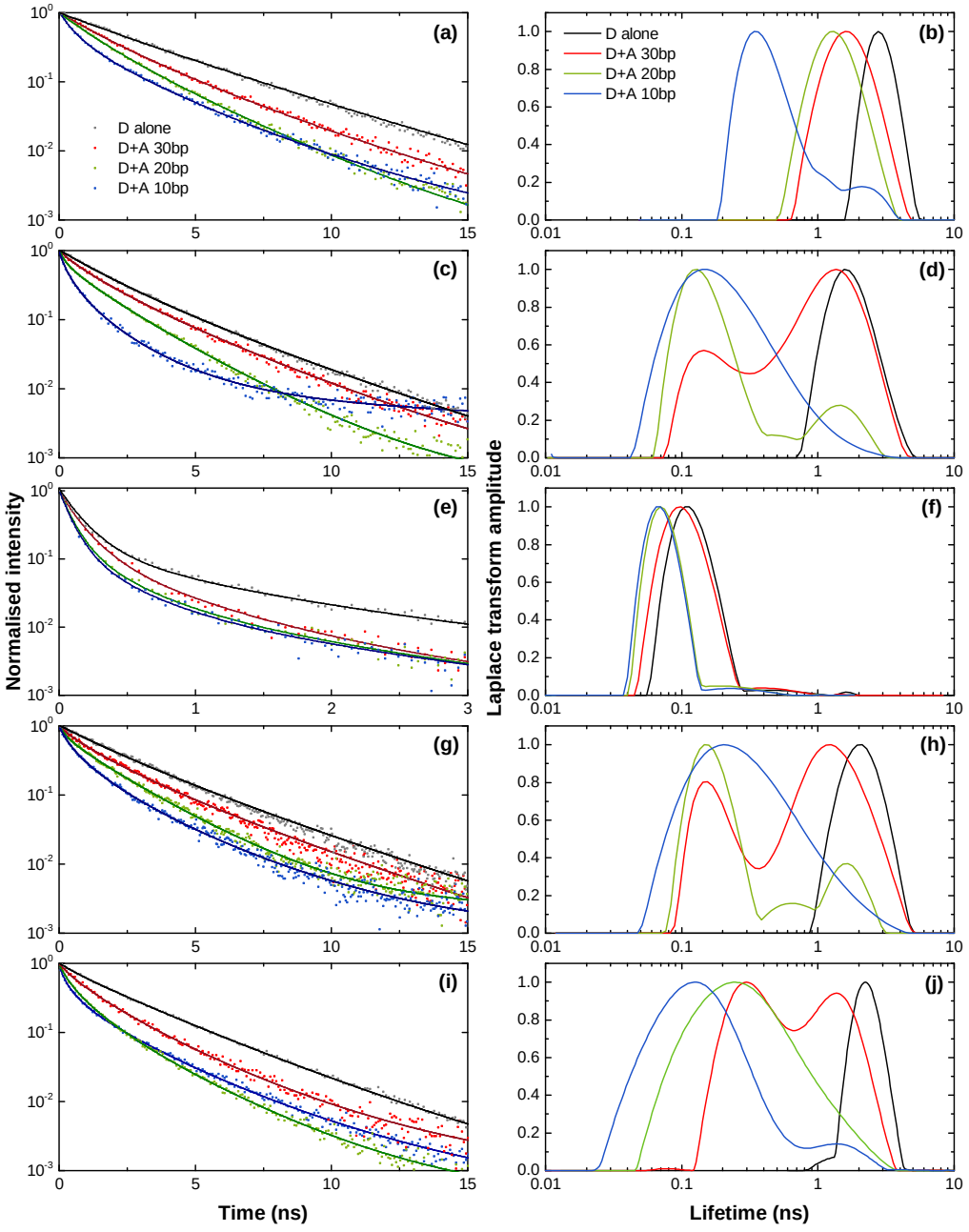

FIGURE 8.7: **Normalised decay dynamics of the donor for different donor-acceptor separations in different environments and Laplace analysis. (a, b)** On glass, **(c,d)** on a 50 *nm* thick gold film, **(e, f)** inside the gold nanorod-based metamaterial, **(g, h)** on top of the gold nanorod-based metamaterial, **(i, j)** inside the polymer coated gold nanorod-based metamaterial.

Figure 8.7(a,c,e,g,i) reports the normalised decay curves for the various environments, where the energy transfer is exhibited by the reduction of the donor's lifetime as much

as the separations between the donor and the acceptor is reduced. In the case of the donor alone, the lifetime of the donor is decreased by the presence of the gold film and the metamaterial, corresponding to an increase in the decay rate of the donor $\Gamma_D = 1/\tau_D$ and revealing the modification of the LDOS for each environment. The energy transfer between the donor and the acceptor is evidenced by the further reduction of the donor's lifetime in the presence of the acceptor $\tau_{DA} = 1/\Gamma_{DA}$ for each donor-acceptor separations, due to the additional decay channel provided by the enabled energy transfer between the donor and the acceptor. The decay rate of the donor can therefore be expressed as a function of the decay rate of the donor alone Γ_D and the energy transfer rate Γ_{FRET} leading to $\Gamma_{DA} = \Gamma_D + \Gamma_{FRET}$.

By looking at the lifetime decays in the different environments depicted in Figure 8.7(a,c,e,g,i), it is seen that whereas the lifetimes for all donor-acceptor separations on the glass substrate, the gold film, on top of the metamaterial and inside the polymer coated metamaterial are moderately modified, the lifetimes in the case of the donor-acceptor pairs inside the uncoated metamaterial are strongly reduced, reaching a few hundreds of picoseconds. The broad features exhibited by the lifetime distributions in Figure 8.7(b,d,f,h,j) and therefore the multi-exponential profiles of the decay dynamics are mainly related to the random positions of the donor-acceptor pairs as well as the random orientations of their dipole moments.

8.3.2 FRET decay rates and efficiencies

Using the distributions obtained by analysis of the emission dynamics of the donor via inverse Laplace transform approach, an amplitude average lifetime was calculated using the following formula [234]:

$$\langle \tau \rangle = \sum_{i=1}^{n} \frac{\alpha_i}{\sum_{i=1}^{n} \alpha_i} \tau_i \tag{8.1}$$

where n is the number of time steps in the lifetime distribution, τ_i is the lifetime component of the donor and $\frac{\alpha_i}{\sum_{i=1}^{n} \alpha_i}$ its corresponding amplitude. Figure 8.8 gathers the results obtained. The donor alone on a glass substrate shows an average lifetime of about 3.2 ns which is consistent with the value reported in the literature.

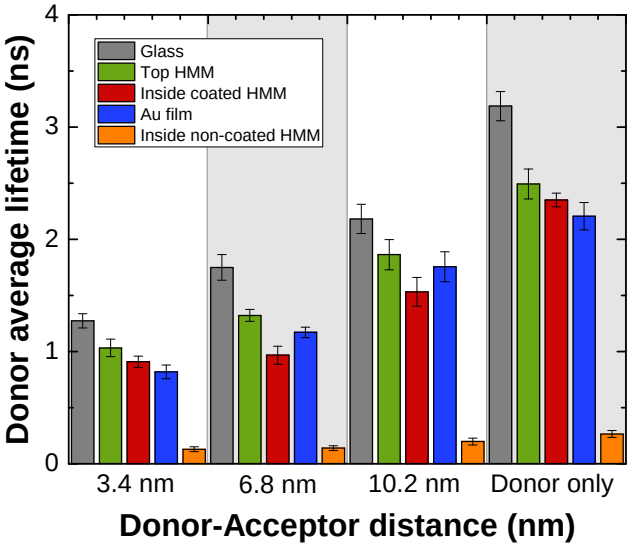

FIGURE 8.8: **Average lifetime of the donor in different electromagnetic environments as a function of the donor-acceptor separation.** The error bars have been calculated from the lifetime distributions, using error propagation on the calculated average lifetime.

From these average lifetimes, the rate of energy transfer Γ_{FRET} and FRET efficiencies E_{FRET} were calculated using the following equations

$$\Gamma_{FRET} = \Gamma_{DA} - \Gamma_D = \frac{1}{\tau_{DA}} - \frac{1}{\tau_D} \tag{8.2a}$$

$$E_{FRET} = 1 - \frac{\Gamma_D}{\Gamma_{DA}} = 1 - \frac{\tau_{DA}}{\tau_D} \tag{8.2b}$$

In order to evaluate the influence of the LDOS on the energy transfer, the FRET rates and efficiencies have been represented as a function of the decay rate of the donor alone in different environments, representing the modification of the LDOS. As represented in Figure 8.9, the increase in the LDOS from the glass substrate to the the top of the metamaterial or the gold film is moderate, with rates increasing from 0.31 ns^{-1} to respectively 0.40 ns^{-1} and 0.45 ns^{-1} and leading to enhancements of respectively 1.3-fold and 1.5-fold. The same observation has been made in the case of the polymer coated nanorod-based metamaterial, where the decay rate of the donor is equal to 0.42 ns^{-1} (1.35-fold enhancement). In the case of the donor-acceptor pairs located inside the metamaterial, the increase is more significant, with an increase of the decay rate of the donor from 0.31 ns^{-1} to 3.76 ns^{-1}

or a LDOS enhancement of 12.1-fold. For larger separations between the donor and the acceptor (6.8 nm and 10.2 nm), an increase in the LDOS led to an increase of the FRET rate, reaching up to an 13-fold increase the donor-acceptor pairs located inside the metamaterial compared to glass. For short separations, i.e 3.4 nm, the modification of the FRET rate does not have a well-defined trend. As the spread in the LDOS studied is not gradual and a significant gap exists between the LDOS enhancement on the gold film and inside the metamaterial, the relationship between the LDOS and the FRET rate is difficult to determine. The non-trivial behaviour of the FRET characteristics in the complex environments studied could be related to various factors. The study of an ensemble of donor-acceptor pairs rather than single pairs could potentially lead to collective effects or cross-talk between FRET pairs, which may play an important role in the energy transfer process, as described in several studies [183, 185]. Other factors such as inaccurate pairing of the donor-acceptor pairs, leading to different distances between donors and acceptors could also influence the experimental results. Moreover, due to the strong dependence of the emission dynamics on the positioning of the donor-acceptor pairs in its environment, a precisely controlled electromagnetic environment, as well as an homogeneous distribution of emitters, is required.

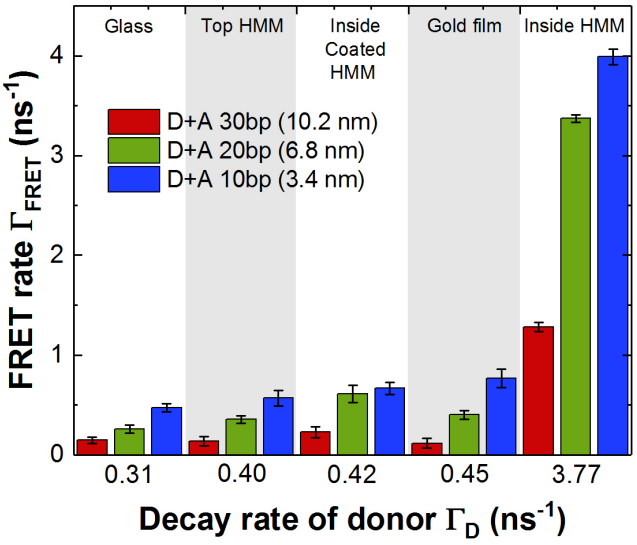

FIGURE 8.9: **FRET rates for different donor-acceptor separation in different electromagnetic environments as a function of the increase in LDOS.** The error bars have been calculated via the propagation of errors method from the errors on the average lifetimes.

Using the same donor decay dynamics and Equation 8.2b, FRET efficiencies have been calculated for the three separations between the donor and the acceptor in each environments. In the case of the donor-acceptor molecules on glass, it is possible to compare the obtained efficiencies to the theoretical values calculated from the known Förster radius R_0 for this specific pair of donor-acceptor, for which a separation of $R_0 = 6.5\ nm$ leads to a 50 % FRET efficiency.

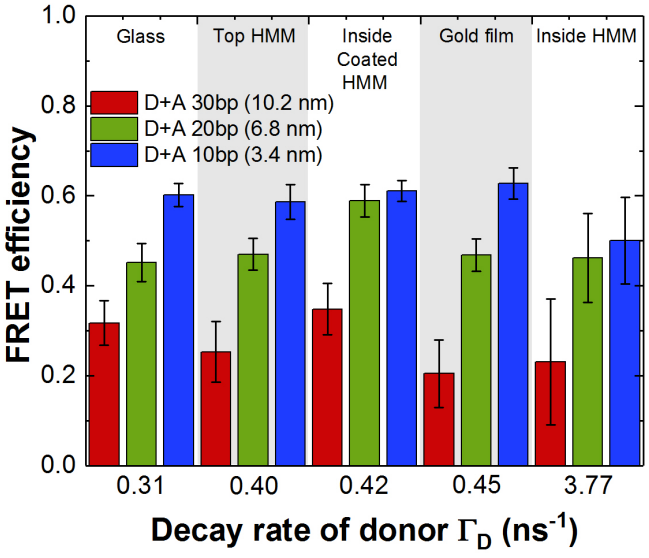

FIGURE 8.10: **FRET efficiencies for different donor-acceptor separation in different electromagnetic environments as a function of the increase in LDOS.** The error bars have been calculated via the propagation of errors method from the errors on the average lifetimes.

As observed from Figure 8.10, a separation of 6.4 nm (20 base pairs) between the donor and the acceptor led to a measured 47 % FRET efficiency on glass which is in reasonable agreement with the theoretical value (51 %). However, the experimental value of ≈ 60 % for a donor-acceptor separation of 3.4 nm is much lower than the theoretical value of 98 %, whereas in the case of a 10.2 nm separation, the experimental value of ≈ 30 % is higher than the theoretical one of 6 %. These discrepancies between experimental and theoretical values of efficiencies can be related to the presence of DNA linkers between the donor and acceptor, preventing dynamic random averaging of the molecules and therefore altering the efficiency of the energy transfer. In this case, the assumed value of $\kappa^2 = 2/3$ is no longer valid and the theoretical determination of κ^2, specific to each type of donor-acceptor pair and their separation, requires the study of the molecular binding of the system [235–237].

The analysis of the FRET efficiencies for each electromagnetic environments has revealed only slight variations of the FRET efficiency with the increase in the LDOS in most cases. The most significant increase in FRET efficiency has been observed in the case of the polymer coated gold nanorod-based metamaterial for all donor-acceptor separations. Small variations of the efficiency are consistent with an increase of the FRET rate as increasing the donor decay rate for each environment and keeping the efficiency the same requires the FRET rate to increase in consequence as $E_{FRET} = \frac{\Gamma_{FRET}}{\Gamma_{FRET}+\Gamma_D}$. However, a decrease in the FRET efficiency essentially means that the donor's decay rate in the absence of the acceptor increases more than the FRET rate in the same environment. This study of FRET through time-resolved analysis of the emission dynamics of the donor has revealed no significant trend on the influence of the material environment on the FRET efficiency but has shown a large increase of the FRET rate, especially inside the metamaterial.

8.3.3 Photoluminescence spectroscopy

The free-space emission intensity of the acceptor collected through the substrate was recorded and normalised to the emission intensity of the donor. The direct emission intensity of the acceptor at the excitation wavelength of the donor was subtracted beforehand. Figure 8.11 depicts the results obtained where the energy transfer generally manifests itself by the increase of the acceptor emission intensity for shorter separations between the donor and the acceptor.

With regard to the donor-acceptor pairs placed on glass, the acceptor emission intensities in the case of the gold film and on top of the metamaterial are both increased whereas in the case of molecules inside the metamaterial, the emission intensity is greatly reduced for all lengths. According to the study reported in Chapter 6, the reduced free-space emission of the acceptor could be due to the coupling of the emitted light to the waveguided mode supported by the structure. In order to verify this hypothesis, a dispersion of reflection for TM-polarised waves was modelled using an effective medium theory for the metamaterial parameters mentioned above and water as the embedding medium of the nanorods, matching the solvent used in the experiments.

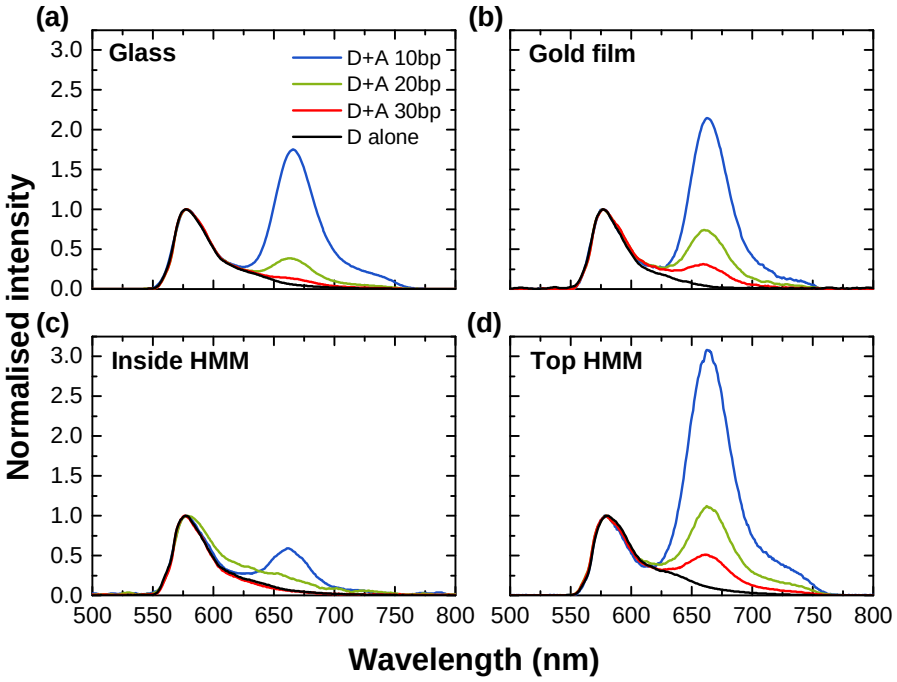

FIGURE 8.11: **Free-space donor-acceptor emission intensity for different donor-acceptor separations in different environments.** **(a)** On glass, **(b)** on a 50 *nm* thick gold film, **(c)** inside the gold nanorod-based metamaterial, **(d)** on top of the gold nanorod-based metamaterial. The data have been normalised to the emission intensity of the donor.

Figure 8.12 shows that one of the TM-polarised waveguided modes supported by the structure is significantly overlapping with the emission of the acceptor, thus favouring the coupling of the emitted light by the acceptor to this mode.

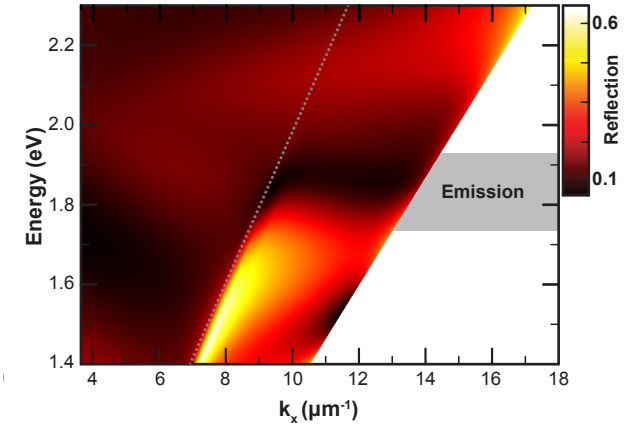

FIGURE 8.12: **Reflection dispersion of the metamaterial for TM polarisation from EMT modelling using a Transfer Matrix Method.** The embedding material surrounding the nanorods is water. The light line in air (grey dotted line) and the emission band of the acceptor dye (greyed region) are represented.

Photoluminescence measurements were then performed on the polymer coated free-standing gold nanorod-based metamaterial as shown in Figure 8.13. It is shown that the free-space intensity of the acceptor is largely enhanced for all donor-acceptor separations but mostly for larger distances (6.8 nm and 10.2 nm).

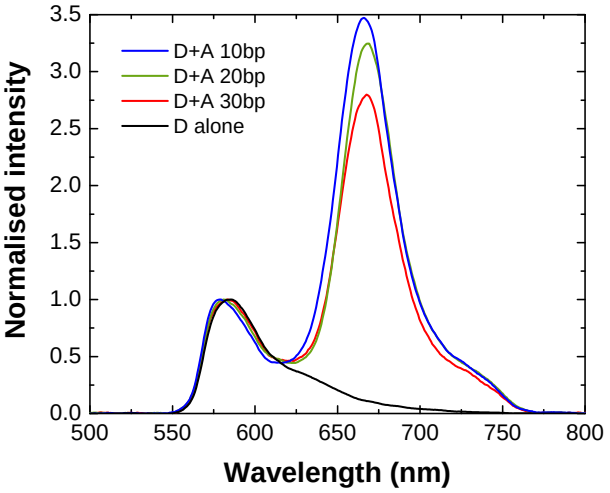

FIGURE 8.13: **Free-space donor-acceptor emission intensity for the free-standing polymer coated gold nanorod-based metamaterial.** The data have been normalised to the emission intensity of the donor.

The presence of the coating around the nanorods acts as a spacer between the metal and the dye molecules in order to avoid quenching but is also modifying the optical properties of the material, thus altering its mode structure. This is therefore affecting the position of the waveguided modes of the metamaterial and in this case does not prevent the free-space emission of the acceptor.

8.4 Conclusion

The energy transfer between a donor and an acceptor with precise separations and located in different electromagnetic environments has been investigated in this chapter. In most environments with increased LDOS, an increase in the donor's spontaneous emission rate as well as the FRET rate with regard to the rates of emitters placed on glass has been observed. In particular, donor-acceptor pairs placed inside the gold nanorod-based metamaterial, showing a 12-fold increase of the LDOS, exhibited a 13-fold increase of the FRET rate along with only slight variations of the FRET efficiency compared to the

emitters located on glass. The free-space intensity measurements of the acceptor's emission for donor-acceptor pairs inside the metamaterial also revealed a strong decrease in the acceptor's emission attributed to the coupling of the emission to the waveguided mode supported by the system at the emission wavelength of the acceptor. For the emitters located on top of a gold film, on top of the nanorod-based metamaterial in its AAO matrix or inside the polymer coated metamaterial, the increases in the decay rates of the donor or the FRET rates remained moderate and the free-space emission of the acceptor normalised to the donor's emission increased in all cases compared to the emission intensity on glass. The highest increase in intensity has been observed in the case of the polymer coated metamaterial, especially for larger separations between the donor and acceptor. The coating of the nanorod-based metamaterial with a thin polymer shell has shown to be a good solution to avoid quenching but also strongly reduces the decay rates compared to the emitters located inside the uncoated metamaterial. The homogeneity of the coating still remains a challenge and needs to be improved for future experiments. This could potentially be achieved by functionalising the gold nanorods with thiols of fixed lengths in order to avoid multi-steps deposition processes. These results show the potential of highly tunable hyperbolic metamaterial for the control of the energy transfer between emitters and the design of fast light-emitting devices.

Chapter 9

Conclusions and Outlook

9.1 Summary

This thesis described the process of spontaneous emission of fluorescent and phosphorescent emitters as well as non-radiative energy transfer in donor-acceptor emitter pairs placed in engineered material environments. In particular, the influence of a gold nanorod-based hyperbolic metamaterial on these processes has been explored. The inexpensive and relatively easy fabrication process of these metamaterials using a self-assembled approach, combined with the ability to tune their geometrical parameters, allows their electromagnetic properties to be tailored in a wide spectral range and over large areas. Therefore, plasmonic hyperbolic metamaterials have recently emerged as a very flexible and powerful platform for spontaneous emission engineering due to their peculiar mode structure providing high density of optical states as well as broadband enhancement.

The study of spontaneous emission in non-local materials was performed. While the linear optical properties of the nanorod-based hyperbolic metamaterial investigated in experiments can be affected by a non-local response of the composite, it was shown theoretically, numerically and experimentally that these properties dominate the spontaneous emission process in such materials, due to the presence of an additional electromagnetic mode impacting the density of optical states available for the emitter to decay. Experimental enhancement of the spontaneous emission rate has been observed, which is in agreement with the theoretical description of the Purcell effect in non-local materials developed.

The influence of the mode structure of the nanorod-based hyperbolic metamaterial on the spontaneous emission of emitters embedded within the metamaterial planar waveguide has been demonstrated. The enhancement of the fluorescence coupled to the waveguided plasmon-polariton modes of the metamaterial has been shown. A strong position-dependent acceleration of the spontaneous decay rate has been observed for emitters inside the metamaterial slab, while only a weak modification of the rate was observed for emitters in the proximity of the metamaterial waveguide interface.

The process of phosphorescence using a long lifetime Ruthenium-based complex, involving triplet-state electronic transitions, was performed in different electromagnetic environments. Very large increases in the spontaneous emission rate in the proximity of a metallic surface and inside a nanorod-based metamaterial were experimentally measured. In both cases, the enhancement factors obtained have been shown to be far beyond the predictions of the standard electromagnetic local density of states description, which led to a good agreement between theoretical and experimental approaches in the case of conventional fluorescent dyes.

The process of non-radiative energy transfer between donor and acceptor emitters in various plasmonic environments including a nanorod-based hyperbolic metamaterial was investigated. The emission dynamics of the donor and the free-space emission intensity of the acceptor were measured in order to evaluate the influence of the modification of the LDOS on the energy transfer process. The highest increase in the FRET rate was observed for emitters located within the metamaterial.

9.2 Outlook

The work reported in the scope of this thesis has given insight into the field of spontaneous emission engineering with hyperbolic metamaterials. The results have demonstrated the capability of such active hyperbolic metamaterials, exhibiting highly tuneable electromagnetic properties, to be used in many different types of practical applications ranging from bioapplications to quantum photonic applications, with the design of enhanced and fast light sources for various nanophotonic components. In addition, this work has opened up new potential research axes to be investigated. It has for instance been theoretically shown that finite-size resonators comprised of nanorod-based hyperbolic metamaterials exhibit

significant Purcell enhancement originating from the mode structure of the metamaterial. Therefore, as an extension to the experimental work done with the nanorod-based planar waveguide which has infinite dimensions in the plane perpendicular to the nanorods, the study of finite-size resonators based on nanorod hyperbolic metamaterials could be beneficial to the control of spontaneous emission. Moreover, in the case where free-space radiated emission is valuable, further nanostructuring of the nanorod-based metamaterial could be used as a way to optimise the out-coupling, shaping and directionality of the free-space emitted light. These tunable structures, potentially exhibiting high enhancements of emission intensity and spontaneous emission rates, would pave the way to the development of efficient light-emitting diodes or single photon sources.

Other types of hyperbolic metamaterials, such as metallo-dielectric multilayers, also constitute interesting alternatives for spontaneous emission engineering. Despite their more difficult fabrication process, requiring the careful combination of dielectric and metallic materials and the subsequent repetitive deposition of layers with deeply subwavelength thicknesses, multilayer hyperbolic metamaterials allow an easier control and optimisation of the placement of the emitters with regard to the structure, therefore limiting the quenching of emission by the metal.

The high potential of hyperbolic metamaterials for various practical applications has also recently led to the research towards natural hyperbolic materials [238, 239], having the advantage of not requiring expensive or complicated fabrication techniques. While many of the materials considered exhibit hyperbolic behaviour in the far-infrared spectral range, a few materials, including tetradymites such as Bi_2Se_3 and Bi_2Te_3, have been shown to exhibit broadband hyperbolic behaviour at optical frequencies [240]. Although having dedicated spectral ranges of applications, these natural hyperbolic materials have the advantage of exhibiting reduced unit cell sizes, technically allowing the presence of higher wavevector modes than in composite materials. These materials have however shown to be relatively lossy and reducing their absorption remains a challenge.

The highly attractive enhanced LDOS over a broad spectral range characteristic of 3D hyperbolic metamaterials has also recently been observed in 2D hyperbolic metasurfaces [241–243]. Thanks to their 2D character, metasurfaces have been predicted to show lower losses than their 3D equivalents and benefit from easy fabrication techniques as well as integration to optoelectronic circuits. These structures therefore constitute good

candidates for the control of spontaneous emission [244], by facilitating the placing of quantum emitters in the vicinity of the structure.

While the core of the research in spontaneous emission engineering has so far been performed in the visible spectral range thanks to the broad range of organic dyes and emitting nanoparticles available, the development of bioapplications, as well as new fields of interest based on spontaneous emission processes, have led to the need to extend the spectral range available. The near-infrared window, comprising wavelengths between 650 nm and 1700 nm, appears to be particularly attractive for biological applications because of minimum photodamage to samples and deep tissue penetration. This wavelength range is also of great interest for telecommunications applications, especially between 1300 nm and 1600 nm, where optical fibres exhibit zero-dispersion and lower losses. Therefore, research towards the design of nanostructured materials with engineered electromagnetic properties for the control of spontaneous emission and non-radiative processes in this new spectral range is required and could be enabled by the development of new types of hyperbolic media, together with advances in the manufacturing of novel emitters.

List of Publications

Journal articles

- Ginzburg, P., Roth, D. J., Nasir, M. E., Segovia, P., Krasavin, A. V., Levitt, J., Hirvonen, L. M., Wells, B., Suhling, K., Richards, D., Podolskiy, V. A. and Zayats, A. V., 2017. **Spontaneous emission in non-local materials**. *Light: Science & Applications, 6, 6, e16273.*

- Roth, D. J., Dickson, W., Murphy, A., Kéna-Cohen, S., Pollard, R., Wurtz, G. A., Richards, D. R., Maier, S. A. and Zayats, A. V., **Spontaneous emission inside a hyperbolic metamaterial waveguide**. *ACS Photonics, 4, 10, 2513-2521.*

- Roth, D. and Dieleman, F., 2016. **Highlights from Faraday Discussion 178: Nanoplasmonics**, London, UK, February 2015. *Chemical Communications, 52, 3, 436-442.*

- Roth, D. J., Nasir, M. E., Suhling, K., Zayats, A. V., **Förster Resonance Energy Transfer inside a gold nanorod-based hyperbolic metamaterial**. *Manuscript in preparation.*

- Roth, D. J., Ginzburg, P., Levitt, J., Nasir, M. E., Hirvonen, L. M., Suhling, K., Richards, D., Podolskiy, V. A. and Zayats, A. V., **Spontaneous emission enhancement of a long lifetime Ruthenium complex with metamaterials**. *Manuscript in preparation.*

Conference papers

- Roth, D., Wang, P., Nasir, M.E., Krasavin, A.V., Wells, B., Ginzburg, P., Richards, D.R., Podolskiy, V.A. and Zayats, A.V., **Accelerating spontaneous emission with Metamaterials**. Invited paper at 9^{th} *International Conference on Materials for Advanced Technologies* (Singapore, June 2017).

- Roth, D. J., Nasir, M.E., Krasavin, A.V., Ginzburg, P., Wells, B., Dickson, W., Suhling, K., Richards, D.R., Podolskiy, V.A. and Zayats, A.V., **Purcell effect in metamaterials**. Oral presentation at *London Plasmonics Forum* (London, June 2017).

- Podolskiy, V.A., Ginzburg, P., Roth, D., Krasavin, A., Wells, B. and Zayats, A.V., **Engineering Optical Density of States with Nonlocal Metamaterials**. Invited paper at *CLEO: QELS Fundamental Science* (San Jose, May 2017).

- Wang P., Roth, D.J., and Zayats A.V., **Active plasmonic multishells**. Oral presentation at 6^{th} *Conference on Advances in Optoelectronics and Micro/Nano-optics* (Nanjing, April 2017).

- Roth, D., Nasir, M.E., Krasavin, A.V., Ginzburg, P., Dickson, W., Le Marois, A., Suhling, K., Richards, D.R., Podolskiy, V.A. and Zayats, A.V., **Spontaneous emission and non-radiative processes inside a hyperbolic metamaterial**. Invited paper at *Active Photonic Materials VIII, SPIE Nanoscience+ Engineering* (San Diego, August 2016).

- Roth, D., Nasir, M.E., Dickson, W., Suhling, K., Ginzburg, P., Richards, D.R. and Zayats, A.V., **Spontaneous emission and non-radiative processes inside a hyperbolic metamaterial**. Invited paper at *Nanophotonics VI, SPIE Photonics Europe* (Brussels, April 2016).

- Roth, D., Nasir, M.E., Dickson, W. , Murphy, A. , Kéna-Cohen, S. , Pollard, R. , Suhling, K. , Ginzburg, P. , Richards, D. R. , Wurtz, G. A. , Maier, S. A. , Zayats, A. V., **Experimental studies of spontaneous emission and energy transfer inside a hyperbolic metamaterial**. Poster at *Nanolight 2016 Conference* (Benasque, March 2016).

Bibliography

[1] Vasilis Ntziachristos, Jorge Ripoll, and Ralph Weissleder. Would near-infrared fluorescence signals propagate through large human organs for clinical studies? *Optics letters*, 27(5): 333–335, 2002.

[2] Robert V Steele. The story of a new light source. *Nature photonics*, 1(1):25–26, 2007.

[3] Koichi Okamoto, Isamu Niki, Alexander Shvartser, Yukio Narukawa, Takashi Mukai, and Axel Scherer. Surface-plasmon-enhanced light emitters based on ingan quantum wells. *Nature materials*, 3(9):601–605, 2004.

[4] Gabriel Lozano, Davy J Louwers, Said RK Rodríguez, Shunsuke Murai, Olaf TA Jansen, Marc A Verschuuren, and Jaime Gómez Rivas. Plasmonics for solid-state lighting: enhanced excitation and directional emission of highly efficient light sources. *Light: Science & Applications*, 2(5):e66, 2013.

[5] Igor Aharonovich, Dirk Englund, and Milos Toth. Solid-state single-photon emitters. *Nature Photonics*, 10(10):631–641, 2016.

[6] Jon A Schuller, Edward S Barnard, Wenshan Cai, Young Chul Jun, Justin S White, and Mark L Brongersma. Plasmonics for extreme light concentration and manipulation. *Nature materials*, 9(3):193–204, 2010.

[7] Igor L Medintz, Aaron R Clapp, Hedi Mattoussi, Ellen R Goldman, Brent Fisher, and J Matthew Mauro. Self-assembled nanoscale biosensors based on quantum dot fret donors. *Nature materials*, 2(9):630–638, 2003.

[8] Daniel J Farrell and Nicholas J Ekins-Daukes. Photovoltaic technology: Relay dye boosts efficiency. *Nature Photonics*, 3(7):373–374, 2009.

[9] MA Baldo, ME Thompson, and SR Forrest. High-efficiency fluorescent organic light-emitting devices using a phosphorescent sensitizer. *Nature*, 403(6771):750–753, 2000.

[10] Ian D. Johnson and Michael W. Davidson for Olympus Microscopy Resource Center. Jablonski energy diagram, 2012. URL `http://www.olympusmicro.com/primer/java/jablonski/jabintro/`.

[11] J.R. Lakowicz. *Principles of Fluorescence Spectroscopy*. Principles of Fluorescence Spectroscopy. Springer, 2006. ISBN 9780387312781.

[12] Herman Brian, Centonze Frohlich Victoria E., Lakowicz Joseph R., Murphy Douglas B., Spring Kenneth R., and Davidson Michael W. Basic concepts in fluorescence, 2015. URL `https://micro.magnet.fsu.edu/primer/techniques/fluorescence/fluorescenceintro.html`.

[13] Bernard Valeur and Mário Nuno Berberan-Santos. *Molecular fluorescence: principles and applications*. John Wiley & Sons, 2012.

[14] Joseph R Lakowicz and Gregorio Weber. Quenching of fluorescence by oxygen. probe for structural fluctuations in macromolecules. *Biochemistry*, 12(21):4161–4170, 1973.

[15] William R Ware. Oxygen quenching of fluorescence in solution: an experimental study of the diffusion process. *The Journal of Physical Chemistry*, 66(3):455–458, 1962.

[16] Sherwin Lehrer. Solute perturbation of protein fluorescence. quenching of the tryptophyl fluorescence of model compounds and of lysozyme by iodide ion. *Biochemistry*, 10(17): 3254–3263, 1971.

[17] David L Dexter. A theory of sensitized luminescence in solids. *The Journal of Chemical Physics*, 21(5):836–850, 1953.

[18] Mitio Inokuti and Fumio Hirayama. Influence of energy transfer by the exchange mechanism on donor luminescence. *The journal of chemical physics*, 43(6):1978–1989, 1965.

[19] Lubert Stryer and Richard P Haugland. Energy transfer: a spectroscopic ruler. *Proceedings of the National Academy of Sciences*, 58(2):719–726, 1967.

[20] Max Born and Emil Wolf. *Principles of optics: electromagnetic theory of propagation, interference and diffraction of light*. Elsevier, 2013.

[21] Karthik Shankar, Xinjian Feng, and Craig A Grimes. Enhanced harvesting of red photons in nanowire solar cells: Evidence of resonance energy transfer. *Acs Nano*, 3(4):788–794, 2009.

[22] Ellen R Goldman, Igor L Medintz, Jessica L Whitley, Andrew Hayhurst, Aaron R Clapp, H Tetsuo Uyeda, Jeffrey R Deschamps, Michael E Lassman, and Hedi Mattoussi. A hybrid quantum dot-antibody fragment fluorescence resonance energy transfer-based tnt sensor. *Journal of the American Chemical Society*, 127(18):6744–6751, 2005.

[23] Th Förster. *Intermolecular energy transfer and fluorescence*. National Research Council of Canada, 1955.

[24] G Cario and J Franck. Über sensibilisierte fluoreszenz von gasen. *Zeitschrift für Physik A Hadrons and Nuclei*, 17(1):202–212, 1923.

[25] J Perrin and N Choucroun. Fluorescence sensibilisée en milieu liquide (transferts d'activation par induction moléculaire). *CR hebd Séances Acad Sci*, 189:1213–1216, 1929.

[26] Robert M Clegg. The history of fret. In *Reviews in Fluorescence 2006*, pages 1–45. Springer, 2006.

[27] BR Masters. Paths to förster's resonance energy transfer (fret) theory. *The European Physical Journal H*, 39(1):87–139, 2014.

[28] Robert M Clegg. Fluorescence resonance energy transfer. *Current opinion in biotechnology*, 6(1):103–110, 1995.

[29] Ammasi Periasamy and Richard Day. *Molecular imaging: FRET microscopy and spectroscopy*. Elsevier, 2011.

[30] N.W. Ashcroft and N.D. Mermin. *Solid state physics*. Science: Physics. Saunders College, 1976. ISBN 9780030493461.

[31] Mark Fox. Optical properties of solids, 2002.

[32] Stefan Alexander Maier. *Plasmonics: Fundamentals and Applications: Fundamentals and Applications*. Springer, 2007.

[33] Lukas Novotny and Bert Hecht. *Principles of nano-optics*. Cambridge university press, 2012.

[34] Jonathan Zenneck. Über die fortpflanzung ebener elektromagnetischer wellen längs einer ebenen leiterfläche und ihre beziehung zur drahtlosen telegraphie. *Annalen der Physik*, 328 (10):846–866, 1907.

[35] Arnold Sommerfeld. Über die ausbreitung der wellen in der drahtlosen telegraphie. *Annalen der Physik*, 333(4):665–736, 1909.

[36] RW Wood. Xlii. on a remarkable case of uneven distribution of light in a diffraction grating spectrum. *The London, Edinburgh, and Dublin Philosophical Magazine and Journal of Science*, 4(21):396–402, 1902.

[37] Lord Rayleigh. On the dynamical theory of gratings. *Proceedings of the Royal Society of London. Series A, Containing Papers of a Mathematical and Physical Character*, 79(532): 399–416, 1907.

[38] U Fano. The theory of anomalous diffraction gratings and of quasi-stationary waves on metallic surfaces (sommerfeld's waves). *JOSA*, 31(3):213–222, 1941.

[39] RH Ritchie. Plasma losses by fast electrons in thin films. *Physical Review*, 106(5):874, 1957.

[40] RH Ritchie, ET Arakawa, JJ Cowan, and RN Hamm. Surface-plasmon resonance effect in grating diffraction. *Physical Review Letters*, 21(22):1530, 1968.

[41] Andreas Otto. Excitation of nonradiative surface plasma waves in silver by the method of frustrated total reflection. *Zeitschrift für Physik*, 216(4):398–410, 1968.

[42] Erwin Kretschmann and Heinz Raether. Notizen: radiative decay of non radiative surface plasmons excited by light. *Zeitschrift für Naturforschung A*, 23(12):2135–2136, 1968.

[43] Anatoly V Zayats, Igor I Smolyaninov, and Alexei A Maradudin. Nano-optics of surface plasmon polaritons. *Physics reports*, 408(3):131–314, 2005.

[44] Peter B Johnson and R-W_ Christy. Optical constants of the noble metals. *Physical review B*, 6(12):4370, 1972.

[45] K Lance Kelly, Eduardo Coronado, Lin Lin Zhao, George C Schatz, et al. The optical properties of metal nanoparticles: the influence of size, shape, and dielectric environment. *Journal of Physical Chemistry B-Condensed Phase*, 107(3):668–677, 2003.

[46] Anatoly V Zayats and Igor I Smolyaninov. Near-field photonics: surface plasmon polaritons and localized surface plasmons. *Journal of Optics A: Pure and Applied Optics*, 5(4):S16, 2003.

[47] Eleonora Petryayeva and Ulrich J Krull. Localized surface plasmon resonance: nanostructures, bioassays and biosensing—a review. *Analytica chimica acta*, 706(1):8–24, 2011.

[48] Craig F Bohren and Donald R Huffman. *Absorption and scattering of light by small particles*. John Wiley & Sons, 2008.

[49] Uwe Kreibig and Michael Vollmer. *Optical properties of metal clusters*, volume 25. Springer Science & Business Media, 2013.

[50] Peter Zijlstra, Marijn van Stee, Nico Verhart, Ziyu Gu, and Michel Orrit. Rotational diffusion and alignment of short gold nanorods in an external electric field. *Physical Chemistry Chemical Physics*, 14(13):4584–4588, 2012.

[51] Wenshan Cai and Vladimir M Shalaev. *Optical metamaterials*, volume 10. Springer, 2010.

[52] Viktor G Veselago. The electrodynamics of substances with simultaneously negative values of and μ. *Soviet physics uspekhi*, 10(4):509, 1968.

[53] JB Pendry, AJ Holden, WJ Stewart, and I Youngs. Extremely low frequency plasmons in metallic mesostructures. *Physical review letters*, 76(25):4773, 1996.

[54] John B Pendry, A J_ Holden, DJ Robbins, and WJ Stewart. Magnetism from conductors and enhanced nonlinear phenomena. *IEEE transactions on microwave theory and techniques*, 47(11):2075–2084, 1999.

[55] David R Smith, Willie J Padilla, DC Vier, Syrus C Nemat-Nasser, and Seldon Schultz. Composite medium with simultaneously negative permeability and permittivity. *Physical review letters*, 84(18):4184, 2000.

[56] RA Shelby, DR Smith, SC Nemat-Nasser, and Sheldon Schultz. Microwave transmission through a two-dimensional, isotropic, left-handed metamaterial. *Applied Physics Letters*, 78 (4):489–491, 2001.

[57] Richard A Shelby, David R Smith, and Seldon Schultz. Experimental verification of a negative index of refraction. *science*, 292(5514):77–79, 2001.

[58] David R Smith, John B Pendry, and Mike CK Wiltshire. Metamaterials and negative refractive index. *Science*, 305(5685):788–792, 2004.

[59] John Brian Pendry. Negative refraction makes a perfect lens. *Physical review letters*, 85(18): 3966, 2000.

[60] David Schurig, JJ Mock, BJ Justice, Steven A Cummer, John B Pendry, AF Starr, and DR Smith. Metamaterial electromagnetic cloak at microwave frequencies. *Science*, 314(5801): 977–980, 2006.

[61] NI Landy, S Sajuyigbe, JJ Mock, DR Smith, and WJ Padilla. Perfect metamaterial absorber. *Physical review letters*, 100(20):207402, 2008.

[62] Hou-Tong Chen, Willie J Padilla, Joshua MO Zide, Arthur C Gossard, Antoinette J Taylor, and Richard D Averitt. Active terahertz metamaterial devices. *Nature*, 444(7119):597–600, 2006.

[63] WJ Padilla, MT Aronsson, C Highstrete, Mark Lee, AJ Taylor, and RD Averitt. Electrically resonant terahertz metamaterials: Theoretical and experimental investigations. *Physical Review B*, 75(4):041102, 2007.

[64] Hou-Tong Chen, Willie J Padilla, Joshua MO Zide, Seth R Bank, Arthur C Gossard, Antoinette J Taylor, and Richard D Averitt. Ultrafast optical switching of terahertz metamaterials fabricated on eras/gaas nanoisland superlattices. *Optics letters*, 32(12):1620–1622, 2007.

[65] Xianliang Liu, Talmage Tyler, Tatiana Starr, Anthony F Starr, Nan Marie Jokerst, and Willie J Padilla. Taming the blackbody with infrared metamaterials as selective thermal emitters. *Physical review letters*, 107(4):045901, 2011.

[66] Long Ju, Baisong Geng, Jason Horng, Caglar Girit, Michael Martin, Zhao Hao, Hans A Bechtel, Xiaogan Liang, Alex Zettl, Y Ron Shen, et al. Graphene plasmonics for tunable terahertz metamaterials. *Nature nanotechnology*, 6(10):630–634, 2011.

[67] Shuang Zhang, Wenjun Fan, NC Panoiu, KJ Malloy, RM Osgood, and SRJ Brueck. Experimental demonstration of near-infrared negative-index metamaterials. *Physical review letters*, 95(13):137404, 2005.

[68] C Enkrich, M Wegener, S Linden, S Burger, L Zschiedrich, F Schmidt, JF Zhou, Th Koschny, and CM Soukoulis. Magnetic metamaterials at telecommunication and visible frequencies. *Physical review letters*, 95(20):203901, 2005.

[69] Gunnar Dolling, Martin Wegener, Costas M Soukoulis, and Stefan Linden. Negative-index metamaterial at 780 nm wavelength. *Optics letters*, 32(1):53–55, 2007.

[70] Vladimir M Shalaev, Wenshan Cai, Uday K Chettiar, Hsiao-Kuan Yuan, Andrey K Sarychev, Vladimir P Drachev, and Alexander V Kildishev. Negative index of refraction in optical metamaterials. *Optics letters*, 30(24):3356–3358, 2005.

[71] Wenshan Cai, Uday K Chettiar, Alexander V Kildishev, and Vladimir M Shalaev. Optical cloaking with metamaterials. *Nature photonics*, 1(4):224–227, 2007.

[72] Costas M Soukoulis, Stefan Linden, and Martin Wegener. Negative refractive index at optical wavelengths. *Science*, 315(5808):47–49, 2007.

[73] Jie Yao, Zhaowei Liu, Yongmin Liu, Yuan Wang, Cheng Sun, Guy Bartal, Angelica M Stacy, and Xiang Zhang. Optical negative refraction in bulk metamaterials of nanowires. *Science*, 321(5891):930–930, 2008.

[74] AV Kabashin, P Evans, S Pastkovsky, W Hendren, GA Wurtz, R Atkinson, R Pollard, VA Podolskiy, and AV Zayats. Plasmonic nanorod metamaterials for biosensing. *Nature materials*, 8(11):867–871, 2009.

[75] Mazhar E Nasir, Wayne Dickson, Gregory A Wurtz, William P Wardley, and Anatoly V Zayats. Hydrogen detected by the naked eye: Optical hydrogen gas sensors based on core/shell plasmonic nanorod metamaterials. *Advanced Materials*, 2014.

[76] Nicholas Fang, Hyesog Lee, Cheng Sun, and Xiang Zhang. Sub–diffraction-limited optical imaging with a silver superlens. *Science*, 308(5721):534–537, 2005.

[77] Vladimir P Drachev, Viktor A Podolskiy, and Alexander V Kildishev. Hyperbolic metamaterials: new physics behind a classical problem. *Optics express*, 21(12):15048–15064, 2013.

[78] Prashant Shekhar, Jonathan Atkinson, and Zubin Jacob. Hyperbolic metamaterials: fundamentals and applications. *Nano Convergence*, 1(1):1–17, 2014.

[79] Alexander Poddubny, Ivan Iorsh, Pavel Belov, and Yuri Kivshar. Hyperbolic metamaterials. *Nature Photonics*, 7(12):948–957, 2013.

[80] Yu Guo, Ward Newman, Cristian L Cortes, and Zubin Jacob. Applications of hyperbolic metamaterial substrates. *Advances in OptoElectronics*, 2012, 2012.

[81] CL Cortes, W Newman, S Molesky, and Z Jacob. Quantum nanophotonics using hyperbolic metamaterials. *Journal of Optics*, 14(6):063001, 2012.

[82] ME Nasir, S Peruch, N Vasilantonakis, WP Wardley, W Dickson, GA Wurtz, and AV Zayats. Tuning the effective plasma frequency of nanorod metamaterials from visible to telecom wavelengths. *Applied Physics Letters*, 107(12):121110, 2015.

[83] Alexandra Boltasseva and Harry A Atwater. Low-loss plasmonic metamaterials. *Science*, 331 (6015):290–291, 2011.

[84] Gururaj V Naik, Vladimir M Shalaev, and Alexandra Boltasseva. Alternative plasmonic materials: beyond gold and silver. *Advanced Materials*, 25(24):3264–3294, 2013.

[85] Polina V Kapitanova, Pavel Ginzburg, Francisco J Rodríguez-Fortuño, Dmitry S Filonov, Pavel M Voroshilov, Pavel A Belov, Alexander N Poddubny, Yuri S Kivshar, Gregory A Wurtz, and Anatoly V Zayats. Photonic spin hall effect in hyperbolic metamaterials for polarization-controlled routing of subwavelength modes. *Nature communications*, 5, 2014.

[86] L Felsen. Focusing by an anisotropic plasma interface. *IEEE Transactions on Antennas and Propagation*, 12(5):624–635, 1964.

[87] Vladislav V Yakovlev, Wayne Dickson, Antony Murphy, John McPhillips, Robert J Pollard, Viktor A Podolskiy, and Anatoly V Zayats. Ultrasensitive non-resonant detection of ultrasound with plasmonic metamaterials. *Advanced Materials*, 25(16):2351–2356, 2013.

[88] Edward M Purcell. Spontaneous emission probabilities at radio frequencies. *Physical Review*, 69:681, 1946.

[89] Zubin Jacob, Igor I Smolyaninov, and Evgenii E Narimanov. Broadband purcell effect: Radiative decay engineering with metamaterials. *Applied Physics Letters*, 100(18):181105, 2012.

[90] MA Noginov, H Li, Yu A Barnakov, D Dryden, G Nataraj, G Zhu, CE Bonner, M Mayy, Z Jacob, and EE Narimanov. Controlling spontaneous emission with metamaterials. *Optics letters*, 35(11):1863–1865, 2010.

[91] Alexander N Poddubny, Pavel A Belov, and Yuri S Kivshar. Electric and magnetic dipole radiation and purcell effect in hyperbolic metamaterials. In *SPIE NanoScience+ Engineering*, pages 88060T–88060T. International Society for Optics and Photonics, 2013.

[92] Lorenzo Ferrari, Dylan Lu, Dominic Lepage, and Zhaowei Liu. Enhanced spontaneous emission inside hyperbolic metamaterials. *Optics express*, 22(4):4301–4306, 2014.

[93] Dylan Lu, Jimmy J Kan, Eric E Fullerton, and Zhaowei Liu. Enhancing spontaneous emission rates of molecules using nanopatterned multilayer hyperbolic metamaterials. *Nature nanotechnology*, 9(1):48–53, 2014.

[94] J Kim, Vladimir P Drachev, Z Jacob, Gururaj V Naik, Alexandra Boltasseva, Evgenii E Narimanov, and Vladimir M Shalaev. Improving the radiative decay rate for dye molecules with hyperbolic metamaterials. *Optics express*, 20(7):8100–8116, 2012.

[95] Alexander N Poddubny, Pavel A Belov, and Yuri S Kivshar. Purcell effect in wire metamaterials. *Physical Review B*, 87(3):035136, 2013.

[96] Alexander N Poddubny, Pavel A Belov, and Yuri S Kivshar. Spontaneous radiation of a finite-size dipole emitter in hyperbolic media. *Physical Review A*, 84(2):023807, 2011.

[97] P Michler, A Kiraz, C Becher, WV Schoenfeld, PM Petroff, Lidong Zhang, E Hu, and A Imamoglu. A quantum dot single-photon turnstile device. *Science*, 290(5500):2282–2285, 2000.

[98] Peter Lodahl, A Floris Van Driel, Ivan S Nikolaev, Arie Irman, Karin Overgaag, Daniël Vanmaekelbergh, and Willem L Vos. Controlling the dynamics of spontaneous emission from quantum dots by photonic crystals. *Nature*, 430(7000):654–657, 2004.

[99] P Evans, WR Hendren, R Atkinson, GA Wurtz, W Dickson, AV Zayats, and RJ Pollard. Growth and properties of gold and nickel nanorods in thin film alumina. *Nanotechnology*, 17 (23):5746, 2006.

[100] GA Wurtz, W Dickson, D O'Connor, R Atkinson, W Hendren, P Evans, R Pollard, and AV Zayats. Guided plasmonic modes in nanorod assemblies: strong electromagnetic coupling regime. *Optics express*, 16(10):7460–7470, 2008.

[101] Justin Elser, Robyn Wangberg, Viktor A Podolskiy, and Evgenii E Narimanov. Nanowire metamaterials with extreme optical anisotropy. *Applied physics letters*, 89(26):261102, 2006.

[102] Vadim A Markel. Introduction to the maxwell garnett approximation: tutorial. *JOSA A*, 33 (7):1244–1256, 2016.

[103] Sanong Ekgasit, Chuchaat Thammacharoen, and Wolfgang Knoll. Surface plasmon resonance spectroscopy based on evanescent field treatment. *Analytical chemistry*, 76(3):561–568, 2004.

[104] RJ Pollard, Antony Murphy, WR Hendren, PR Evans, Ron Atkinson, GA Wurtz, AV Zayats, and Viktor A Podolskiy. Optical nonlocalities and additional waves in epsilon-near-zero metamaterials. *Physical review letters*, 102(12):127405, 2009.

[105] Brian M Wells, Anatoly V Zayats, and Viktor A Podolskiy. Nonlocal optics of plasmonic nanowire metamaterials. *Physical Review B*, 89(3):035111, 2014.

[106] Enrico Fermi. Quantum theory of radiation. *Reviews of modern physics*, 4(1):87, 1932.

[107] KH Drexhage. Influence of a dielectric interface on fluorescence decay time. *Journal of Luminescence*, 1:693–701, 1970.

[108] KH Drexhage and E Wolf. Progress in optics. *Vol. 12North-Holland, Amsterdam*, page 165, 1974.

[109] RM Amos and WL Barnes. Modification of the spontaneous emission rate of eu 3+ ions close to a thin metal mirror. *Physical Review B*, 55(11):7249, 1997.

[110] WL Barnes. Fluorescence near interfaces: the role of photonic mode density. *journal of modern optics*, 45(4):661–699, 1998.

[111] George W Ford and Willes H Weber. Electromagnetic interactions of molecules with metal surfaces. *Physics Reports*, 113(4):195–287, 1984.

[112] DH Waldeck, AP Alivisatos, and CB Harris. Nonradiative damping of molecular electronic excited states by metal surfaces. *Surface Science*, 158(1-3):103–125, 1985.

[113] WH Weber and CF Eagen. Energy transfer from an excited dye molecule to the surface plasmons of an adjacent metal. *Optics Letters*, 4(8):236–238, 1979.

[114] Joseph R Lakowicz. Radiative decay engineering 3. surface plasmon-coupled directional emission. *Analytical biochemistry*, 324(2):153–169, 2004.

[115] Ignacy Gryczynski, Joanna Malicka, Zygmunt Gryczynski, and Joseph R Lakowicz. Radiative decay engineering 4. experimental studies of surface plasmon-coupled directional emission. *Analytical biochemistry*, 324(2):170–182, 2004.

[116] I Pockrand, A Brillante, and D Möbius. Nonradiative decay of excited molecules near a metal surface. *Chemical Physics Letters*, 69(3):499–504, 1980.

[117] RR Chance, A Prock, and R Silbey. Molecular fluorescence and energy transfer near interfaces. *Adv. Chem. Phys*, 37(1):65, 1978.

[118] Wolfgang Knoll, Michael R Philpott, JD Swalen, and Alberto Girlando. Emission of light from ag metal gratings coated with dye monolayer assemblies. *The Journal of Chemical Physics*, 75(10):4795–4799, 1981.

[119] Arnold Adams, John Moreland, PK Hansma, and Zack Schlesinger. Light emission from surface-plasmon and waveguide modes excited by n atoms near a silver grating. *Physical Review B*, 25(6):3457, 1982.

[120] Kevin G Sullivan, Oliver King, Christina Sigg, and Dennis G Hall. Directional, enhanced fluorescence from molecules near a periodic surface. *Applied optics*, 33(13):2447–2454, 1994.

[121] RM Amos and WL Barnes. Modification of spontaneous emission lifetimes in the presence of corrugated metallic surfaces. *Physical Review B*, 59(11):7708, 1999.

[122] Piers Andrew and William L Barnes. Molecular fluorescence above metallic gratings. *Physical Review B*, 64(12):125405, 2001.

[123] S Wedge, Ian R Hooper, I Sage, and William L Barnes. Light emission through a corrugated metal film: The role of cross-coupled surface plasmon polaritons. *Physical Review B*, 69(24): 245418, 2004.

[124] Elizaveta Klantsataya, Alexandre François, Heike Ebendorff-Heidepriem, Beniamino Sciacca, Agnieszka Zuber, and Tanya M Monro. Effect of surface roughness on metal enhanced fluorescence in planar substrates and optical fibers. *Optical Materials Express*, 6(6):2128–2138, 2016.

[125] Joseph R Lakowicz, Yibing Shen, Sabato D'Auria, Joanna Malicka, Jiyu Fang, Zygmunt Gryczynski, and Ignacy Gryczynski. Radiative decay engineering: 2. effects of silver island films on fluorescence intensity, lifetimes, and resonance energy transfer. *Analytical biochemistry*, 301(2):261–277, 2002.

[126] Jia Li, Alexey V Krasavin, Linden Webster, Paulina Segovia, Anatoly V Zayats, and David Richards. Spectral variation of fluorescence lifetime near single metal nanoparticles. *Scientific reports*, 5, 2016.

[127] Julie Goffard, Davy Gérard, Patrice Miska, Anne-Laure Baudrion, Régis Deturche, and Jérôme Plain. Plasmonic engineering of spontaneous emission from silicon nanocrystals. *Scientific reports*, 3:2672, 2013.

[128] Rizia Bardhan, Nathaniel K Grady, Joseph R Cole, Amit Joshi, and Naomi J Halas. Fluorescence enhancement by au nanostructures: nanoshells and nanorods. *Acs Nano*, 3(3):744–752, 2009.

[129] Keiko Munechika, Yeechi Chen, Andreas F Tillack, Abhishek P Kulkarni, Ilan Jen-La Plante, Andrea M Munro, and David S Ginger. Spectral control of plasmonic emission enhancement from quantum dots near single silver nanoprisms. *Nano letters*, 10(7):2598–2603, 2010.

[130] Felicia Tam, Glenn P Goodrich, Bruce R Johnson, and Naomi J Halas. Plasmonic enhancement of molecular fluorescence. *Nano Letters*, 7(2):496–501, 2007.

[131] Pascal Anger, Palash Bharadwaj, and Lukas Novotny. Enhancement and quenching of single-molecule fluorescence. *Physical review letters*, 96(11):113002, 2006.

[132] E Dulkeith, AC Morteani, T Niedereichholz, TA Klar, J Feldmann, SA Levi, FCJM Van Veggel, DN Reinhoudt, M Möller, and DI Gittins. Fluorescence quenching of dye molecules near gold nanoparticles: radiative and nonradiative effects. *Physical review letters*, 89(20):203002, 2002.

[133] Dmitry V Guzatov, Svetlana V Vaschenko, Vyacheslav V Stankevich, Anatoly Ya Lunevich, Yuri F Glukhov, and Sergey V Gaponenko. Plasmonic enhancement of molecular fluorescence near silver nanoparticles: theory, modeling, and experiment. *The Journal of Physical Chemistry C*, 116(19):10723–10733, 2012.

[134] Sergei Kühn, Ulf Håkanson, Lavinia Rogobete, and Vahid Sandoghdar. Enhancement of single-molecule fluorescence using a gold nanoparticle as an optical nanoantenna. *Physical review letters*, 97(1):017402, 2006.

[135] Tian Ming, Lei Zhao, Zhi Yang, Huanjun Chen, Lingdong Sun, Jianfang Wang, and Chunhua Yan. Strong polarization dependence of plasmon-enhanced fluorescence on single gold nanorods. *Nano letters*, 9(11):3896–3903, 2009.

[136] Thomas W Ebbesen, HJ Lezec, HF Ghaemi, Tineke Thio, and PA Wolff. Extraordinary optical transmission through sub-wavelength hole arrays. *nature*, 391(6668):667, 1998.

[137] Jérôme Wenger, Davy Gérard, José Dintinger, Oussama Mahboub, Nicolas Bonod, Evgeny Popov, Thomas W Ebbesen, and Hervé Rigneault. Emission and excitation contributions to enhanced single molecule fluorescence by gold nanometric apertures. *Optics express*, 16(5): 3008–3020, 2008.

[138] Hervé Rigneault, Jérémie Capoulade, José Dintinger, Jérôme Wenger, Nicolas Bonod, Evgeni Popov, Thomas W Ebbesen, and Pierre-François Lenne. Enhancement of single-molecule fluorescence detection in subwavelength apertures. *Physical Review Letters*, 95(11):117401, 2005.

[139] Anika Kinkhabwala, Zongfu Yu, Shanhui Fan, Yuri Avlasevich, Klaus Müllen, and WE Moerner. Large single-molecule fluorescence enhancements produced by a bowtie nanoantenna. *Nature Photonics*, 3(11):654–657, 2009.

[140] Lukas Novotny and Niek Van Hulst. Antennas for light. *Nature photonics*, 5(2):83–90, 2011.

[141] David P Fromm, Arvind Sundaramurthy, P James Schuck, Gordon Kino, and WE Moerner. Gap-dependent optical coupling of single "bowtie" nanoantennas resonant in the visible. *Nano letters*, 4(5):957–961, 2004.

[142] Lavinia Rogobete, Franziska Kaminski, Mario Agio, and Vahid Sandoghdar. Design of plasmonic nanoantennae for enhancing spontaneous emission. *Optics letters*, 32(12):1623–1625, 2007.

[143] M Ringler, A Schwemer, M Wunderlich, A Nichtl, K Kürzinger, TA Klar, and J Feldmann. Shaping emission spectra of fluorescent molecules with single plasmonic nanoresonators. *Physical review letters*, 100(20):203002, 2008.

[144] OL Muskens, V Giannini, José A Sánchez-Gil, and J Gomez Rivas. Strong enhancement of the radiative decay rate of emitters by single plasmonic nanoantennas. *Nano letters*, 7(9): 2871–2875, 2007.

[145] Reuben M Bakker, Hsiao-Kuan Yuan, Zhengtong Liu, Vladimir P Drachev, Alexander V Kildishev, Vladimir M Shalaev, Rasmus H Pedersen, Samuel Gresillon, and Alexandra Boltasseva. Enhanced localized fluorescence in plasmonic nanoantennae. *Applied Physics Letters*, 92(4):043101, 2008.

[146] Tim H Taminiau, Fernando D Stefani, and Niek F van Hulst. Enhanced directional excitation and emission of single emitters by a nano-optical yagi-uda antenna. *Optics express*, 16(14): 10858–10866, 2008.

[147] Alberto G Curto, Giorgio Volpe, Tim H Taminiau, Mark P Kreuzer, Romain Quidant, and Niek F van Hulst. Unidirectional emission of a quantum dot coupled to a nanoantenna. *Science*, 329(5994):930–933, 2010.

[148] Heykel Aouani, Oussama Mahboub, Eloïse Devaux, Hervé Rigneault, Thomas W Ebbesen, and Jerome Wenger. Plasmonic antennas for directional sorting of fluorescence emission. *Nano letters*, 11(6):2400–2406, 2011.

[149] Young Chul Jun, Kevin CY Huang, and Mark L Brongersma. Plasmonic beaming and active control over fluorescent emission. *Nature communications*, 2:283, 2011.

[150] Ruben Esteban, TV Teperik, and Jean-Jacques Greffet. Optical patch antennas for single photon emission using surface plasmon resonances. *Physical review letters*, 104(2):026802, 2010.

[151] Cherif Belacel, Benjamin Habert, Florian Bigourdan, François Marquier, J-P Hugonin, S Michaelis de Vasconcellos, Xavier Lafosse, Laurent Coolen, Catherine Schwob, Clémentine Javaux, et al. Controlling spontaneous emission with plasmonic optical patch antennas. *Nano letters*, 13(4):1516–1521, 2013.

[152] Gleb M Akselrod, Christos Argyropoulos, Thang B Hoang, Cristian Ciracì, Chao Fang, Jiani Huang, David R Smith, and Maiken H Mikkelsen. Probing the mechanisms of large purcell enhancement in plasmonic nanoantennas. *Nature Photonics*, 8(11):835–840, 2014.

[153] Thang B Hoang, Gleb M Akselrod, Christos Argyropoulos, Jiani Huang, David R Smith, and Maiken H Mikkelsen. Ultrafast spontaneous emission source using plasmonic nanoantennas. *Nature communications*, 6, 2015.

[154] Sebastian Gerber, Frank Reil, Ulrich Hohenester, Thomas Schlagenhaufen, Joachim R Krenn, and Alfred Leitner. Tailoring light emission properties of fluorophores by coupling to resonance-tuned metallic nanostructures. *Physical Review B*, 75(7):073404, 2007.

[155] Hans Mertens, Julie S Biteen, Harry A Atwater, and Albert Polman. Polarization-selective plasmon-enhanced silicon quantum-dot luminescence. *Nano letters*, 6(11):2622–2625, 2006.

[156] G Vecchi, V Giannini, and J Gómez Rivas. Surface modes in plasmonic crystals induced by diffractive coupling of nanoantennas. *Physical Review B*, 80(20):201401, 2009.

[157] SRK Rodriguez, G Lozano, MA Verschuuren, R Gomes, Karel Lambert, Bram De Geyter, Antti Hassinen, Dries Van Thourhout, Zeger Hens, and J Gómez Rivas. Quantum rod emission coupled to plasmonic lattice resonances: A collective directional source of polarized light. *Applied Physics Letters*, 100(11):111103, 2012.

[158] Shinpei Ogawa, Masahiro Imada, Susumu Yoshimoto, Makoto Okano, and Susumu Noda. Control of light emission by 3d photonic crystals. *Science*, 305(5681):227–229, 2004.

[159] Masayuki Fujita, Shigeki Takahashi, Yoshinori Tanaka, Takashi Asano, and Susumu Noda. Simultaneous inhibition and redistribution of spontaneous light emission in photonic crystals. *Science*, 308(5726):1296–1298, 2005.

[160] Kevin Hennessy, Antonio Badolato, M Winger, D Gerace, Mete Atatüre, S Gulde, S Fält, Evelyn L Hu, and A Imamoğlu. Quantum nature of a strongly coupled single quantum dot–cavity system. *Nature*, 445(7130):896–899, 2007.

[161] J-M Gérard and Bruno Gayral. Strong purcell effect for inas quantum boxes in three-dimensional solid-state microcavities. *Journal of lightwave technology*, 17(11):2089–2095, 1999.

[162] Kasey J Russell, Tsung-Li Liu, Shanying Cui, and Evelyn L Hu. Large spontaneous emission enhancement in plasmonic nanocavities. *Nature Photonics*, 6(7):459–462, 2012.

[163] Harish NS Krishnamoorthy, Zubin Jacob, Evgenii Narimanov, Ilona Kretzschmar, and Vinod M Menon. Topological transitions in metamaterials. *Science*, 336(6078):205–209, 2012.

[164] Zubin Jacob, J-Y Kim, GV Naik, Alexandra Boltasseva, EE Narimanov, and VM Shalaev. Engineering photonic density of states using metamaterials. *Applied Physics B*, 100(1): 215–218, 2010.

[165] Mikhail Y Shalaginov, Satoshi Ishii, Jingjing Liu, J Liu, J Irudayaraj, A Lagutchev, AV Kildishev, and VM Shalaev. Broadband enhancement of spontaneous emission from nitrogen-vacancy centers in nanodiamonds by hyperbolic metamaterials. *Applied Physics Letters*, 102 (17):173114, 2013.

[166] Ward D Newman, Cristian L Cortes, and Zubin Jacob. Enhanced and directional single-photon emission in hyperbolic metamaterials. *JOSA B*, 30(4):766–775, 2013.

[167] T Tumkur, G Zhu, P Black, Yu A Barnakov, CE Bonner, and MA Noginov. Control of spontaneous emission in a volume of functionalized hyperbolic metamaterial. *Applied Physics Letters*, 99(15):151115, 2011.

[168] T Galfsky, HNS Krishnamoorthy, W Newman, EE Narimanov, Z Jacob, and VM Menon. Active hyperbolic metamaterials: enhanced spontaneous emission and light extraction. *Optica*, 2(1):62–65, 2015.

[169] Alexander N Poddubny, Pavel A Belov, Pavel Ginzburg, Anatoly V Zayats, and Yuri S Kivshar. Microscopic model of purcell enhancement in hyperbolic metamaterials. *Physical Review B*, 86(3):035148, 2012.

[170] Jian Zhang, Yi Fu, and Joseph R Lakowicz. Enhanced förster resonance energy transfer (fret) on a single metal particle. *The journal of physical chemistry C*, 111(1):50–56, 2007.

[171] Mathieu Lessard-Viger, Maxime Rioux, Luc Rainville, and Denis Boudreau. Fret enhancement in multilayer core- shell nanoparticles. *Nano letters*, 9(8):3066–3071, 2009.

[172] Xia Zhang, Cristian A Marocico, Manuela Lunz, Valerie A Gerard, Yurii K Gun'ko, Vladimir Lesnyak, Nikolai Gaponik, Andrei S Susha, Andrey L Rogach, and A Louise Bradley. Experimental and theoretical investigation of the distance dependence of localized surface plasmon coupled forster resonance energy transfer. *ACS nano*, 8(2):1273–1283, 2014.

[173] Manuela Lunz, Valerie A Gerard, Yurii K Gun'ko, Vladimir Lesnyak, Nikolai Gaponik, Andrei S Susha, Andrey L Rogach, and A Louise Bradley. Surface plasmon enhanced energy transfer between donor and acceptor cdte nanocrystal quantum dot monolayers. *Nano letters*, 11(8):3341–3345, 2011.

[174] Piers Andrew and William L Barnes. Förster energy transfer in an optical microcavity. *Science*, 290(5492):785–788, 2000.

[175] Chris E Finlayson, David S Ginger, and Neil C Greenham. Enhanced förster energy transfer in organic/inorganic bilayer optical microcavities. *Chemical physics letters*, 338(2):83–87, 2001.

[176] Toshihiro Nakamura, Minoru Fujii, Kenji Imakita, and Shinji Hayashi. Modification of energy transfer from si nanocrystals to er 3+ near a au thin film. *Physical Review B*, 72(23):235412, 2005.

[177] Toshihiro Nakamura, Minoru Fujii, Satoru Miura, Masaki Inui, and Shinji Hayashi. Enhancement and suppression of energy transfer from si nanocrystals to er ions through a control of the photonic mode density. *Physical Review B*, 74(4):045302, 2006.

[178] Freddy T Rabouw, Stephan A Den Hartog, Tim Senden, and Andries Meijerink. Photonic effects on the förster resonance energy transfer efficiency. *Nature communications*, 5, 2014.

[179] MJA De Dood, Jasper Knoester, A Tip, and Annemieke Polman. Förster transfer and the local optical density of states in erbium-doped silica. *Physical Review B*, 71(11):115102, 2005.

[180] Christian Blum, Niels Zijlstra, Ad Lagendijk, Martijn Wubs, Allard P Mosk, Vinod Subramaniam, and Willem L Vos. Nanophotonic control of the förster resonance energy transfer efficiency. *Physical review letters*, 109(20):203601, 2012.

[181] Frank Schleifenbaum, Andreas M Kern, Alexander Konrad, and Alfred J Meixner. Dynamic control of förster energy transfer in a photonic environment. *Physical Chemistry Chemical Physics*, 16(25):12812–12817, 2014.

[182] Alexander Konrad, Michael Metzger, Andreas M Kern, Marc Brecht, and Alfred J Meixner. Controlling the dynamics of förster resonance energy transfer inside a tunable sub-wavelength fabry–pérot-resonator. *Nanoscale*, 7(22):10204–10209, 2015.

[183] Thejaswi U Tumkur, John K Kitur, Carl E Bonner, Alexander N Poddubny, Evgenii E Narimanov, and Mikhail A Noginov. Control of förster energy transfer in the vicinity of metallic surfaces and hyperbolic metamaterials. *Faraday discussions*, 178:395–412, 2015.

[184] Vitaliy N Pustovit, Augustine M Urbas, and Tigran V Shahbazyan. Cooperative amplification of energy transfer in plasmonic systems. *Physical Review B*, 88(24):245427, 2013.

[185] Alexander N Poddubny. Collective förster energy transfer modified by a planar metallic mirror. *Physical Review B*, 92(15):155418, 2015.

[186] Petru Ghenuche, Juan de Torres, Satish Babu Moparthi, Victor Grigoriev, and Jérôme Wenger. Nanophotonic enhancement of the förster resonance energy-transfer rate with single nanoapertures. *Nano letters*, 14(8):4707–4714, 2014.

[187] Petru Ghenuche, Mathieu Mivelle, Juan de Torres, Satish Babu Moparthi, Hervé Rigneault, Niek F Van Hulst, María F García-Parajó, and Jérôme Wenger. Matching nanoantenna field confinement to fret distances enhances förster energy transfer rates. *Nano letters*, 15(9): 6193–6201, 2015.

[188] PM De Roque, NF van Hulst, and R Sapienza. Nanophotonic boost of intermolecular energy transfer. *New Journal of Physics*, 17(11):113052, 2015.

[189] Donald M Mattox. *Handbook of physical vapor deposition (PVD) processing*. William Andrew, 2010.

[190] Hideki Masuda and Kenji Fukuda. Ordered metal nanohole arrays made by a two-step replication of honeycomb structures of anodic alumina. *science*, 268(5216):1466, 1995.

[191] MJ Cole, J Siegel, SED Webb, R Jones, K Dowling, MJ Dayel, D Parsons-Karavassilis, PMW French, MJ Lever, LOD Sucharov, et al. Time-domain whole-field fluorescence lifetime imaging with optical sectioning. *Journal of microscopy*, 203(3):246–257, 2001.

[192] AC Mitchell, JE Wall, JG Murray, and CG Morgan. Measurement of nanosecond time-resolved fluorescence with a directly gated interline ccd camera. *Journal of microscopy*, 206 (3):233–238, 2002.

[193] W Becker, A Bergmann, MA Hink, K König, K Benndorf, and C Biskup. Fluorescence lifetime imaging by time-correlated single-photon counting. *Microscopy research and technique*, 63 (1):58–66, 2004.

[194] Wolfgang Becker. *The bh TCSPC handbook*. Becker & Hickl, 2014.

[195] Desmond O'Connor. *Time-correlated single photon counting*. Academic Press, 1984.

[196] Rafal Luchowski, Zygmunt Gryczynski, Pabak Sarkar, Julian Borejdo, Mariusz Szabelski, Peter Kapusta, and Ignacy Gryczynski. Instrument response standard in time-resolved fluorescence. *Review of Scientific Instruments*, 80(3):033109, 2009.

[197] Bart Van Oort, Alexey Amunts, Jan Willem Borst, Arie Van Hoek, Nathan Nelson, Herbert Van Amerongen, and Roberta Croce. Picosecond fluorescence of intact and dissolved psi-lhci crystals. *Biophysical journal*, 95(12):5851–5861, 2008.

[198] Rahul Chib, Sunil Shah, Zygmunt Gryczynski, Rafal Fudala, Julian Borejdo, Bogumil Zelent, Maria G Corradini, Richard D Ludescher, and Ignacy Gryczynski. Standard reference for instrument response function in fluorescence lifetime measurements in visible and near infrared. *Measurement Science and Technology*, 27(2):027001, 2015.

[199] Mariusz Szabelski, Rafal Luchowski, Zygmunt Gryczynski, Peter Kapusta, Uwe Ortmann, and Ignacy Gryczynski. Evaluation of instrument response functions for lifetime imaging detectors using quenched rose bengal solutions. *Chemical Physics Letters*, 471(1):153–159, 2009.

[200] Mengwei Liu, Menghui Jia, Haifeng Pan, Lei Li, Mengfang Chang, Hua Ren, Françoise Argoul, Sanjun Zhang, and Jianhua Xu. Instrument response standard in time-resolved fluorescence spectroscopy at visible wavelength: quenched fluorescein sodium. *Applied spectroscopy*, 68 (5):577–583, 2014.

[201] William R Ware, Laurence J Doemeny, and Thomas L Nemzek. Deconvolution of fluorescence and phosphorescence decay curves. least-squares method. *The Journal of Physical Chemistry*, 77(17):2038–2048, 1973.

[202] Amiram Grinvald and Izchak Z Steinberg. On the analysis of fluorescence decay kinetics by the method of least-squares. *Analytical biochemistry*, 59(2):583–598, 1974.

[203] Mugurel G Badea and Ludwig Brand. [17] time-resolved fluorescence measurements. *Methods in enzymology*, 61:378–425, 1979.

[204] Irvin Isenberg and Robert D Dyson. The analysis of fluorescence decay by a method of moments. *Biophysical journal*, 9(11):1337–1350, 1969.

[205] Stephen W Provencher. Inverse problems in polymer characterization: direct analysis of polydispersity with photon correlation spectroscopy. *Die Makromolekulare Chemie*, 180(1): 201–209, 1979.

[206] A Gafni, Robert L Modlin, and Ludwig Brand. Analysis of fluorescence decay curves by means of the laplace transformation. *Biophysical journal*, 15(3):263, 1975.

[207] SW Provencher. A fourier method for the analysis of exponential decay curves. *Biophysical journal*, 16(1):27, 1976.

[208] DV O'Connor, WR Ware, and JC Andre. Deconvolution of fluorescence decay curves. a critical comparison of techniques. *Journal of Physical Chemistry*, 83(10):1333–1343, 1979.

[209] David F Eaton. Recommended methods for fluorescence decay analysis. *Pure and Applied Chemistry*, 62(8):1631–1648, 1990.

[210] Kaj Madsen, Hans Bruun Nielsen, and Ole Tingleff. Methods for non-linear least squares problems, 2004.

[211] Donald W Marquardt. An algorithm for least-squares estimation of nonlinear parameters. *Journal of the society for Industrial and Applied Mathematics*, 11(2):431–441, 1963.

[212] Kenneth Levenberg. A method for the solution of certain non-linear problems in least squares. *Quarterly of applied mathematics*, 2(2):164–168, 1944.

[213] Michael L Johnson and Lindsay M Faunt. [1] parameter estimation by least-squares methods. *Methods in enzymology*, 210:1–37, 1992.

[214] Henri Gavin. The levenberg-marquardt method for nonlinear least squares curve-fitting problems, 2011.

[215] Stephen W Provencher. A constrained regularization method for inverting data represented by linear algebraic or integral equations. *Computer Physics Communications*, 27(3):213–227, 1982.

[216] PH Lissberger and RG Nelson. Optical properties of thin film au-mgf2 cermets. *Thin Solid Films*, 21(1):159–172, 1974.

[217] N Vasilantonakis, GA Wurtz, VA Podolskiy, and AV Zayats. Refractive index sensing with hyperbolic metamaterials: strategies for biosensing and nonlinearity enhancement. *Optics express*, 23(11):14329–14343, 2015.

[218] Gregory A Wurtz, Robert Pollard, Willam Hendren, GP Wiederrecht, DJ Gosztola, VA Podolskiy, and Anatoly V Zayats. Designed ultrafast optical nonlinearity in a plasmonic nanorod metamaterial enhanced by nonlocality. *Nature nanotechnology*, 6(2):107–111, 2011.

[219] Kun-Tong Tsai, Gregory A Wurtz, Jen-You Chu, Tian-You Cheng, Huai-Hsien Wang, Alexey V Krasavin, Jr-Hau He, Brian M Wells, Viktor A Podolskiy, Juen-Kai Wang, et al. Looking into meta-atoms of plasmonic nanowire metamaterial. *Nano letters*, 14(9):4971–4976, 2014.

[220] GW Ford and WH Weber. Electromagnetic effects on a molecule at a metal surface: I. effects of nonlocality and finite molecular size. *Surface Science*, 109(2):451–481, 1981.

[221] Alexey P Slobozhanyuk, Pavel Ginzburg, David A Powell, Ivan Iorsh, Alexander S Shalin, Paulina Segovia, Alexey V Krasavin, Gregory A Wurtz, Viktor A Podolskiy, Pavel A Belov, et al. Purcell effect in hyperbolic metamaterial resonators. *Physical Review B*, 92(19):195127, 2015.

[222] SRJ Brueck. Radiation from a dipole embedded in a dielectric slab. *IEEE Journal of Selected Topics in Quantum Electronics*, 6(6):899–910, 2000.

[223] Viktor A Podolskiy, Pavel Ginzburg, Brian Wells, and Anatoly V Zayats. Light emission in nonlocal plasmonic metamaterials. *Faraday discussions*, 178:61–70, 2015.

[224] Ashwin C Atre, Benjamin JM Brenny, Toon Coenen, Aitzol García-Etxarri, Albert Polman, and Jennifer A Dionne. Nanoscale optical tomography with cathodoluminescence spectroscopy. *Nature nanotechnology*, 10(5):429–436, 2015.

[225] Silvia Peruch, Andres Neira, Gregory A Wurtz, Brian Wells, Viktor A Podolskiy, and Anatoly V Zayats. Geometry defines ultrafast hot-carrier dynamics and kerr nonlinearity in plasmonic metamaterial waveguides and cavities. *Advanced Optical Materials*, 5(15), 2017.

[226] Pavel Ginzburg, Diane J Roth, Mazhar E Nasir, Paulina Segovia, Alexey V Krasavin, James Levitt, Liisa M Hirvonen, Brian Wells, Klaus Suhling, David Richards, et al. Spontaneous emission in non-local materials. *Light: Science & Applications*, 6(6):e16273, 2017.

[227] Andres D Neira, Gregory A Wurtz, Pavel Ginzburg, and Anatoly V Zayats. Ultrafast all-optical modulation with hyperbolic metamaterial integrated in si photonic circuitry. *Optics express*, 22(9):10987–10994, 2014.

[228] Marc A Baldo, DF O'brien, Y You, A Shoustikov, et al. Highly efficient phosphorescent emission from organic electroluminescent devices. *Nature*, 395(6698):151, 1998.

[229] MAa Baldo, Sb Lamansky, PEc Burrows, MEb Thompson, and SRl Forrest. Very high-efficiency green organic light-emitting devices based on electrophosphorescence. *Applied Physics Letters*, 75(1):4–6, 1999.

[230] Ho Trung Dung, Ludwig Knöll, and Dirk-Gunnar Welsch. Intermolecular energy transfer in the presence of dispersing and absorbing media. *Physical Review A*, 65(4):043813, 2002.

[231] Martijn Wubs and Willem L Vos. Förster resonance energy transfer rate in any dielectric nanophotonic medium with weak dispersion. *New J. Phys*, 18:053037, 2016.

[232] Andreas Chrambach and Dt Rodbard. Polyacrylamide gel electrophoresis. *Science*, 172 (3982):440–451, 1971.

[233] Heike Summer, René Grämer, and Peter Dröge. Denaturing urea polyacrylamide gel electrophoresis (urea page). *JoVE (Journal of Visualized Experiments)*, (32):e1485–e1485, 2009.

[234] Alain Sillen and Yves Engelborghs. The correct use of "average" fluorescence parameters. *Photochemistry and photobiology*, 67(5):475–486, 1998.

[235] Asif Iqbal, Sinan Arslan, Burak Okumus, Timothy J Wilson, Gerard Giraud, David G Norman, Taekjip Ha, and David MJ Lilley. Orientation dependence in fluorescent energy transfer between cy3 and cy5 terminally attached to double-stranded nucleic acids. *Proceedings of the National Academy of Sciences*, 105(32):11176–11181, 2008.

[236] Steven S Vogel, Tuan A Nguyen, B Wieb van der Meer, and Paul S Blank. The impact of heterogeneity and dark acceptor states on fret: implications for using fluorescent protein donors and acceptors. *PloS one*, 7(11):e49593, 2012.

[237] Juan De Torres, Mathieu Mivelle, Satish Babu Moparthi, Hervé Rigneault, Niek F Van Hulst, María F García-Parajó, Emmanuel Margeat, and Jérôme Wenger. Plasmonic nanoantennas enable forbidden förster dipole–dipole energy transfer and enhance the fret efficiency. *Nano letters*, 16(10):6222–6230, 2016.

[238] Evgenii E Narimanov and Alexander V Kildishev. Metamaterials: naturally hyperbolic. *Nature Photonics*, 9(4):214–216, 2015.

[239] Karolina Korzeb, Marcin Gajc, and Dorota Anna Pawlak. Compendium of natural hyperbolic materials. *Optics express*, 23(20):25406–25424, 2015.

[240] Moritz Esslinger, Ralf Vogelgesang, Nahid Talebi, Worawut Khunsin, Pascal Gehring, Stefano De Zuani, Bruno Gompf, and Klaus Kern. Tetradymites as natural hyperbolic materials for the near-infrared to visible. *Acs Photonics*, 1(12):1285–1289, 2014.

[241] Alexander V Kildishev, Alexandra Boltasseva, and Vladimir M Shalaev. Planar photonics with metasurfaces. *Science*, 339(6125):1232009, 2013.

[242] Alexander A High, Robert C Devlin, Alan Dibos, Mark Polking, Dominik S Wild, Janos Perczel, Nathalie P de Leon, Mikhail D Lukin, and Hongkun Park. Visible-frequency hyperbolic metasurface. *Nature*, 522(7555):192, 2015.

[243] JS Gomez-Diaz and Andrea Alù. Flatland optics with hyperbolic metasurfaces. *ACS Photonics*, 3(12):2211–2224, 2016.

[244] J Sebastian Gomez-Diaz, Mykhailo Tymchenko, and Andrea Alù. Hyperbolic plasmons and topological transitions over uniaxial metasurfaces. *Physical review letters*, 114(23):233901, 2015.